Air Force Office of Scientific Research grant #91-0269

NUMERICAL SIMULATION OF A REGIONAL ICING EVENT BY A MESOSCALE MODEL

by Bruce David Muller

William R. Cotton, P.I.

Colorado State University

DEPARTMENT OF ATMOSPHERIC SCIENCE

PAPER NO. 607

NUMERICAL SIMULATION OF A REGIONAL ICING EVENT BY A MESOSCALE MODEL

by

Bruce David Muller

Department of Atmospheric Science

Colorado State University

Fort Collins, CO 80523

Research Supported by

Air Force Office of Scientific Research

under Grant AFOSR-91-0269

May 22, 1996

Atmospheric Science Paper No. 607

ABSTRACT OF THESIS

NUMERICAL SIMULATION OF A REGIONAL ICING EVENT BY A MESOSCALE MODEL

A control run and a series of sensitivity studies were performed for this study on the developing extra-tropical cyclone in the central plans of the United States on 31 October 1994. During this storm, a commuter plane crashed near Roselawn, Indiana, killing all 68 passengers and aircrew on board. A suspected or contributing factor in the crash was the presence of a high amount of supercooled liquid water which could have resulted in creating an extremely hazardous icing event.

The RAMS model was initialized using standard synoptic scale atmospheric data at 1200 UTC 31 October 1994, with a total of three stationary grids centered on Illinois and Indiana, which was the primary area of interest. The resulting extra-tropical cyclone very closely resembled observations and a supercooled cloud water field was produced in all the simulations performed at the flight level of the aircraft.

The sensitivity studies entailed varying the number concentration of activated cloud condensation nuclei (CCN) from as low as 150/cm^3 to as high as 1000/cm^3. Additional sensitivity studies were performed in which the shape parameter of the gamma distribution function was switched to ν=3 (versus the default value of 1), as well as a no hail case. The resulting droplet size distributions were then examined to determine icing potential based on the mass of cloud water in each bin of the droplet size distributions. Droplet size distribution is a critical element in determining icing potential. Large (D > 30 μm) droplets, having a higher collection efficiency than small droplets can, in certain types of distributions (low number concentration N_t) comprise most (over 80%) of the total mass of cloud droplets, resulting in potentially severe icing. Larger values of N_t require the droplet sizes to be

smaller and thus appear to reduce the icing potential. Various methods of calculating the expected potential accumulation were used and resulted in possible accumulations of around 1 cm thickness of ice to over 20 cm, depending upon the simulation performed. This illustrated that high-resolution ($\Delta X = \Delta Y \simeq 5$ km) cloud models can provide useful guidance in forecasting aircraft icing conditions.

Bruce D. Muller
Department of Atmospheric Science
Colorado State University
Fort Collins, Colorado 80523
Summer 1996

ACKNOWLEDGEMENTS

There are many individuals I would like to thank that greatly supported my research and assisting in achieving successful results. First of all, I would like to thank my advisor, Dr. William Cotton, for having suggested this very interesting subject to me in the first place, shortly after my arrival at graduate school. I would also like to thank and acknowledge my committee members, Dr. Thomas McKee and Dr. Paul Mielke for having served on my committee as well.

I am extremely grateful for having been selected by the AFIT program to attend graduate school. Obviously without this assignment and sponsorship by the AFIT program and the USAF, I would not have been able to attend graduate school at this time or so early in my career.

I would also like to send a special thanks to Dr. Marcia Politovich of the Research Applications Program, National Center for Atmospheric Research (RAP/NCAR), who provided many useful comments and much appreciated guidance in the writing of this thesis, as well as educating me and answering questions about the general subject of aircraft icing.

Lastly, I would also like to thank those individuals in the Cotton research project here at CSU for a tremendous amount of assistance in using the RAMS model. Most notably I would like to thank my current and past office partners Brian Gaudet and Sharon Nebuda for teaching me the basics of RAMS, Louie Grasso for supplying me with the model code that I used for these simulations, Jerry Harrington for helping me develop the new variables used in the VAN package and in general educating me about droplet size distributions, Bob Walko for always having a suggestion to try for the next simulation when the model wasn't cooperating, and the many other members of this group whom I've asked for help from time to time.

TABLE OF CONTENTS

LIST OF FIGURES

LIST OF TABLES

Chapter 1

INTRODUCTION

Aircraft icing was responsible for or a contributing factor in 803 aviation accidents in the United States between 1975 and 1988 (Cole and Sand, 1991). Icing has been a problem throughout the history of aviation, but it has become more significant with the advancement of aircraft instrumentation that has allowed for prolonged flights into areas of cloudiness and poor visibility. Commercial aviation has spread to all parts of the country and the world, and has demanded that technology allow for travel into less-than-ideal weather conditions. Therefore, it is no surprise then that icing has become more of a problem as planes now routinely travel through weather conditions thought to be impossible or inadvisable just a few decades ago. High performance wings (high speed) are more vulnerable to icing conditions than regular wings and an increase in the number of commuter class aircraft in recent years has increased the number of lower level flights than previously, both of which have contributed to an increasing icing hazard over the years. The hazard of aircraft icing is not so much a problem of the additional weight of the ice accumulated, since the amount of ice is seldom more than a few percent of the aircraft weight itself and usually well within an airplanes cargo carrying weight capacity. The problem with icing is that the accumulated ice on the fuselage disrupts the airflow both increasing the drag and reducing the lift of the plane, which can be extremely detrimental to flight if not avoided.

Many different forecast techniques have been implemented over the years in an attempt to predict the icing potential, both of intensity and type, of icing. These methods are inherently flawed as they are too simplistic and tend to overforecast actual occurrences of icing, especially those involving the most severe types of icing. The microphysical process of forming the supercooled liquid water necessary for icing to occur are too complicated to

be forecast by merely looking for favored areas on the weather map based on past incidents and climatology. An attempt to model these situations which create known occurrences of icing must be made in order to further the understanding of this aviation hazard.

The purpose of this thesis is to examine if a forecast, using the Regional Atmospheric Modeling System developed at Colorado State University (RAMS), could aid in identifying potentially hazardous icing regions. A simulation is performed of the 31 October 1994 mid-latitude cyclone over Illinois and Indiana in which icing was suspected to be a major contributor to the crash of an American Eagle ATR-72 commuter flight near Roselawn, Indiana, killing all 68 people on board. The various types and intensities of icing will be discussed (Chapter 2) as well as the meteorological conditions that are necessary for each. Several of the current methods for the prediction of icing will also be discussed, along with the problems and limitations of each (Chapter 3). The RAMS model, the model used for this simulation will also be described as well as the set up of various parameters and grid locations used in this simulation (Chapter 4). The synoptic setting of the storm will be discussed, in which the previously mentioned mid-latitude cyclone developed and moved into the Illinois-Indiana area developing large areas of heavy rainfall, strong winds, and hazardous icing conditions aloft (Chapter 5). The simulation of this storm will be compared to actual observations as best as possible in order to evaluate the model's ability to forecast the mesoscale conditions necessary for the production of supercooled liquid water and aircraft icing (Chapter 6). Modeling sensitivity studies will be discussed, which will compare the effects of changing the cloud droplet concentration and its affect on cloud water and ice processes thereby affecting the icing potential (Chapter 7). Finally, the conclusions reached from this research will be discussed along with suggestions for future research into the area of forecasting aircraft icing (Chapter 8).

Chapter 2

ICING

2.1 Conditions Associated with Icing

The most fundamental condition necessary for the formation of aircraft icing is the presence of supercooled liquid water in the atmosphere. The FAA (1975) published a guide called *Aviation Weather for Pilots and Flight Operations Personnel* in which it is stated that two conditions must be present for icing to occur. First, the aircraft must be flying through visible water such as rain or cloud droplets. Second, the temperature where the droplets impact the fuselage must be below freezing to allow for freezing onto the aircraft. This is an oversimplification of the problem surrounding icing and says very little about the weather conditions necessary to produce icing except for the obvious parameters of water and temperature. This offers very little guidance for forecasters looking at current weather analysis charts or forecast model output about where to look to predict icing potential. How one arrives at diagnosing or forecasting the presence of supercooled liquid water in a particular environment is a challenge of aviation weather forecasters, however there are certain synoptic or mesoscale environments that favor icing.

Supercooled liquid water is produced through a variety of mechanisms, such as lifting and moisture advection into colder environments. Condensation of vapor into cloud droplets must occur and coalescence of these cloud droplets into larger droplets, such as drizzle droplets can also occur. As will be explained later, larger droplets present a much greater hazard than smaller droplets for a given cloud water mixing ratio. Pobanz *et al.*, (1994) and Politovich (1989) described these environments which favor the formation of supercooled drizzle droplets (SCDD) to include a combination of strong vertical wind shear and a stable thermodynamic profile near the cloud top. This combination, if sufficiently strong, can

produce a Richardson number of less than one which can induce Kelvin-Helmholtz (KH) waves and turbulent mixing. The formula for the bulk Richardson number is given by Eq (2.1),

$$\mathrm{Ri} = \frac{\frac{g}{\theta}\frac{\Delta\theta}{\Delta z}}{\left(\frac{\Delta\vec{V}}{\Delta z}\right)^2} \tag{2.1}$$

where g is the acceleration due to gravity, θ is the potential temperature, $\Delta\theta$ and $\Delta\vec{V}$ are the changes in the potential temperature and wind vector across the shear layer Δz. So it can be seen that in order for KH waves and turbulence to occur, one would want to have low values of potential temperature gradient (low stability) or strong values of shear to produce the desired value of Richardson number less than unity. Pobanz *et al.,* (1994) stated that all three of the following must exist for a dynamically unstable shear layer to exist; a distinct change in the wind vector, a vertical shear value of at least 0.02 s^{-1}, and as mentioned above, a value of Ri less than 1.0. Having this dynamically unstable layer coincident with a cloud where significant amounts of supercooled liquid water are present then can act to force the cloud droplet distribution towards larger sizes.

One hypothesis is that turbulent mixing, as opposed to stagnant or more laminar flow, helps to initiate or accelerate the coalescence process by also forcing turbulent motions of the cloud droplets. Stagnant or laminar flow would have fewer collisions between cloud droplets than turbulent flow. When considering small scale turbulent motions (on the order of fractions of centimeters or millimeters), de Almeida (1979) calculated the droplet size distribution broadening and found that the smallest droplets (radius < 10 μm) had collection efficiencies dramatically increase even in the slightest amounts of turbulence compared to purely laminar flow or still air. His calculation resulted in a substantial broadening of the distribution resulting in the creation of precipitation-sized droplets in the time scales observed in nature. The effect of turbulence on droplet size distribution broadening were less noticeable as droplet size increased, and at larger droplets radius > 30 μm), turbulent motions added little if any to the amount of broadening compared to pure gravitational settling and collection (in a non-turbulent environment).

While these results were certainly encouraging, they were largely rejected by the atmospheric science community mainly based on errors he made in his use of the turbulent energy spectrum (Lomaya *et al.*, 1990). Having accounted for and correcting these errors, new calculations of turbulent collection efficiencies were made for small scale turbulence by Lomaya *et al.*, (1990), Cooper (1989), and Reuter *et al.*, (1989). These resulted in substantially lower collection rates that while still showing some enhanced broadening, could not explain the observed size distribution broadening and warm rain processes.

The other theory to be considered in this case, is that of inhomogeneous mixing which would be forced by the initiation of K-H waves described above (a much larger scale turbulent process). Inhomogeneous mixing into a stratiform cloud, for example, is a process in which dry air is entrained downward into the cloud (Cotton and Anthes, 1989). These eddies can occupy much of the depth of the shear layer in question along the top of the cloud ($\sim$ 100-200 m). The inhomogeneous mixing that takes place forces the smallest droplets to completely evaporate (mixing in of drier air, as well as subsidence warming) and larger droplets to only partially evaporate, thus leaving a lower number concentration of cloud droplets. When condensation is allowed to resume on the upward cycle of the K-H wave, there are fewer remaining cloud droplets to compete for the available water vapor, thus larger droplets form by vapor depotision. Creation of large droplets can then allow for the initiation or enhancement of coalescence, furthering the broadening process. This cycle can continue indefinitely for stratiform clouds if they occupy a large horizontal area, or are otherwise long-lived. The evidence presented by Pobanz *et al.* strongly suggests that the inhomogeneous mixing process is responsible for forming large droplets in the tops of stratiform cloud, however the evidence is also circumstantial and insufficient to resolve whether small scale turbulence or inhomogeneous mixing (if either) are responsible.

A final significant necessary step to create a larger mean droplet size would be to have a dry layer capping the gradually ascending stratiform cloud region such that the cloud top temperatures are relatively warm, in this case greater than -15°C. This dry layer is typically around or above the 700mb level, not uncommon for mid-latitude cyclones in the central plains of the United States, and is important to prevent glaciation of the cloud

and removal of supercooled liquid water via ice processes. With cloud top temperatures significantly colder than -15°C, ice processes which can initiate precipitation become much more efficient in removing supercooled liquid water via seeder-feeder process (Cotton and Anthes, 1989), thereby reducing the icing potential of clouds.

Having all of the above conditions in place for a particular cloud environment would therefore create the maximum potential threat for icing and probably moderate to severe levels of icing at that. The most common locations relative to a typical mid-latitude cyclone (Carlson, 1980, and Reed *et al.*, 1994) for these most favorable icing locations to occur are poleward of the warm front of a storm, where you already have gradual lifting of the warm sector (combined with the most moisture) and where it is also common to have the above-mentioned dry layer above low to mid-level stratiform clouds (Politovich, personal communication). As will be discussed in Chapter 5, this was the location of the flight path of the doomed aircraft relative to the storm in question and the model output and analysis of these parameters will be covered there.

2.2 Types of Icing

There are several categories of icing that can occur on an airframe, each of which have their own special meteorological conditions which favor their formation. Each type of icing can also be further characterized by a level of intensity or rate of accumulation (trace, light, moderate or severe). The rates of icing are somewhat subjective as it is up to the pilot to determine the intensity of the icing (see Section 2.3, Intensity of Icing). The aircraft involved may have deicing equipment that would prevent or reduce the amount of ice that accumulates on the airframe. Thus, light icing to a large aircraft such as a passenger jet with deicing equipment may be moderate or severe to a smaller aircraft which does not have deicing equipment. The type of airframe involved also can influence the formation of icing, and some airframes are more susceptible to degradation of flight than others given the same meteorological conditions. The types of icing can be broken down into three broad categories, rime icing, clear icing and mixed icing (Air Weather Service, 1980).

2.2.1 Rime Icing

Rime icing forms as a result of supercooled liquid water (SLW) droplets immediately freezing to the leading edge of the airframe, i.e. the wings or the fuselage of the aircraft. Since it freezes instantaneously, the droplets form a rough surface that is also opaque or milky in appearance. This appearance is a result of trapping small air pockets in with the ice. The instantaneous freezing prevents the smearing of the ice, which would remove those air pockets (see Section 2.2.2, Clear Icing). This type of icing is the most common and usually not dangerous, except in large amounts when the icing is encountered for long periods of time. This is the easiest type of icing to protect against, as the deicing equipment is typically located along the leading edges of the wings, propellers, and the fuselage in aircraft equipped to handle icing. This type of icing occurs when the temperature of the air is sufficiently below freezing to allow for instantaneous freezing (colder than about -4°C) and the droplet size distribution for rime icing usually is such that the mass mean diameter[1] is relatively small, also supportive of instantaneous freezing into ice of the SLW. Smaller drops also have greater dynamic stability and are less likely to deform or smear upon impact with the fuselage. Rime icing is not solely dependent upon droplet size distribution, however, it also depends upon the total mass that freezes and releases its latent heat. Rime icing can also be created with large droplets if it is relatively cold and/or there are relatively few of them (Politovich, personal communication).

2.2.2 Clear Icing

Clear icing is different from rime icing in that the rate of accretion of SLW is so high or the temperature of the air warm enough that instantaneous freezing is not possible, and the water flows along the surface of the wings or fuselage before freezing (Sand *et al.*, 1984). This is basically a problem of local heat budgets. If the latent heat released from a water droplet undergoing freezing on the fuselage cannot be dissipated quickly enough by the ice

---

[1] Mass mean diameter is defined here as it is in most icing literature to be the diameter in which half the mass of liquid water is contained in droplets smaller than this size, and half the mass is contained in droplets greater than this size (Sand, *et al.*, 1984).

already present, the skin of the fuselage or the airstream around the wing, heat builds up in the water which prevents instantaneous freezing. As the name implies, it is clear in appearance as no air bubbles are trapped upon freezing, unlike rime icing. The clearness of ice is also related to the amount of air dissolved in the water, as solubility of air increases with decreasing temperature. Thus rime ice freezing at cold temperatures can be milky white while clear ice freezes closer to 0°C (Mason, 1971).

Some of the meteorolgical conditions associated with this type of icing include large cloud droplet or drizzle drop sizes between 30μm and 250μm (Pobanz *et al.,* 1994), higher supercooled liquid water content (Schultz and Politovich, 1992) and warmer air temperatures than would create rime icing. The American Meteorological Society (AMS) Glossary of Meteorology (1980) defines droplets as either cloud, drizzle, or rain based on their diameter. Cloud droplets have sizes up to 200μm, drizzle droplets are between 200μm to 500μm, and rain droplets are larger than 500μm. There is some ambiguity between definitions of droplet sizes, some icing researchers consider supercooled drizzle droplet sizes to range from as low as 40μm up to 400μm (Politovich *et al.* 1995).

At any rate, large drops contain more heat to be dissipated per unit surface area than smaller drops, so it follows that larger (drizzle or rain) droplets impacting onto the leading edge of the wing or fuselage could take longer to dissipate their latent of fusion by conduction and diffusion than small drops. This time lag allows the water to flow before becoming completely frozen. Larger droplets are also more likely to deform their shape upon impact with the fuselage, a characteristic which will therefore cause the smearing and air pocket removal that doesn't happen to smaller, more dynamically stable water drops.

It also follows that higher supercooled liquid water contents would tend to favor clear icing over rime as a faster accumulation of liquid water also results in a greater release of latent heat (all other things being equal) which of course would tend to increase the time it takes for the impacting water to freeze. There are no good threshold values available (i.e. mixing ratios) of cloud water that would favor clear icing over rime icing, as the type of icing as mentioned in this section more strongly depends on temperature and droplet size

distribution. Cloud water amounts do more to determine the icing intensity (see Section 2.3, Intensity of Icing) than the type.

Another important condition for clear ice is that when the air temperatures are close enough to freezing, compression of the air along the leading edge of the fuselage creates a local warming of the air that further reduces the removal or latent heat from the accreted water to allow for instantaneous freezing. The magnitude of this warming is on the order of 2-3°C for a airplane flying at an airspeed of about 200 knots. An airplane flying faster than this would have a greater amount of dynamic warming, and a slower plane would have less. In this sense then, clear icing does not have a well-defined threshold temperature as it depends on the airspeed and the aerodynamics of the airframe. To further complicate the situation, aircraft such as helicopters have experienced different types of icing along the length of the blade. The relative airspeed of the tip of the blade is considerably faster than near the root, so rime ice can form near the root transitioning to clear icing near the tip (Politovich, personal communication).

Freezing rain events are particularly hazardous and can also result in clear icing (or the term glaze icing, which is also used to describe freezing rain events) as the large raindrops (relative to cloud and drizzle droplets) having fallen through layers of above freezing and subsequently below freezing air can freeze upon impact with the airfoil, assuming of course that the temperature of the airfoil skin is also below freezing. Airplanes can encounter clear icing without even flying. Clear ice can accumulate over all exposed surfaces by just being parked on the ground or taxiing while freezing rain occurs. Freezing rain also generally occurs where aircraft are most vulnerable, in the lower altitudes generally associated with takeoff, landing and reduced flight speeds. Freezing rain becomes less common more than a few thousand feet above ground level.

Clear icing then, is especially hazardous, since the ice accumulates along the top and bottom surfaces of the airfoil, which can seriously disrupt airflow around the wings. The accumulation of ice in these areas reduces the amount of lift generated by the wings. It is also hazardous as a result of the design of the deicing equipment. Most deicing equipment is

located along the leading edges of the wing and works well to remove rime icing accumulated there but often cannot remove clear ice further back along the surfaces.

2.2.3 Mixed Icing

Mixed icing, as the name implies, is merely a combination of the two types of icing described above, rime icing and clear icing (Air Weather Service, 1980). When meteorological conditions are encountered such that the air temperature, droplet size distribution and/or droplet concentration are truly marginal for either case, both types of icing may be encountered. The droplet size distribution may be such that larger droplets may result in clear icing and smaller droplets form rime icing at the same time assuming that there is sufficient liquid water content in either the large or small droplet sizes and the smaller droplets have a collection efficiency greater than zero. It is also possible to alternate back and forth between both types of icing, thus creating mixed icing, in a fairly small distance and short time frame. Stratiform clouds with embedded cumulus cells for example may very well be the type of environment that would provide enough variety in the cloud water and temperature fields over small spatial and time scales to create mixed icing. This type of icing is generally not as hazardous as clear icing, as not all water flows back along the wing, but it is much more hazardous than pure rime icing.

2.3 Intensity of Icing

As mentioned before, icing intensity is a very subjective call on the part of the pilots. They are not without guidance, however, as Table 2.1 shows. The table (Newton, 1978) outlines this guidance. The rates of accumulation column on Table 2.1 refer to calculations made by Lewis (1947) and are rates of collection of ice at 200 mph on a circular cylinder 3 inches in diameter. The Ice Accumulation column on Table 2.1 refers to guidance as approved by the Subcommittee for Aviation Meteorological Services in 1968. The units of g/cm^2-h can be used to infer a thickness of ice accumulated by the cylinder per hour (or similarly, the leading edge of a wing), by dividing this number by the density of ice.

Thus, Eq. (2.2) relates a rate of actual accumulation of ice in thickness (cm) per unit cross-sectional area as opposed to the mass of ice (g).

$$\text{Ice Thickness Rate (cm/hour)} = \frac{\text{Rate of Accumulation (Table 2.1)}}{\rho_{ice}}. \tag{2.2}$$

Table 2.1: **Airframe Icing Reporting Table (Newton, 1978)**

Intensity	Rate of Accumulation	Ice Accumulation
Trace	0.0–1.0 g/cm^2-h	Ice becomes perceptible. The rate of accumulation is slightly greater than the rate of sublimation. It is not hazardous even though deicing equipment is not utilized unless encountered for an extended period of time over 1 hour.
Light	1.0–6.0 g/cm^2-h	The rate of accumulation may create a problem if flight is prolonged in this environment for over 1 hour. Occasional use of deicing equipment removes/prevents accumulation. It does not present a problem if deicing equipment is used.
Moderate	6.0–12.0 g/cm^2-h	The rate of accumulation is such that even short encounters become potentially hazardous and continuous use of deicing equipment or diversion is necessary.
Severe	12.0–more g/cm^2-h	The rate of accumulation is such that deicing equipment fails to reduce or control the hazard. Immediate diversion is necessary.

The density of various types of ice vary considerably. Rime ice, with air bubbles trapped would be less than $\rho_{ice} \cong 0.8$ g/cm^3 and could be as low as 0.1 g/cm^3. Clear ice would be greater than ~ 0.8 g/cm^3 and in some cases be over 0.9 g/cm^3 (Macklin, 1962) with absolutely no air bubbles trapped in the ice. The exact values of density then depend upon the amount of air bubbles trapped inside the ice. It is no surprise then that the density of mixed icing falls over a large range between the extremes for both rime and clear icing.

Chapter 3

CURRENT FORECAST TECHNIQUES

Various methods for forecasting icing have been implemented over the years in an attempt to evaluate the potential to predict icing type and severity based on either model output or current analysis of fields such as relative humidity, temperature, and vertical motion (Schultz and Politovich, 1992). In this chapter, the National Weather Service (NWS) method, the Air Force Method, as well as experimental mesoscale modeling methods for predicting icing will be discussed, along with problems inherent to these methods.

3.1 National Weather Service Method

A division within the NWS at Kansas City called the Aviation Weather Center (AWC) provides icing forecasts within the continental United States. Their forecasts are intended for flight planning purposes only. They issue forecasts valid for 6 hr that are updated every 8 hr. Updates to these forecasts are transmitted to weather service offices and military base weather stations as AIRMETs (Airmen's Meteorological Information). AIRMETs are issued systematically based on satellite images, surface weather observations. Icing SIGMETs (Significant Meteorological Information) are issued as a reaction to pilot reports (PIREPS) of severe weather events encountered in flight.

For many years, AWC used almost exclusively synoptic-scale model output such as the Nested-Grid Model (NGM) and the Limited Fine-Mesh Model (LFM), to determine areas likely to form icing (Politovich and Olson, 1991). Through observational studies, icing conditions were most commonly found in clouds with temperatures between 0°C and -20°C, as SLW is rarely found in temperatures below -20°C or at least in such small amounts to be considered negligible. A wide range of 1000-500mb thicknesses is also looked at, as appropriate atmospheric temperatures for icing can be found between approximately 5220

and 5580 meters of thickness. Additionally, low level temperatures such as the 850mb temperature can be used to help determine icing, with a temperature range of about -12°C to +4°C allowing for icing somewhere in the lower to middle troposphere (Schultz and Politovich, 1992).

The amount of water available is certainly critical, and the only output available from the NGM is the 1000-500mb relative humidity. It has been shown that using a relative humidity (RH) greater than about 55% can support widespread areas of cloudiness within that layer, although not providing specific information about particular layers. Forecasters may combine this information with estimates of the freezing level to forecast icing potential above a certain altitude.

Finally, the AWC method used NGM-derived 700mb vertical velocity predictions. In general, upward vertical motion is required for condensation of water vapor into cloud water droplets, so regions of upward vertical motion predicted by the NGM are also looked at. Droplets would be evaporating and tending towards a smaller mean diameter in slight subsidence which then would favor smaller collection efficiencies and reduced icing. Strong upward vertical motions, such as in thunderstorm updrafts, are rapidly producing and growing cloud water droplets. However, all of the vapor does not condense, resulting in increased supersaturation in the clouds. So a foreign body, such as an airplane flying through an updraft which is rapidly trying to condense its water vapor into SLW, is providing additional surface area upon which to condense and freeze the vapor and at the same time collect the SLW forming ice.

The above conditions can be said to be necessary (but not sufficient) conditions, as icing cannot occur without condensed SLW, temperatures below freezing at flight level, and upward vertical motion that would favor additional condensation on droplets. This forecast method is oversimplified since it does not take into account the more complex physics involved with droplet sizes and their displacement from streamlines around objects such as an airplane wing (see Section 3.4). Nor does it take into account mesoscale or cloud-scale motions responsible for SLW production and drizzle formation. Thus, it could be said that this method provides a depiction of areas where there is a potential for icing.

Very recently, the AWC transitioned away from the above method toward automated algorithm guidance develped by the Research Applications Program (RAP) at NCAR. This method is one that now uses the Rapid Update Cycle (RUC) (Benjamin, *et al.*, 1994) and the Eta model output. This method is described in more detail in Section 3.3.

3.2 Air Force Method

The Air Force method is slightly more sophisticated since it takes into account, or rather assumes information about, the mean drop diameter. Forecasters specify a mean diameter of 14 μm in stratiform clouds and 17 μm in cumuliform clouds (Newton, 1978). These values were chosen based on the recommendation of Lewis (1947) during National Advisory Committee for Aeronautics (NACA) flight investigations begun in 1944. Next, using these droplet diameters, liquid water content corresponding to the onset of light, moderate or severe icing can be looked up by using the Lewis envelopes. These envelopes were an attempt to forecast light, moderate, or severe icing based only on knowledge or liquid water content and mean diameter. To summarize these envelopes, icing intensity increased both with increasing liquid water content and increasing mean diameter as expected. The liquid water content is derived by a cloud model by Best (1952). This model assumes adiabatic parcel ascent of clouds entraining in an environment where the entrained air has a relative humidity of 70%. The mass of the air in the entraining cloud is doubled for every 400mb of ascent. This model calculates an amount of liquid water content, the full value of which is used for cumuliform clouds and one-half of which is used for stratiform clouds. The reduction of liquid water for stratiform clouds was adopted by Best in accordance with observations made during NACA flight investigations (Newton, 1978).

A sounding is then evaluated using a Skew T-Log P or other thermodynamic diagram in which the stability of the airmass is evaluated, to determine the likelihood of either cumuliform or stratiform clouds. The corresponding liquid water value from the Best model is then used, and then using the Lewis envelopes, an intensity of icing is then determined. Also, the type of icing is also determined, as the Air Force method instructs forecasters to forecast rime icing for stratiform clouds and clear icing for cumuliform clouds. As will be seen in Section 3.4, the assumption of a particular mean droplet diameter size is crucial to this method and could invalidate this method if the wrong size is assumed.

3.3 Experimental Icing Algorithms

Although the above two methods have been used for years to attempt to forecast icing, the use of mesoscale models has only recently begun experimentally to attempt to further refine icing forecasts. The benefits of using a mesoscale model (like the MM5 or RAMS, as was used for this case study), are the adaptability of the model grids to a specific location of interest, the full or parameterized microphysics schemes which include accounting for all types of cloud water and ice species, and extremely fine resolution which can be used to resolve cloud-scale motions and convection if necessary. Politovich (personal communication) found that improving surface characteristics such as topography along with finer model resolution was one of the larger factors in making better forecasts. Theoretically, from knowledge of cloud water mixing ratios, and assuming a concentration of cloud droplets, one could let the model calculate the mean droplet size by conservation of water. Or, the model could find the droplet concentration by knowing a mean diameter or droplets or better yet, knowing the cloud-condensation nuclei (CCN) concentration and spectra. The downside of this is that increased resolution and complex microphysics can significantly increase the computational expense of model runs and at present cannot be run in real time for an area as large as the United States with as fine of a resolution as would be desired; about 5 kilometers or finer. The use of mesoscale models at present can therefore be used for after the fact case studies, research, and analysis where computer processing time is not a significant concern. They can also be used to identify icing threat areas and spawn finer resolution nested grids to that area and still run in real time if the area to be finely resolved is small enough.

The Research Applications Program (RAP) at NCAR is continually developing an icing scheme, originally attempted by Schultz and Politovich (1992), in which icing, if forecast, falls into either of four categories; General, Unstable, Freezing Rain, and Stratiform (Thompson *et al.*, 1996). The algorithm uses thresholds of atmospheric parameters such as temperatures, relative humidities, stability of airmasses (to determine possibility of convection), keeping track of above- and below-freezing airmasses aloft (to determine freezing rain potential), and cloud top temperatures, all from model output. The four categories of the

algorithm were an attempt to provide forecasters with the several distinguishable processes to form icing. Knowledge of weather systems and where things are occuring relative to what the model says should aid forecasters in fine-tuning the model results.

The threshold values correspond to the types of parameters usually associated with each type of event. The general portion of this algorithm uses values of temperature between -16° and 0^0C as well as relative humidity greater than 63%. The unstable portion is similar to this but it evaluates the conditional instability in order to determine the likelihood of convective clouds. The stratiform portion uses the parameters discussed in Chapter 2, the warm cloud top tempatures, the evaluation of the dynamic stability of cloud layers using the Richardson number, combined with the presence of cloudiness. Lastly, the freezing rain portion, as suspected, keeps track of warm and cold layers aloft that contribute to freezing rain events.

An additional scheme by AWC is similar to the RAP scheme, but uses only two categories to predict the probability of icing (the first having a smaller probability of icing than the second) and the category is reduced by one if a downslope flow of greater than 5 cm/s exists within 500 meters of the surface. The only difference between this method and the Schultz-Politovich method described at the beginning of this section is the addition of the vertical velocity constraint. Both of the above mentioned schemes have been evaluated statistically over previous methods of forecasting icing and have shown significant improvements in forecasting skill when these additional parameters are considered.

One final technique to attempt to forecast icing, which is still in its infancy and relatively untested is the use of neural net technology to attempt to forecast icing (Coffey, 1996). This method is unlike any other method in existance, but instead uses computer algorithms to recognize weather patterns as they occur. The computer would have access to a database of PIREPS and the corresponding atmospheric conditions associated with those PIREPS (along with the geographic location of those PIREPS). When similar enough patterns repeat themselves at some future time, the computer then forecasts the same icing type and intensity in the locations which previously had icing PIREPS. If the forecasted icing event occurs or is otherwise verified, the programmer 'trains' the computer and by increasing the probability of it forecasting the same event in the future in similar conditions.

If the forecast were to be wrong, the programmer can 'teach' the computer about what actually happened so it is less likely to make the same mistake in the future, i.e. simple rote learning.

This method obviously has its advantages as well as its disadvantages. First of all, forecasters seem to like this method as it mimics what an experienced forecaster would do in recognizing weather patterns, without running the risk of forgetting any previous occurrances. This method is obviously limited by the database, as the atmosphere can never completely reproduce itself identically. However, this method certainly has the ability to improve itself in the future as it gains experience and the database grows. Therefore, this method is largely based on statistical methods and simple rote learning. The neural net method doesn't actually try to model the development of the storm and forecast things like temperature and droplet size distribution. It essentially can or will be used as a nowcasting tool providing information which can be made readily available to pilots, even while in flight based on current observations. Another limitation is that this method is highly dependent upon good observations of all types to aid in its pattern recognition, not just upper air soundings and surface observations. Including more information such as Doppler radar information to locate and track convection, precipitation, etc. along with a reasonably dense profiler network would also be necessary to aid the computer in its pattern recognition.

3.4 Problems

The problem of aircraft icing is a much more difficult one than can be simply evaluated from a few plots. Recent studies have shown that it can be just as important to evaluate the droplet size distribution as well as the number concentration of the supercooled liquid water drops in order to more accurately predict the severity of icing. Since aircraft icing is essentially an accretion problem, the formation of icing on airfoils is much like the growth of hailstones. Smaller sized SLW droplets are able to follow the streamlines around the wing of the aircraft, never impacting the wing leading to a collection efficiency of nearly zero. As with the case of hail however, the collection efficiency can increase dramatically toward unity as the droplet sizes increase; the larger drops have too much inertia to follow the streamlines around the wing.

Fortunately, assuming a typical size distribution of cloud water droplets, there are relatively few of these largest droplets as most of the cloud water is contained in the small drops which may never impact the fuselage. The problem arises as to where the mean diameter falls in the size distribution and what the collection efficiency of this droplet size would be. As a final complication, the aerodynamics of the wing itself can alter the collection efficiencies so that a particular size distribution can create more severe icing among different types of aircraft or even on different parts of the wing and locations on the airframe. Aircraft that have very sleek aerodynamics (such as supersonic aircraft) don't have blunt leading edges and large cross-sectional areas, such as transport or large passenger aircraft. The sleek profile of the performance aircraft fuselage presents a smaller cross-sectional area than the blunt wing, resulting in a smaller rate of collection than for the same size droplets impinging upon a wing with a larger cross-sectional area. Angle of attack also influences the cross-sectional area presented, hence affecting the collection of water. Aircraft performing any type of climbing or turning manuevers increase their angle of attack (angle between actual line of flight and the orientation of the aircraft) compared to steady straight line flight. Thus, higher angles of attack usually produce more turbulent flow around the aircraft that would tend to increase collection efficiencies of cloud water. The more blunt leading edge wings are built to generate more lift and fly at slower speeds leading to lower collection efficiencies. These effects somewhat offset each other as a sleeker wing generates less lift at the same airspeed than does a blunt wing, so the sleeker wing is more susceptible to loss of lift from accumulating ice than does the larger wing. The use of flaps which is common at lower levels during takeoff or landings, also similarly increases collection area and more dramatically affects the airflow than when they are retracted.

One final problem that is inherent to all methods, is the problem of verification. Since the only practical method of verification of icing forecasts is through the use of PIREPS, verification is very subjective, if it happens at all. PIREPS, obviously, are only reporting what the pilot encountered along their particular route and time of flight. PIREPS tend to become very numerous in close proximity to major airports for several reasons. First, there is a higher density of flight-miles in the immediate vicinity of airports and because reports of icing in particular are more numerous in the lower levels where icing is more

of a problem. In many areas of the United States, especially in the northern plains and western states there are large areas in which commercial aviation does not routinely fly. This leads to essentially an over reporting of icing around airports and under reporting in more remote areas. Pilots may also not choose to report icing for whatever reason, even though they are always encouraged to do so. It is especially crucial to receive icing reports (both positive and negative) in areas where any method previously described would have predicted icing, or rather, to report icing in an area where icing had not been forecast. The problem with verification will probably always be an issue unless a reliable method of uniform (not dependent upon the aviation community) remote sensing of supercooled liquid water and its droplet size distribution is ever fielded (Bernstein, personal communication).

Chapter 4

MODEL DESCRIPTION

For these simulations, the Regional Atmospheric Modeling System (RAMS) developed at Colorado State University, Version 3a, was used. This model has been undergoing nearly continuous development and combines features of several earlier codes dating back to the 1970's (Pielke, *et al.*, 1992). In 1986, RAMS was created by combining features in a non-hydrostatic cloud model (Tripoli and Cotton, 1982) with a hydrostatic mesoscale model (Mahrer and Pielke, 1977). The model currently possesses the capability to use interactive nested-grid code that allows the user to telescope the subordinate grids down to finer scales and focus in on a more limited region of interest, saving on computational cost by using finer resolutions only in the immediate areas of interest rather than across the entire domain.

4.1 Components of RAMS

There are three main components to RAMS, the isentropic analysis package (ISAN), the model itself, and a visualization and analysis package (VAN) which is used to graphically display the output. The first component, ISAN, performs the analysis of the data sets which are usually NMC mandatory level 2.5 degree global data sets, NMC rawinsonde and surface observation data sets. All significant and mandatory levels in the rawinsonde data can be used, along with special soundings or observations. Certain items, such as erroneous sounding data can be omitted from the analysis to prevent contamination of the data. Mesoscale Analysis and Prediction System (MAPS) data sets can also be used if desired, as this is a finer resolution (60 km) data set, but it is also limited in area to just slightly larger than the USA. This data set could not be used for any simulation that extended much beyond the borders of the continental United States. Additionally, the RUC model mentioned in the last chapter can be used to initialize the model. Once these data files

are read, a Barnes objective analysis scheme is then applied to the atmospheric variables which need to be written to a grid format. These variables include wind components, thermodynamic, and moisture variables. Gridded surface data sets are also made at this time, which take into account such things as topography, vegetation, and soil types, moisture, and temperature at 11 below-ground soil levels. The surface data are extremely important as it is well known that variations in surface characteristics have drastic effects on sensible and latent heat fluxes, evapo-transpiration, and slope flows, for example.

4.2 Features Selected for Simulation

The RAMS model is a highly adaptable numerical model, allowing for a variety of parameters to be adjusted as desired by the user, including numerical schemes, surface characteristics, radiation schemes, cumulus parameterization, diffusion coefficients, and microphysics complexity for example. The model uses a terrain-following sigma coordinate system. The variables predicted include the components of wind velocity, u, v, and w, Exner function π, mixing ratio of all water species, dry air density ρ, and ice-liquid potential temperature θ_{il} on an Arakawa-C grid (Arakawa and Lamb, 1981). All of the remaining variables are diagnosed from these prognostic variables.

To summarize the basic setup of the model as it was used for these simulations, the following features were selected. The model was run in a non-hydrostatic and compressible mode (Tripoli and Cotton, 1982). The radiation scheme was one developed by Mahrer and Pielke (1977) for both the incoming shortwave and outgoing longwave radiation with longitudinal variation of the shortwave radiation. The Mahrer and Pielke scheme does not consider cloud effects in radiation calculations, but has been shown to be somewhat more accurate and faster than the Chen and Cotton (1983) scheme also available to the user (Harrington, personal communication). The frequency of radiation tendency updates was set to 900 seconds. The soil model was one developed by Tremback and Kessler (1985) in which 11 grid points were specified from the surface down to 50 cm below ground. The vegetation model was one developed by Avissar and Pielke (1989). The soil type was homogeneously initialized to be sandy clay loam and the vegetation type was specified to be crop/mixed farming throughout the entire domain, as these are the dominant types

throughout the model domain, especially in the second and third grids (see Section 4.5). The soil moisture was also homogeneously initialized across the domain to be 20% of the total soil water capacity. This was a reasonable assumption since according to the Weekly Weather and Crop Bulletin (1994), much of the midwest had encountered a particularly dry fall following an already hot and dry summer as of 29 October 1994. The drought severity approached moderate to severe levels from central Kansas to Ohio, once again in the grid 2 and grid 3 domain.

A hybrid timestep scheme was used wherein velocity components and pressure are updated using leapfrog differencing and all other prognostic variables are advanced using forward differencing (Walko *et al.*, 1993). Both the forward and leapfrog differencing used second order advection. The Exner function which is used to update the momentum variables were predicted using a time-split scheme (Klemp and Wilhelmson, 1978). The computed diffusion is based on the Smagorinsky scheme (Smagorinsky, 1963) with stability modifications by Lilly (1962). The bulk microphysics used will be described in the next section.

4.3 Microphysics

The bulk microphysics package was used with full complexity activated. This microphysics scheme predicts the evolution and mixing ratios of the hydrometeor species, including total water, rain, pristine ice, snow, aggregates, graupel and hail ($r_t, r_r, r_p, r_s, r_a, r_g$, and r_h, respectively). In order to calculate cloud water, r_c, a couple more steps must be taken. The sum of mixing ratios of cloud water and vapor is determined to be the difference of total water mixing ratio and the other six hydrometeor species, according to Eq 4.1

$$r_{c+v} = r_t - (r_r + r_p + r_s + r_a + r_g + r_h) \tag{4.1}$$

Then, the cloud water mixing ratio r_c, is diagnosed as the amount by which the sum r_{c+v} exceeds the saturation mixing ratio with respect to liquid water, r_{sl}. If r_{c+v} does not exceed r_{sl}, then r_c is set to zero (Walko *et al.*, 1995). All the hydrometeors are predicted based on a single-moment scheme where the user specifies a parameter such as number concentration (see Section 4.4) and shape parameter, and the model diagnoses droplet size

for example. Other options available in this version of RAMS are: a) using a default value of number concentration specified in the code and then predicting mean diameter, b) specifying the y-intercept value of the number concentration (per unit diameter evaluated at zero diameter assuming a Marshall-Palmer size distribution) and letting the model diagnose mean diameter, c) specifying the mean diameter and letting the model diagnose the number concentration, or d) diagnosing a mean diameter from both a prognosed mixing ratio and prognosed number concentration (Walko *et al.*, 1993). The latter of these options is referred to as a two-moment scheme (Meyers, 1995) where a third variable is diagnosed from two other prognosed variables. It is being incorporated into later versions of RAMS but is still undergoing testing and refinement.

In these simulations, the single-moment scheme was used, where the number concentration of hydrometeors was specified by the user in the model code, except for pristine ice, in which the concentration is predicted. This particular version of microphysics was developed for use with RAMS Version 3b, but is compatible for use with RAMS Version 3a.

4.4 Departure from Standard Code

The code used was largely standard 3a code, applying the various fixes to known bugs as required. The one parameter that was adjusted by the user in order to perform sensitivity studies was the parameter in rmicr3a.f in which cloud droplet concentration, N_t, is specified. This parameter was adjusted as required in order to vary the cloud water concentration (or rather, the activated CCN concentration) from values as low as $150/\text{cm}^3$ to as high as $1000/\text{cm}^3$.

Along the same lines as the above change, another change was made to the VAN code in order to display the mass mean diameter of cloud water droplets. New code was added in rafld3a.f by specifying a new variable to plot (labelled 'MEANDI' for mass mean diameter) and adding a subroutine to do the calculations. This calculation assumes the droplet size distribution is a gamma distribution which depends on the shape parameter ν, set to the same value as used in the model run (Walko *et al.,* 1995). The calculation also takes into account the cloud droplet concentration specified (see above). The formulas used for this

are:

$$D_n = \left(\frac{r_c}{N_t}\frac{6\rho_a}{\pi\rho_l}\frac{1}{(\nu)(\nu+1)(\nu+2)}\right)^{(1/3)} \tag{4.2}$$

$$D_m \cong (2.67+\nu)D_n \tag{4.3}$$

where D_n is the characteristic size in meters, r_c is the mixing ratio of cloud water in kg/kg, N_t is the number concentration in #/m^3, ν is the shape parameter of the distribution function, ρ_a is the density of air in kg/m^3, ρ_l is the density of water, or 1000 kg/m^3, and D_m is the mass mean diameter. The motivation for doing this type of plot was to get an idea what the droplet spectrum looked like, since as explained in Chapter 2, droplet size (i.e. knowing the mass mean diameter) along with knowing the mixing ratio of supercooled cloud water were the critical ingredients in determining the type and intensity of aircraft icing. For a more complete discussion and derivation of the method used to compute D_m as well as other variables of interest, see Appendix A.

4.5 Grid Setup

One of the benefits of using a mesoscale model such as RAMS is the flexibility in locating the grids in the immediate region of interest, and using multiple grids and moving those grids, if necessary to track the weather systems of interest. RAMS can run an unlimited number of nested grids if desired, however for these simulations, only three stationary grids were used. See Figures 4.1 and 4.2 for the geographic location of the grids used. Figure 4.2 also shows the location of the crash site of the ATR-72 and Indianapolis within Grid #3. Both of these locations were marked as the aircraft had an almost direct flight from Indianapolis to the crash site near Roselawn Indiana.

The first (coarse) grid covers the entire continental United States as well as adjoining ocean areas, southern Canada and northern Mexico, and uses 68 east-west grid points and 42 north-south grid points with a grid spacing of 80 km. The second grid was 46 grid points on each side, having a grid spacing of 20 km. The third and finest resolution grid had 74 grid points on each side while having a grid spacing of 5 km. The second grid was placed in order to cover the path of the mid-latitude cyclone throughout the entire 12 hour simulation.

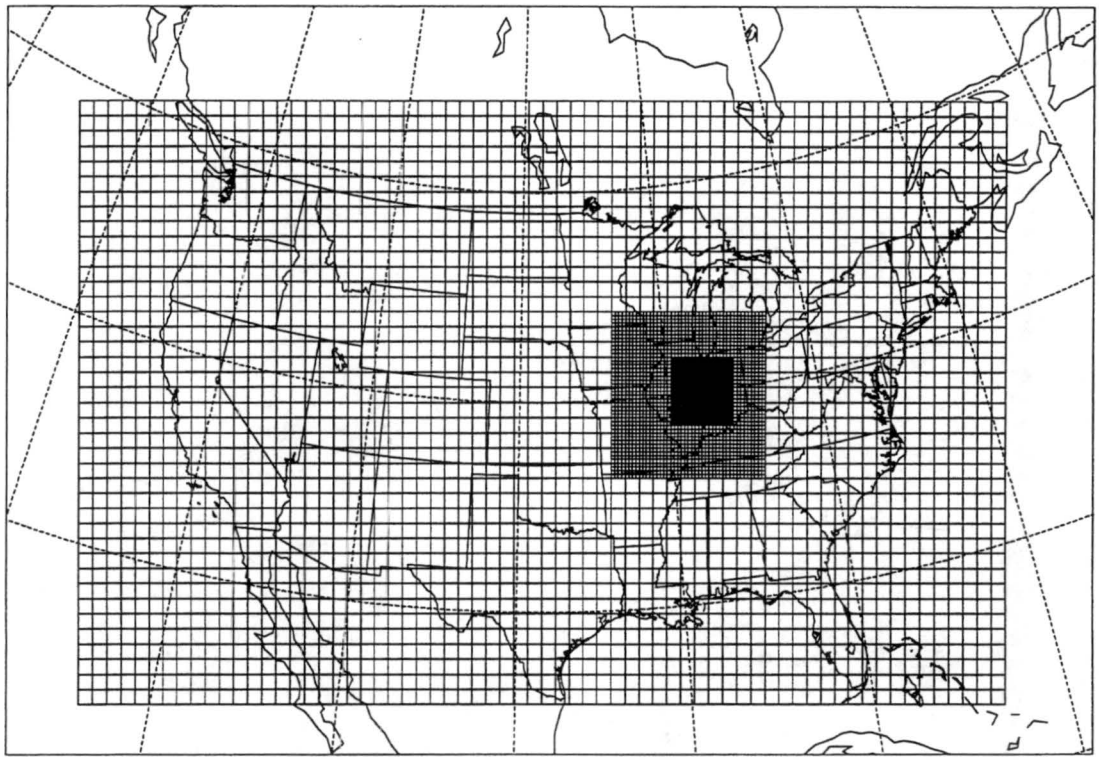

Figure 4.1: This figure displays the location and orientation of the three grids used in the RAMS simulation.

The third grid was placed in order to more finely resolve the immediate region of the route of flight over Indiana as well as the weather system approaching from the southwest.

Thirty vertical grid levels were used, starting with a minimum grid spacing 200 m expanding upward with a stretch ratio of 1.15 to a maximum vertical grid spacing of 750 m. Based on these numbers, all three grids reached an altitude of about 18 km or above 100 mb, well above the tropopause. All of these grids used a long time-step of 90 seconds, but the timestep ratio was set to 1/3, such that the second and third grids used a 30 second and 10 second time-step, respectively.

Figure 4.2: This figure is a close-up of grid three, also showing the locations of Indianapolis and the crash site.

Chapter 5

SYNOPTIC SETTING AND MODEL INITIALIZATION FOR 31 OCTOBER 1994

5.1 Synoptic Setting

During the daylight hours of 31 October 1994, a developing extratropical cyclone was analyzed by the National Weather Service to be over southwestern Missouri at 1200 UTC (Fig. 5.1) but moving rapidly to the northeast so that at 2100 UTC, it was located along the Illinois-Indiana border (Fig. 5.2).

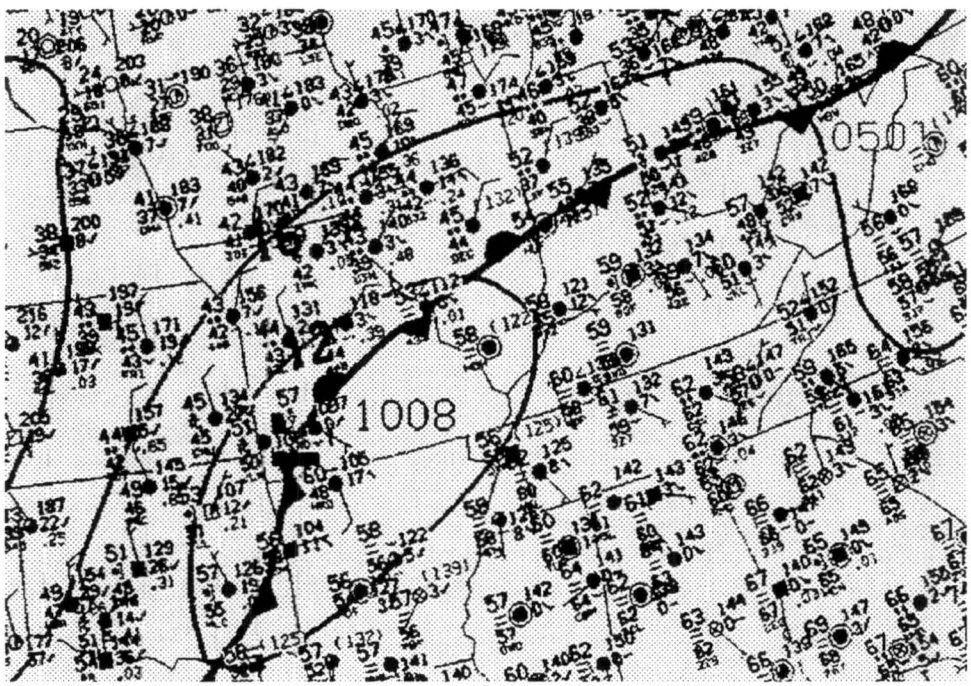

Figure 5.1: The NWS surface analysis for 1200 UTC 31 October 1994.

This center of low pressure was observed to have dropped in pressure from 1008 mb to about 1001 mb nine hours later. Along with this developing cyclone was a strong baroclinic environment, many of the surface stations were reporting temperatures in the high 30's and

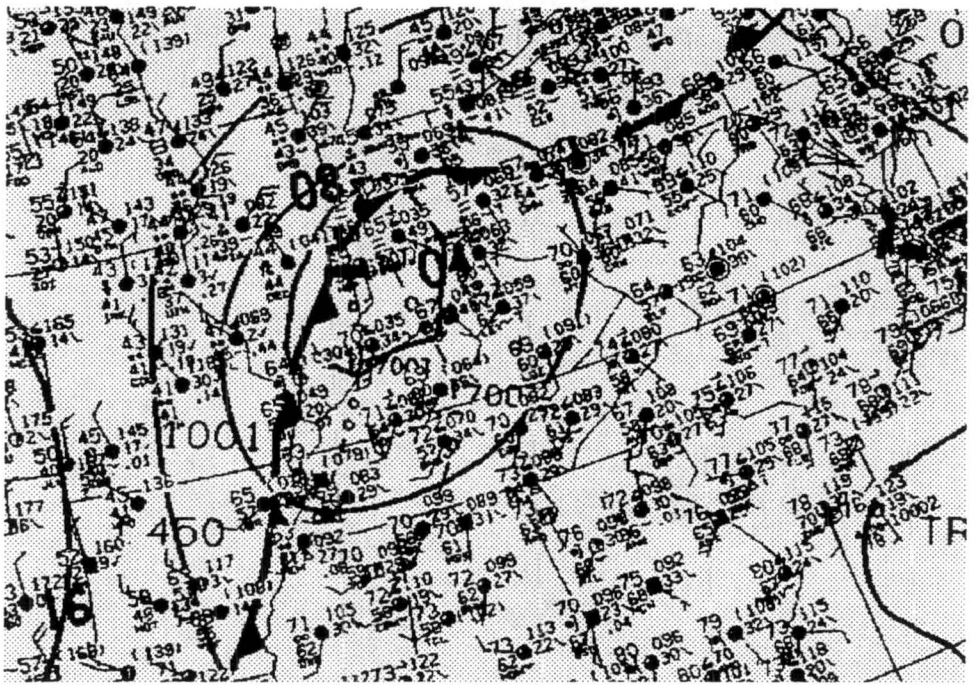

Figure 5.2: The NWS surface analysis for 2100 UTC 31 October 1994.

low 40's* immediately to the north and west of the cyclone, with stations to the east and south in the upper 50's and low 60's. The warm sector, as expected also contained higher dewpoints than the cold sector, in the upper 50's and low 60's compared to dewpoints in the 20's and 30's in the cold sector. A distinct wind shift also accompanied the passage of the cold front through the central United States as surface winds were out of the north at speeds of up to 15 knots in Oklahoma, but winds were south to southeasterly at 5 to 10 knots east of the Mississippi River.

The NWS analysis for 1200 UTC 31 October 94 also depicts a surface stationary to the north and east of the surface cyclone, extending across central Illinois, Indiana and points east. To the north of this stationary front are northeasterly surface winds at up to 15 knots, temperatures and dewpoints mainly in the 40's and a widespread area of light rain. By 2100 UTC with the low pressure center on the Indiana-Illinois border, the cold front was nearly through southern Illinois and about to cross the Mississippi River in the southern United

*Unless otherwise noted, all temperatures in this discussion are left in their original units of degrees fahrenheit.

States. Rainfall had increased to moderate intensity over northwestern Illinois and a cold pool appeared to have developed there in conjunction with the precipitation as temperatures dropped to the low 40's. Air surrounding this cold pool was in the upper 40's and 50's.

Mild, humid, and unstable air continued to flow up from the south into Indiana as temperatures now reached the low 70's with dewpoints still in the 60's. The fast moving cold front also served to trigger a line of convection throughout southern Illinois and radar summaries from 2235 UTC (Fig. 5.3) showed thunderstorm radar echoes reaching up to 25000 feet (7620 m) in southwestern Indiana with a thunderstorm watch box being placed over much of southern Indiana and northern Kentucky valid for the next several hours.

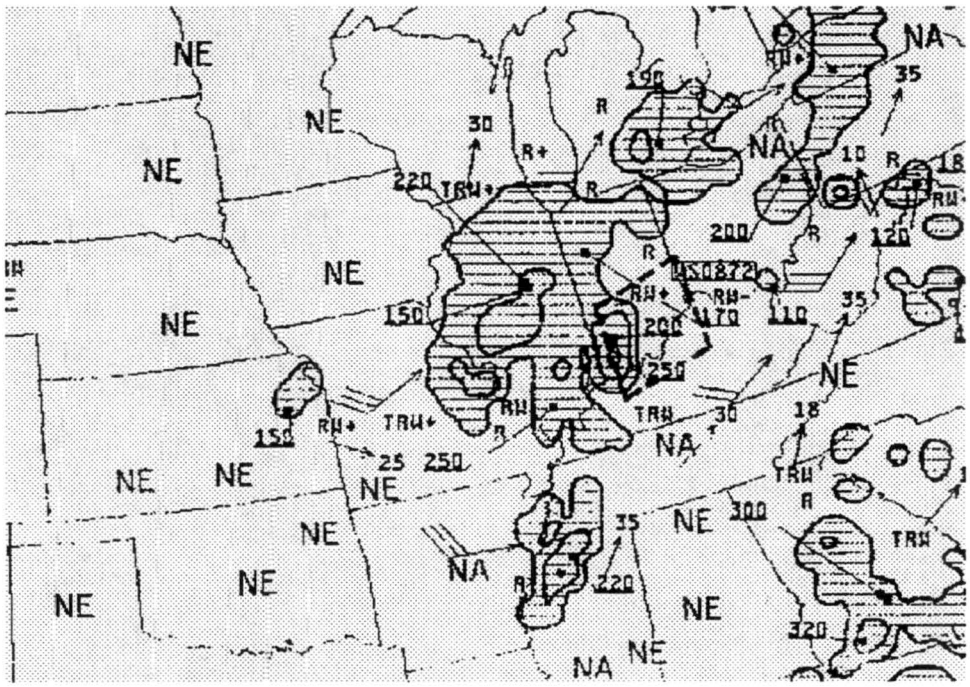

Figure 5.3: The NWS Radar Summary for 2235 UTC 31 October 1994.

The upper level winds were also conducive to cyclogenesis. The 0000 UTC 1 November 1994 upper air plots are shown since they more closely reflect the conditions to the time of the crash than would 1200 UTC 31 October 94 upper air plots. The latter of these will be discussed in Section 5.2 on model initialization. A closed cyclonic circulation extended from the surface up to about the 700 mb level (Fig. 5.4) with an open wave trough pattern at and above 500 mb (Fig. 5.5). This closed cyclonic circulation did not exist at or above 850 mb at 1200 UTC 31 October 94, thus indicating the rapid intensification of the cyclone

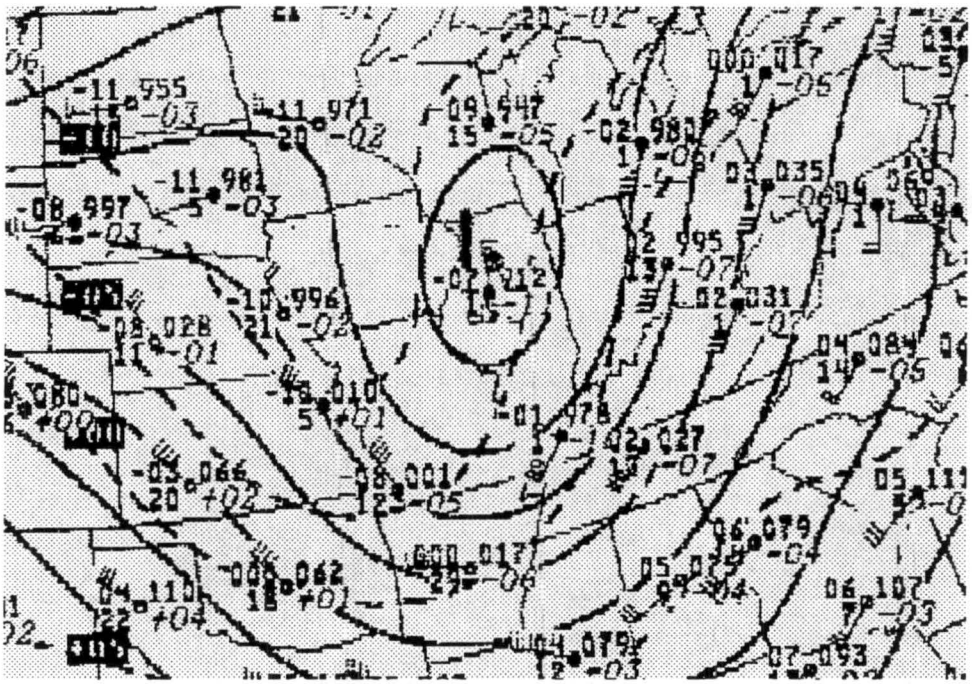

Figure 5.4: The 700mb pressure level for 0000 UTC 1 November 1994.

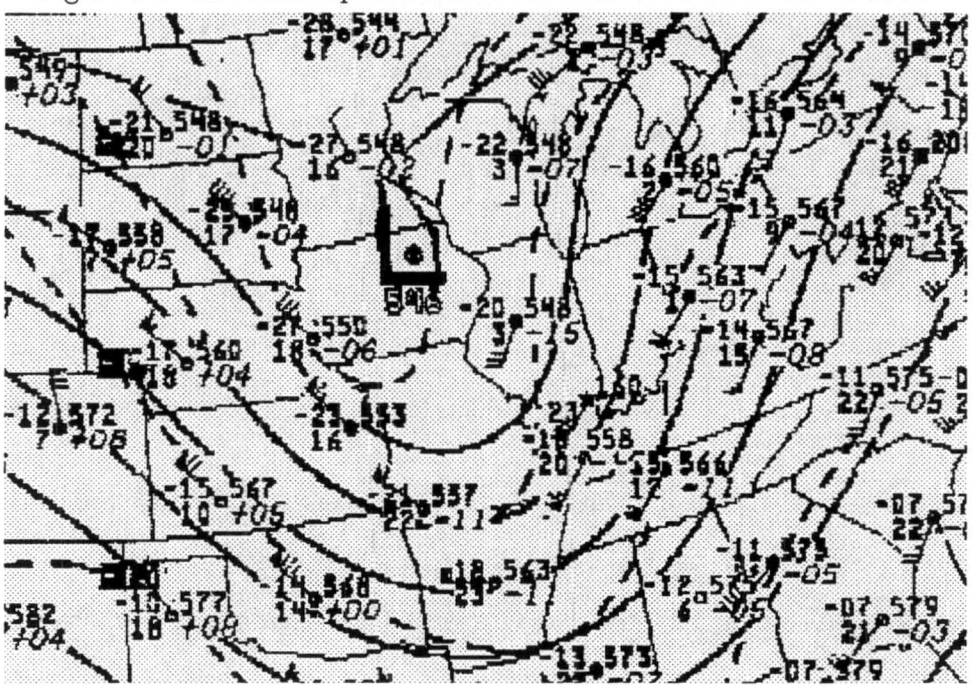

Figure 5.5: The 500mb pressure level for 0000 UTC 1 November 1994.

during this 12 hour period. The cyclone was also favorably tilted back to the northwest over cold air, with the closed cylone over northwestern Illinois at the 700 mb level at 0000 UTC 1 November 94. The upper level trough axis (300mb, not shown) fell along a north-south line from Minnesota to Louisiana. Furthermore, an intense northerly jet of 50 knots at 850 mb (also not shown) developed over northwestern Illinois which further indicates the intensification of the cyclone. Such a strong northerly jet was not present in a similar location relative to the cyclone 12 hours earlier, in fact the 850 mb winds there were only 20-30 knots.

Further information about the structure of the the cyclone can be inferred from the sounding network. While the sounding network over the United States is sparce, the midwest is no exception. There are no regular radiosondes taken in the state of Indiana, however surrounding states provide at least some information about the wind structure and moisture profiles of the storm. On 1200 UTC 31 October 94, the 700 mb plot (Fig. 5.6) showed that the sites of Paducah, KY, and Nashville, TN, had a well pronounced dry slot of dewpoint depressions of 26 and 24 °C while other stations to the north, west and east showed dewpoint depressions of less than 3 °C. As mentioned previously in Chapter 2, the presence of this dry slot fits the classical extra-tropical cyclone structure (Carlson, 1980) and the dry layer aloft is a critical component in allowing a layer of supercooled liquid water to build up with being glaciated by ice processes. Further evidence of this dry slot can be seen in the IR satellite imagery from 2200 UTC 31 October 1994. The dry slot is evident as the band of lower broken cloud tops over southern Illinois extending into northern Indiana (Fig. 5.7). Many of the cloud tops in this region can be seen to be between -5 °C and -15 °C, conditions which are generally too warm to initiate ice processes.

Information about the structure of the cyclone can also be gathered from NOAA's wind profiler network across the central United States. Unfortunately, the network does not extend much eastward beyond the Mississippi River and the closest profiler site to the crash site is in Winchester, Illinois, on the western side of the state.

The profiler site at Winchester was chosen because of its location relative to the cyclone and the fact that based upon satellite imagery the cyclone moved approximately along a line connecting the profiler and the crash site in Indiana. Figure 5.8 displays the vertical

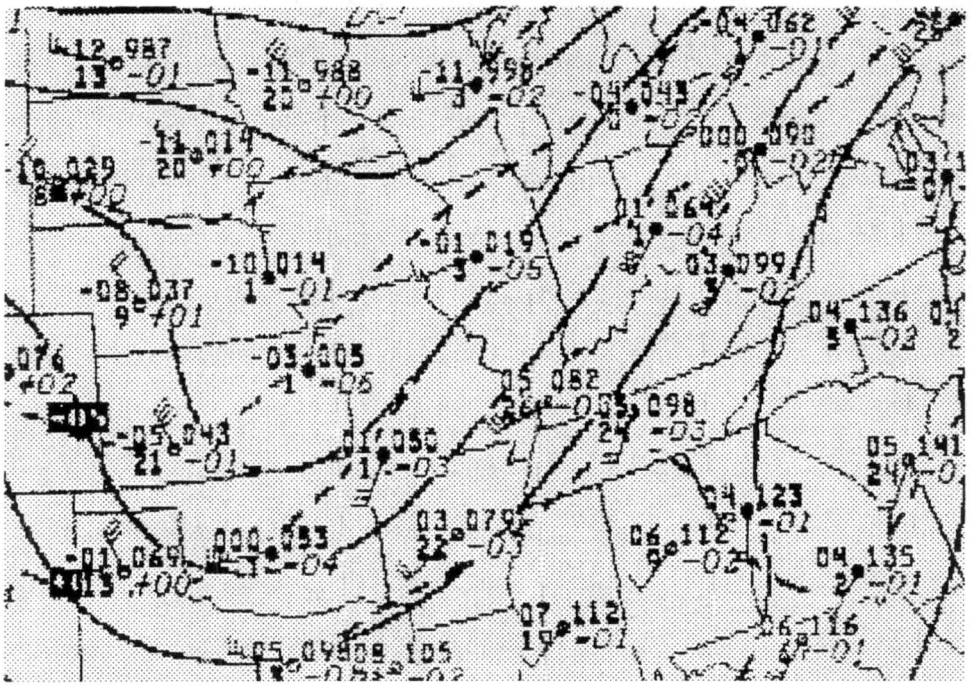

Figure 5.6: The 700mb pressure level for 1200 UTC 31 October 1994.

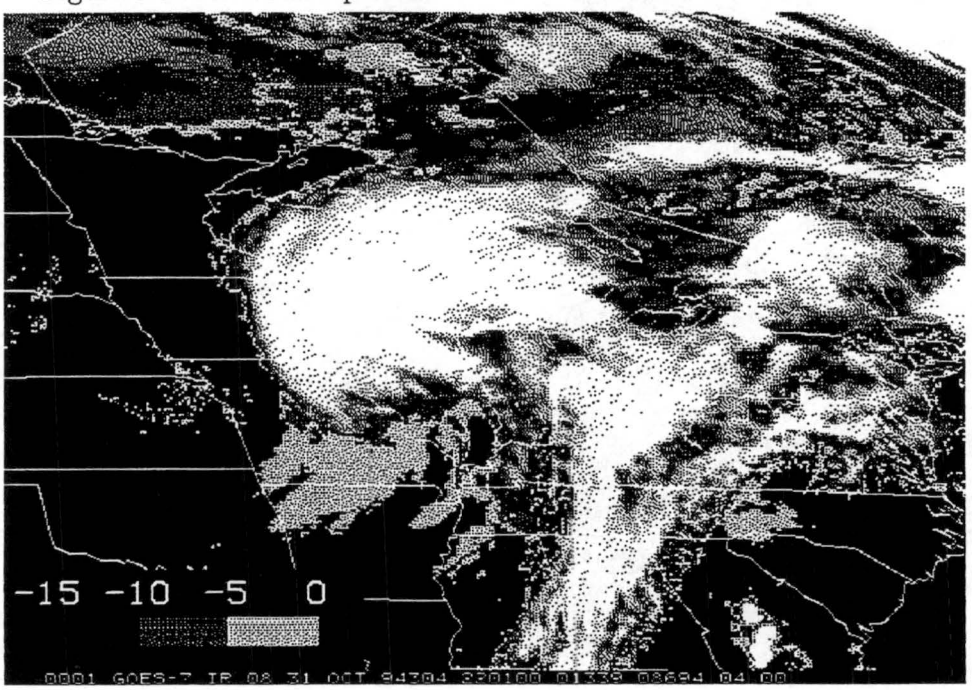

Figure 5.7: GOES-7 IR Satellite Imagery from 2200 UTC 31 October 1994. The temperature scale at the bottom left is incomplete, showing only the temperatures for the cloud tops of interest. The white cloud tops over Illinois, Wisconsin, Iowa, etc., are actually much less than -15 °C and the black areas surrounding the cyclone are actually clear skies with the ground temperatures greater than 0 °C. The scale accurately depicts the cloud top temperatures over southern Missouri, southern Illinois, and Indiana. (Courtesy of the University of Wyoming.)

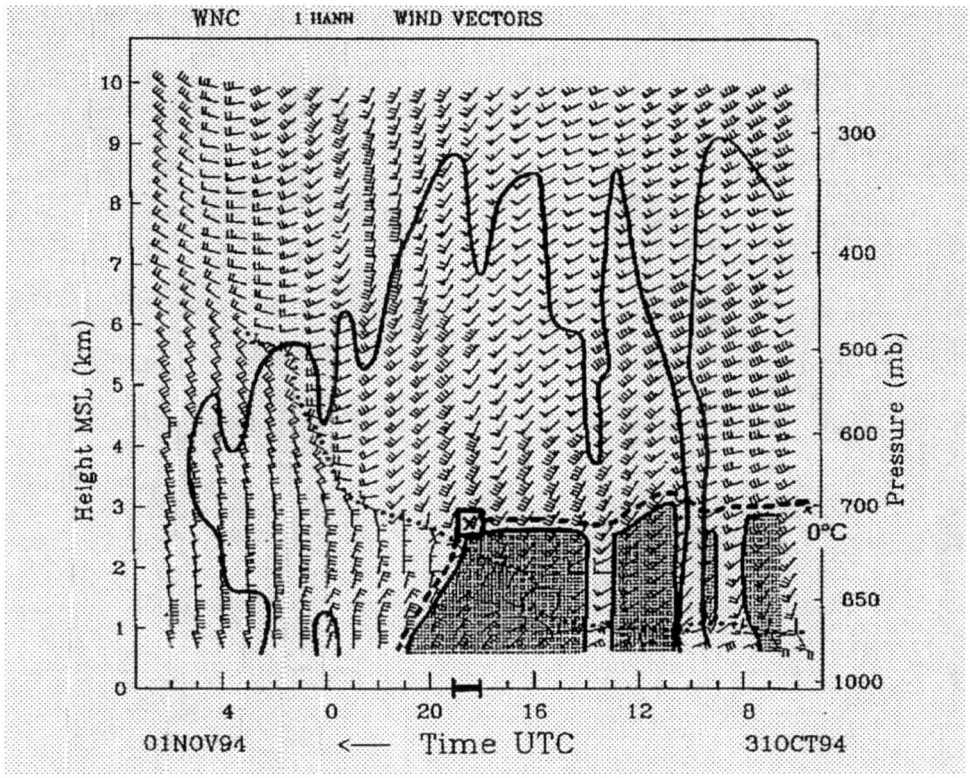

Figure 5.8: Time-Height profile of winds and other parameters from Winchester, IL radar wind profiler on 31 October 1994 and 1 November 1994. Regions of rain (shaded) and snow (unshaded, bounded by upper solid line) are shown. The dashed line represents the 0 °C isotherm, the dotted line is the zero front-parallel wind which indicated the location of the warm front aloft. The X marks the location of the maximum vertical wind shear (> 16 m s^{-1} km^{-1}) and the square surrounding the X marks the approximate height and time of the upstream-adjusted (storm relative) holding pattern (Reprinted with permission from Politovich *et al.*, 1995).

structure of the atmosphere over Winchester during the 31 October 1994 to 1 November 1994 timeframe. Of particular interest in this figure are the locations of the warm front aloft, the region of maximum vertical wind shear, and the 0 °C isotherm aloft. All these are nearly coincident with the adjusted (storm relative) location of the holding pattern translated upstream and to a slightly earlier time (1800 UTC to 1900 UTC 31 October 1994) than that of the actual crash site. It was believed that the conditions experienced over Winchester between 1800 UTC to 1900 UTC were similar to what actually occurred over Roselawn Indiana three to four hours later at the time of the airplane crash (Politovich *et al.*, 1995). As mentioned in Chapter 2, these ingredients in such close proximity to the

altitude of the holding pattern strongly suggest the likelihood of supercooled drizzle droplet production and possible icing conditions.

5.2 Model Initialization

The 31 October 1994 extratropical cyclone over the the central United States was initialized at 1200 UTC on that day, and ran out for 12 hours to 0000 UTC 1 November 1994, using standard archived synoptic scale data as described in Chapter 4. This included 2.5 degree gridded data on pressure surfaces, soundings and surface observations. The initial fields of total water mixing ratio and wind vectors are shown in Figure 5.9 and the initial temperature fields are shown in Figure 5.10, both of which are for Grid #1, 96.5m above the surface. Both of these figures display some of the surface conditions which are necessary

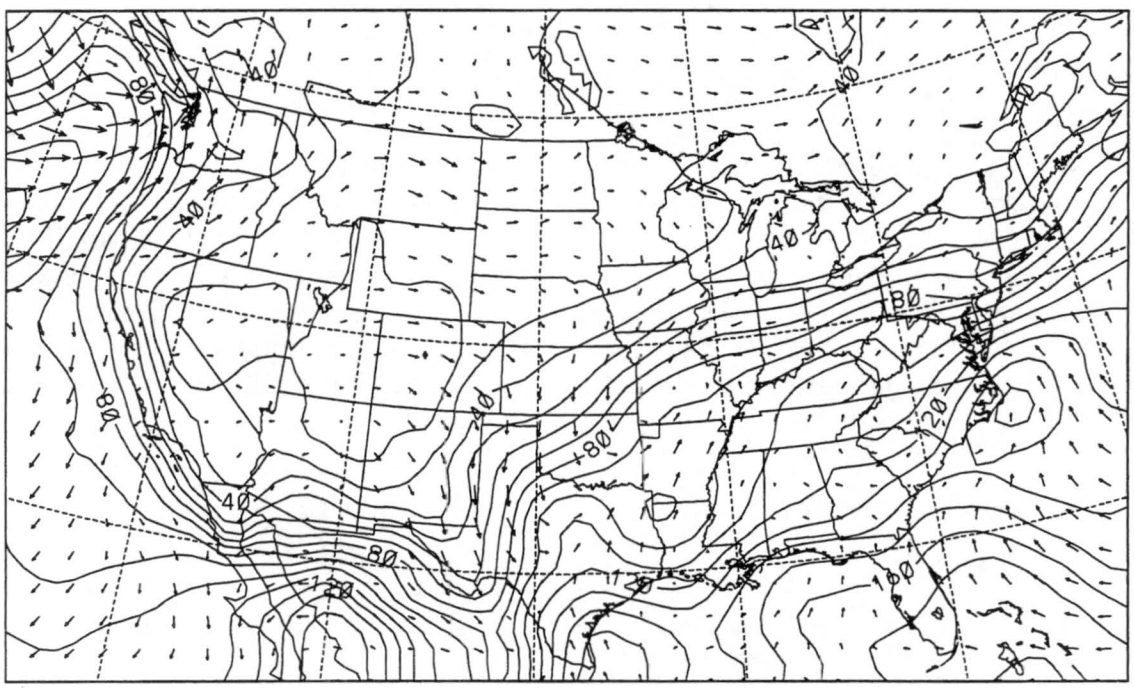

Figure 5.9: Initial Fields for 1200 UTC 31 October 1994 in Grid 1 at 96.5 meters. The solid lines are contoured every 1 g/kg and represent the total water mixing ratio. The contour labels are multiplied by 10 so a label of 80 represents a value of 8.0 g/kg. The arrows are horizontal wind vectors and a vector having a length equal to the distance between the tails of any two vectors has a magnitude of 22.1 m/s. The location of the surface cyclone can be seen in the wind vectors over southwestern to central Missouri.

for extratropical cyclone development, namely the strong baroclinic zone across the central United States combined with a strong moisture gradient across the same region.

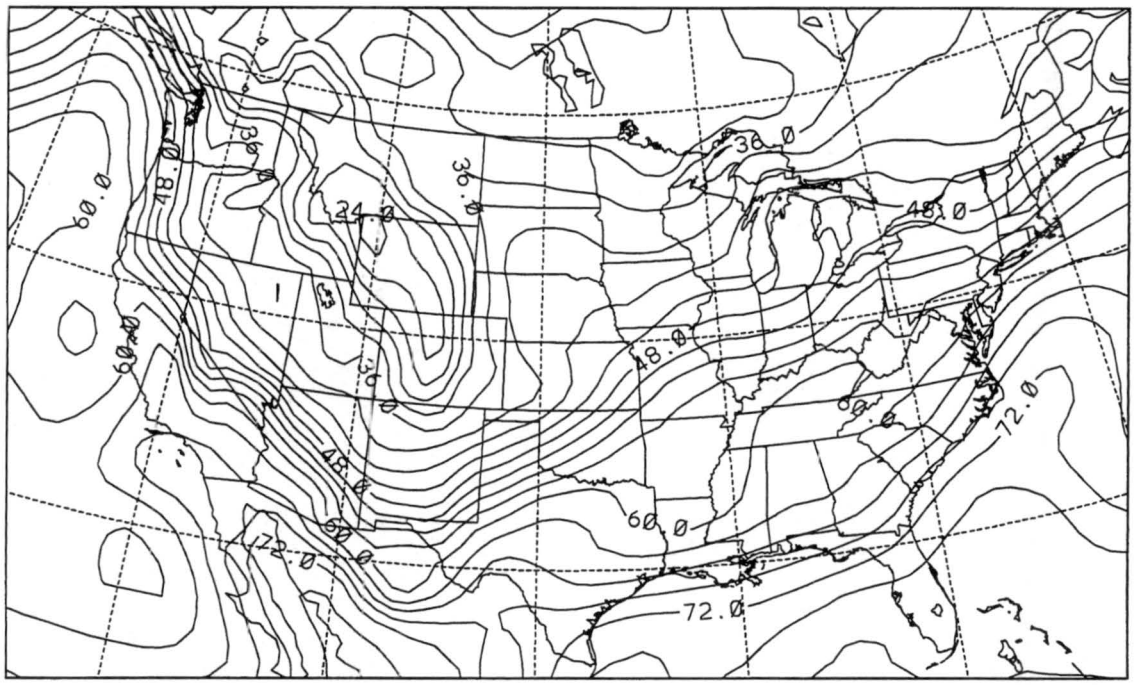

Figure 5.10: Initial field of temperature at 1200 UTC 31 October 1994 in Grid 1 at 96.5 meters. The labels are in degrees F to more easily verify against surface observations which are reported in degrees F.

The initialization of the upper levels are important to examine as well. The same fields as were examined near the surface are displayed again at the grid level of the model most closely corresponding to the altitude of flight, about 700 mb. The pressure evaluated at this grid level over the central United States was actually about 675 mb (not shown), so the figures of initial total water mixing ratio and wind (Fig. 5.11) and temperature (Fig. 5.12) are actually about 25 mb above the flight level. Therefore, the actual moisture values and temperatures would be slightly greater for the level of flight than at this grid level.

Of interest in these two figures is to note the location of the local maxima and minima of moisture and the location of the freezing line. There is a local maxima of moisture (4.8 g/kg) over southwestern Missouri and northeastern Oklahoma with a local minima (1.4 g/kg) over western Tennessee and northern Mississippi. These features will be important as they will advect to the northeast providing supercooled liquid water and the dry slot; important for icing conditions.

Two of the stations that show how the vertical profiles of moisture were initialized into the model run are shown in Fig. 5.13. The Paducah KY sounding shows a much lower

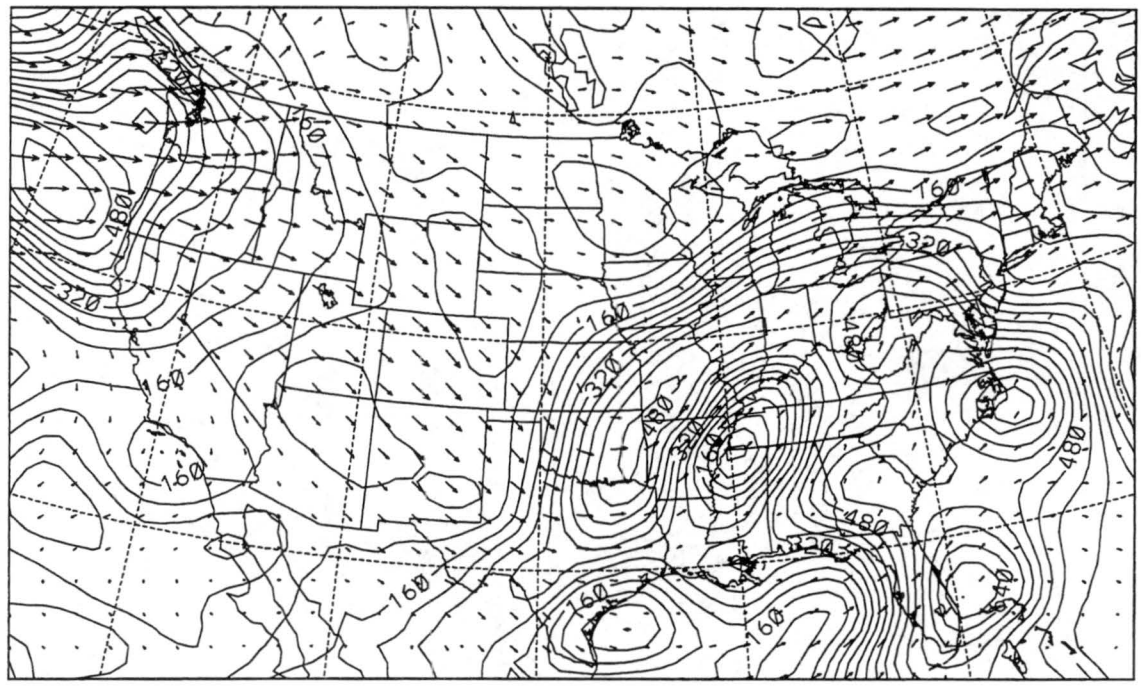

Figure 5.11: Initial Fields for 1200 UTC 31 October 1994 in Grid 1 at 3040.6 meters. The solid lines are contoured every 1 g/kg and represent the total water mixing ratio. The contour labels are multiplied by 100 so a label of 320 represents a value of 3.2 g/kg. The arrows are horizontal wind vectors and a vector having a length equal to the distance between the tails of any two vectors has a magnitude of 37.3 m/s.

cloud top elevation (as indicated by the sudden drop in RH) compared to the Dayton OH sounding. The low level cloud top at Paducah appears to be at about 800 mb whereas the same cloud top is about 600 mb over Dayton. This dry slot over Paducah is also verified upon looking at the satellite imagery (Fig. 5.7). Due to the translation of the storm during the model run to the northeast, it is reasonable to assume that this dry layer aloft advected over Indiana.

Now that the structure of the storm has been documented according to observations available, the next step will be to verify the model output against these observations. Once the verification is completed and it is determined that there is reasonable agreement between the model and observations, a more in-depth analysis of the mesoscale structure of the storm can be done in which case the icing potential based on model output and important known parameters can be evaluated.

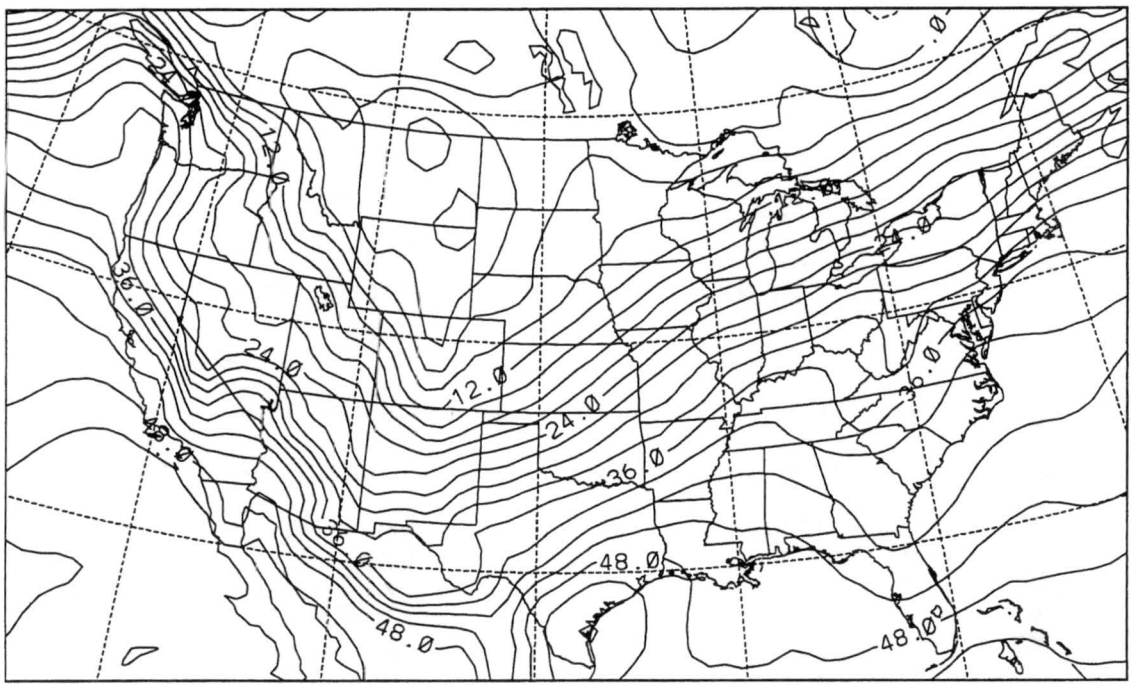

Figure 5.12: Initial field of temperature in degrees F at 1200 UTC 31 October 1994 in Grid 1 at 3040.6 meters. The freezing line at this altitude can be seen running through southeast Missouri, southern Illinois, and southern Indiana.

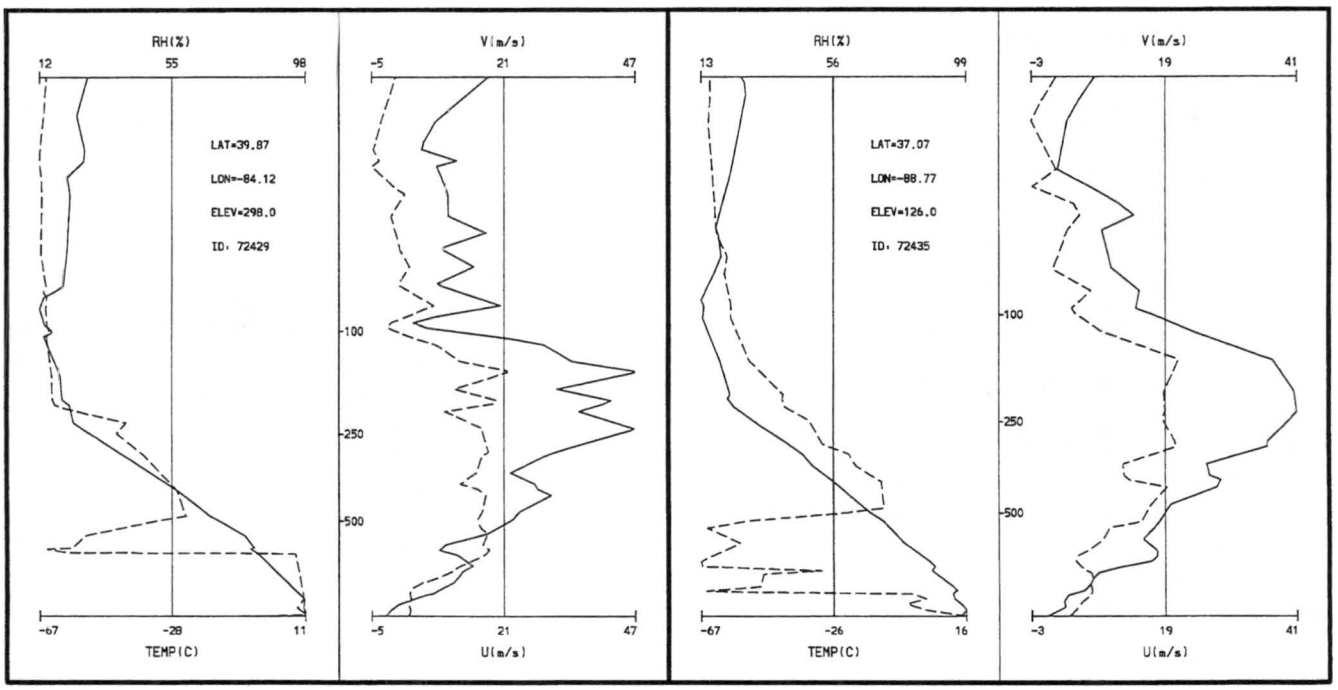

Figure 5.13: Initial Sounding Data for Dayton OH (left) and Paducah KY (right). On the left half of each plot are the Relative Humidity profile with height (dashed line) and Temperature in degrees C (solid line). In the right half of each plot are the vertical profiles of V-component of the wind (dashed line) and U-component of the wind (solid line).

Chapter 6

MODEL RESULTS AND ANALYSIS

As was described in the Chapter 4, the model code was modified by specifying the parameter which controls the number of cloud droplets or activated CCN. Most of these runs were performed in order to conduct sensitivity studies of the supercooled liquid water production during the storm on 31 October 1994. Since the environmental profile of CCN for a specific case is usually unknown, it is important to test the model with several possible CCN profiles, had the environmental profile of CCN been closer to that in one of the sensitivity studies than to the default value written in the model code. For the purposes of the discussion of initial model results, however, the default value of $300/cm^3$ will be used, and the sensitivity studies will follow in Chapter 7.

6.1 Verification

Before the results of any model run can be examined in depth, it is important to verify how well the model has performed thus far, at least in regards to certain large scale features such as temperature and wind fields, along with the track of the center of low pressure. Although the airplane crash occurred at approximately 2200 UTC on 31 October 1994, the National Weather Service plots of surface observations are only available at 3-hr intervals, and in this case the closest time is 2100 UTC. Model output from 2100 UTC will be compared to these plots.

At this same time in the model run, both the mean sea level pressure (Fig. 6.1) and temperature fields (Fig. 6.2) can be compared with the surface observations (Fig. 5.2). From the model output, the location of the center of surface low pressure was very close to the NWS analysis. If anything, the model was slightly slow, as it put the low just to the

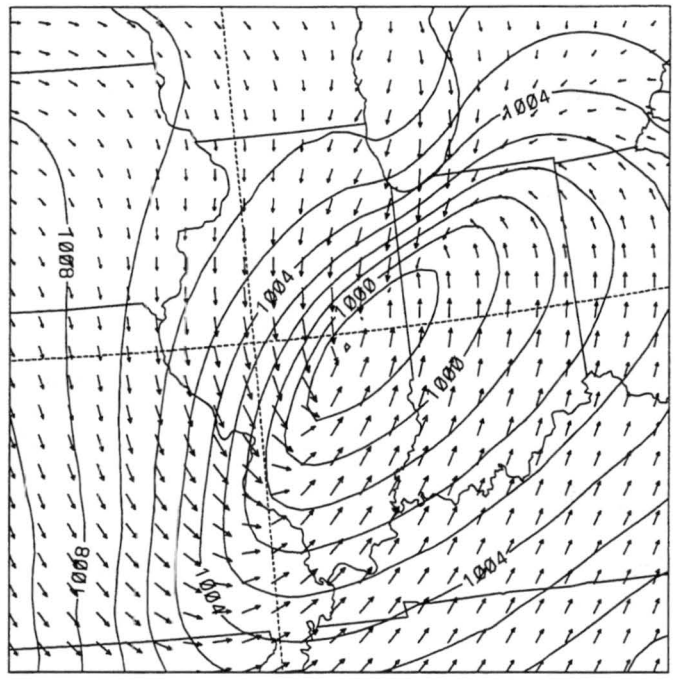

Figure 6.1: The Mean Sea Level Pressure at 2100 UTC 31 October in Grid 2. The center of low pressure was predicted to have a value of 997.5 mb. The contour interval is 1.0 mb. The arrows are horizontal wind vectors and a vector having equal length to the distance between the tails of any two vectors has a magnitude of 16.3 m/s.

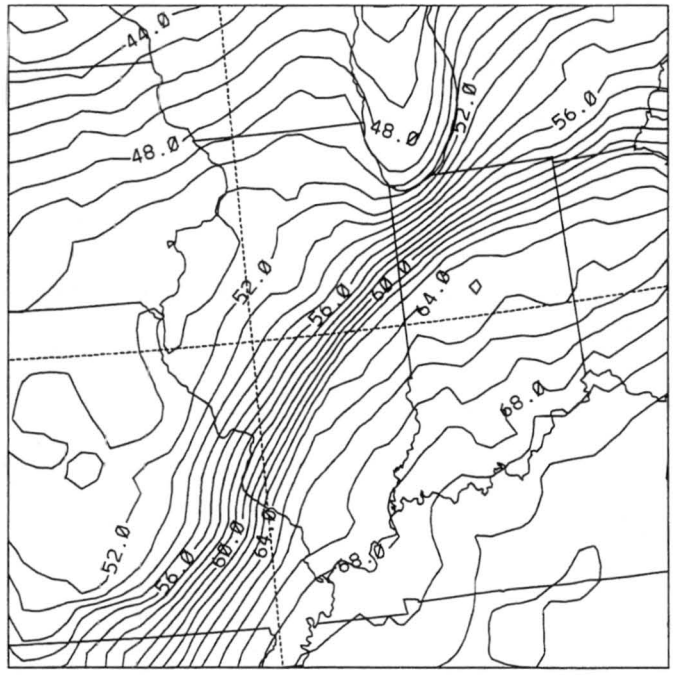

Figure 6.2: The near-surface temperatures at 2100 UTC 31 October 1994 in Grid 2, reported in degrees F.

west of the Illinois-Indiana border. The locations of the kinks in the isobars, indicating the likely position of the surface fronts does seem to agree very well with the NWS analysis.

There is some disagreement on the intensity of the low pressure center, as the NWS analysis indicated a 1001 mb low whereas the model had predicted a somewhat lower pressure of 997.5 mb. From the temperature plots, the model is in very close agreement with the surface temperatures south and east of the low pressure center in Illinois, Indiana, Kentucky and Tennessee. For example, Indianapolis reported a temperature at 2100 UTC of 65°F and the model placed the 65°F isotherm across central Indiana, for an almost perfect agreement. There is some disagreement of temperatures in the cold sector of the storm as observations across northern and western Illinois and Missouri were actually in the low 40's but the model predicted much warmer temperatures at this time in the low 50's.

Obviously then, the temperature gradient across the front in the model is somewhat in error as the cold pool behind the front does not develop to its actual full strength. The source of this error (the absence of a cold pool) appears to be a result of the model not producing enough precipitation in this region, thus evaporative cooling is not taking place forming a cold pool. According to the NWS analysis, areas surrounding the cyclone such as southern Wisconsin and Iowa, which were not receiving precipitation, appear to have nearly correct temperatures in the model, in the upper 40's and low 50's. This lack of precipitation could be the result of sub-grid scale precipitation processes such as convection not being resolved. However, this cold sector of the cyclone is not known for convective precipitation but rather stratiform precipitation. It should also be noted that the areas where the cold pool is noticeably absent such as western Illinois and Missouri are outside of Grid #3 and only has 20 km resolution, as opposed to 5 km inside of Grid #3.

The model-predicted precipitation for 2100 UTC can be seen in Figures 6.3 and 6.4, corresonding to the predicted rain and hail mixing ratios, respectively. Near the surface, the temperatures in the model were sufficiently warm to allow only these two types of precipitation. It can be seen from these two figures that at least in this basic simulation, hail was the dominant precipitation type, with the mixing ratio values having about an order of magnitude difference. In the new version of RAMS, it should also be pointed out that the hail category also represents frozen rain and ice pellets as well as partially-melted

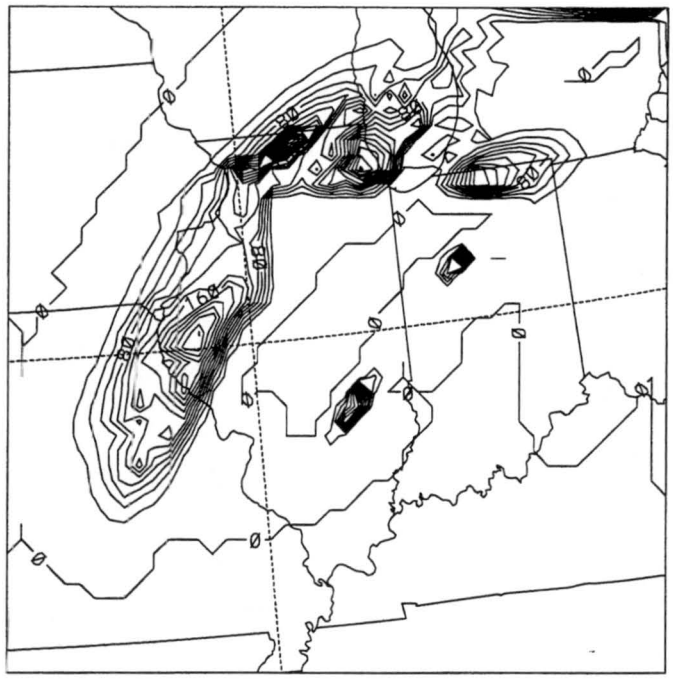

Figure 6.3: The near-surface rain mixing ratio at 2100 UTC 31 October in Grid 2. The maximum value of rain mixing ratio predicted is 0.32E-5 kg/kg with a contour interval of 0.6E-6 kg/kg. The labels are multiplied by 1E+8 so a label of 160 equals 0.16E-5 kg/kg.

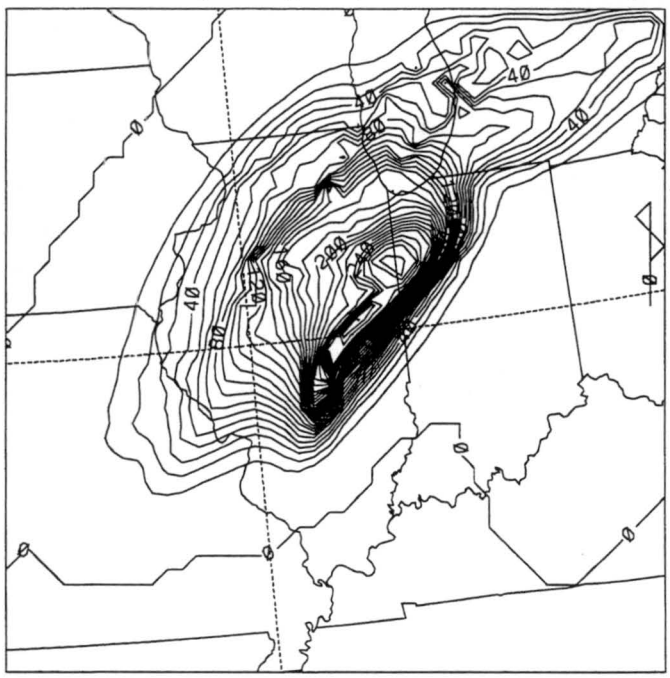

Figure 6.4: The near-surface hail mixing ratio at 2100 UTC 31 October in Grid 2. The maximum value of hail mixing ratio predicted is 0.31E-4 kg/kg with a contour interval of 0.1E-5 kg/kg. The labels are multiplied by 1E+7 so a label of 240 equals 0.24E-4 kg/kg.

species, in addition to hail (Walko *et al.*, 1995). It also can be seen in Figure 6.3 that the presence of Grid #3 and its finer resolution has an effect on precipitation type, almost completely removing the rainfall from Grid #3 (hence, the rather conspicuous 'notch' in the rain mixing ratio over north central Illinois, which happens to coincide with the northwest corner of Grid #3). This could be an artifact of the model trying to form only hail in this finer resolution area due to variations in vertical motion from one grid to another.

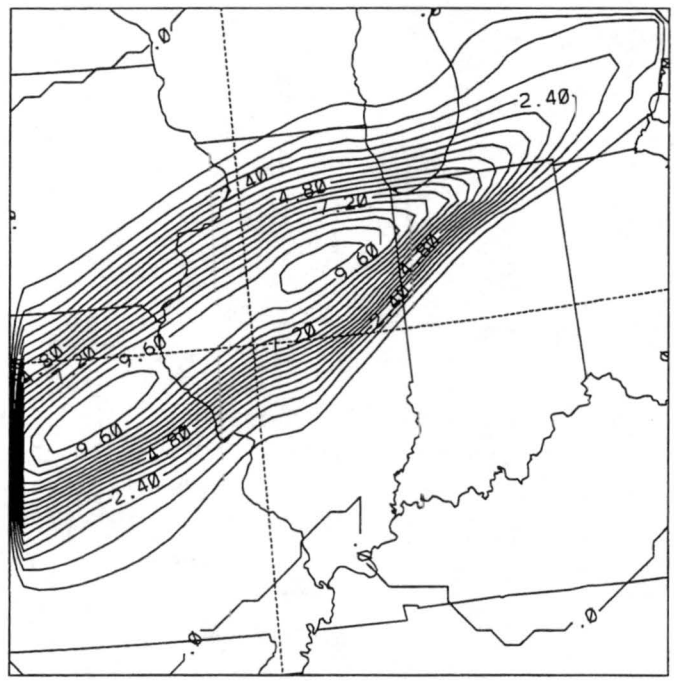

Figure 6.5: The total accumulated precipitation (all categories) at 2100 UTC 31 October in Grid 2. The maximum value of accumulated precipitation is 10.2 mm with a contour interval of 0.6 mm.

This contradicts the observations somewhat as many stations across Missouri, Illinois, and northern Indiana were reporting light to moderate rainfall amounts (Fig. 5.2). The total amount of precipitation (Fig. 6.5) in the model run was low, as much of the region was predicted to have precipitation amounts reaching 10 mm whereas summing the observations of three-hourly accumulated precipitation reported on the 2100 UTC surface plot (Fig. 5.2) as well as for 1500 UTC and 1800 UTC (not shown), ranged between 1.0 to 1.5 inches (25 to 38 mm) across the same region. Furthermore, the precipitation type was wrong, which is evidenced not only in the rain and hail mixing ratio plots (Figs. 6.3 and 6.4 respectively) but also in the accumulated rain and hail precipitation plots (Figs. 6.6 and

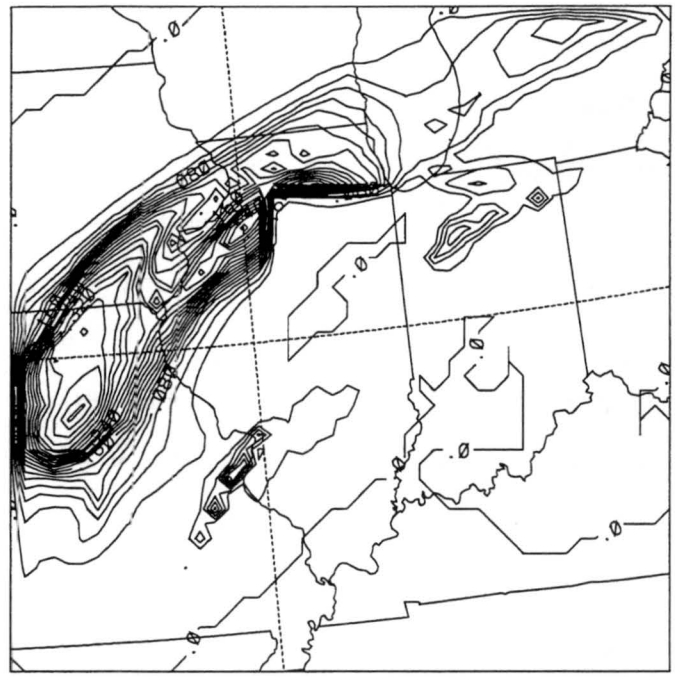

Figure 6.6: The accumulated rainfall at 2100 UTC 31 October in Grid 2. The maximum value of accumulated rainfall is 0.42 mm with a contour interval of 0.02 mm.

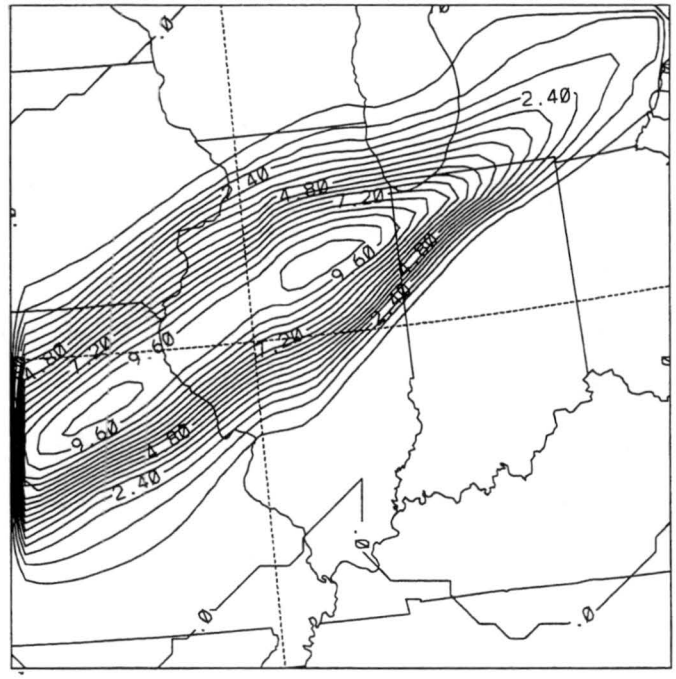

Figure 6.7: The accumulated precipitation from hail at 2100 UTC 31 October in Grid 2. The maximum value of accumulated hail is 10.2 mm with a contour interval of 0.6 mm.

6.7 respectively). This discrepancy reflects some of the problems with the microphysics in this version of RAMS, and a coding error in the precipitation sedimentation algorithm near the ground where grid-spacing is stretched has recently been discovered which is a possible source of these problems. While there was not sufficient time to completely rerun all the simulations required for this thesis following the discovery of this coding error, a rerun of the basic run did show improved results in both precipitation amounts (maximum values of total precipitation of about 30 mm, much closer to the observations, were now being forecast), and in the temperature field behind the cold front where a cold pool was not sufficiently developed before. Fortunately, the cloud water field was not significantly impacted by this error and thus the results from the orignal basic run are presented. In an attempt to compensate for the precipitation-type problem, a no-hail case was also run and will be discussed with the rest of the sensitivity studies in Chapter 7.

6.2 Model Results

Now that the overall synoptic scale structure of the storm in the model appears to be in somewhat reasonable agreement with the observations (keeping in mind, that this is only a model), the mesoscale structure of the storm needs to be examined to determine the possible conditions at the time and flight level of the doomed aircraft. Many of the following figures will be shown at the 700mb pressure level, as it was documented that the aircraft had been flying at this altitude on the flight to Chicago and also while in the holding pattern over Roselawn, Indiana where it eventually crashed (Politovich, personal communication). It should also be noted at this time that the 700mb level figures are made by interpolating the model output from the nearest vertical grid levels immediately above and below this pressure level, as RAMS does not have the ability to predict for specified altitudes.

As was noted in Chapter 5, the region of interest contained a rapidly developing mid-latitude cyclone with a swift moving cold front pushing through southern Illinois on 31 October 1994. Out ahead of this cold front in the warm sector, was a region of mild and relatively unstable air advecting up from the south. The convective available potential energy (CAPE) at 2200 UTC was analyzed by the model and is shown in Figure 6.8. Although the values predicted are not unusually high, only between 300-400 J/kg ahead of

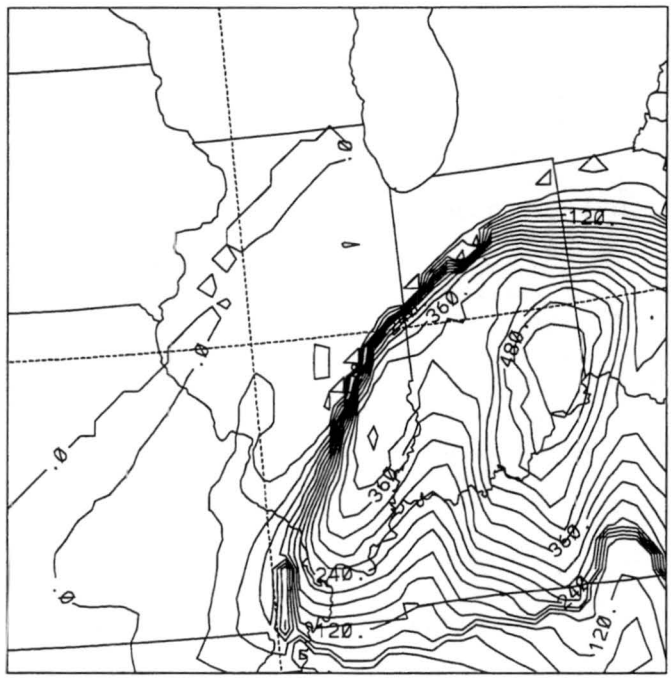

Figure 6.8: The Convective Available Potential Energy (CAPE) in Grid 2 at 2200 UTC in units of J/kg. The maximum value is 540 J/kg with a contour interval of 30 J/kg.

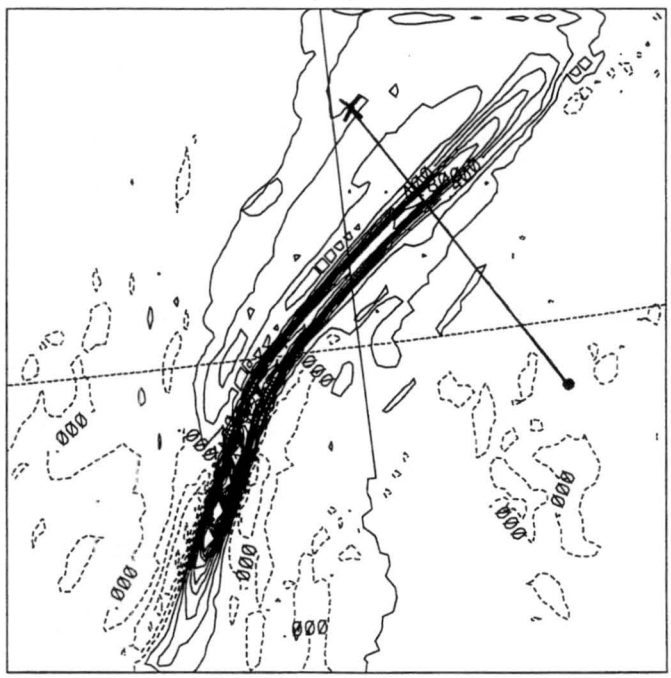

Figure 6.9: The vertical component of motion, w, in units of m/s analyzed at p=700mb in Grid 3 at 2200 UTC. The maximum upward vertical velocity is 1.6 m/s, with a contour interval of 0.1 m/s. The location of the flight path on this and the remainder of the Grid 3 figures is indicated by the southeast-northwest line, with the 'X' indicating the crash site.

the cold front, the fact that there are some positive values of CAPE indicates that there is instability for the convection to develop, assuming there exists a strong trigger mechanism. In this case, the fast moving cold front acted as the trigger for a line of convection and the vertical velocities are shown in Figure 6.9. Although the actual values of vertical velocities are probably limited by the 5 km horizontal grid resolution in Grid #3, they were never the less predicted to reach a maximum value of 1.6 m/s within the convective line. The actual values within the updraft were likely somewhat stronger than this, however, they were probably also limited by the relatively weak values of CAPE. This convection was strong enough to supply moisture to the mid and upper levels of the storm system, whereupon the moisture was likely advected downstream to the northeast with the mean flow through the storm. As can be seen from Figure 6.9, the vertical velocity 'ridge' extended to the northeast into northwestern Indiana with updrafts of generally less than 1 m/s, however these updrafts combined with the horizontal moisture advection from the southwest supplied additional moisture to the region over northwestern Indiana.

The moisture supply is illustrated through both Figures 6.10 and 6.11, the relative humidity (RH) and cloud water mixing ratios respectively. First, upon examining the RH plot in Grid #2, there is a large area of 100 % RH extending from southern Illinois across northwestern Indiana into southern Michigan, in a pattern consistent with the convection and horizontal advection of moisture through the storm. The cloud water mixing ratio plot for Grid #3 also displays the horizontal wind vectors present in the region advecting the moisture. It can be seen that both the horizontal advection and vertical updrafts supplying the midlevels with their moisture are nearly aligned along with the maxima in cloud water mixing ratio, thus resulting in a relatively narrow band of enhanced cloud water being advected into northwestern Indiana, directly into the flight path of the aircraft (see Figure 4.2 again for locations of crash site and Indianapolis within Grid #3). The cloud water mixing ratios over northwestern Indiana, while not as high as in the region of strongest convection to the southwest in Illinois, do indicate liquid water amounts which should be high enough for icing conditions.

Lewis (1947) established general guidelines for the severity of icing based on liquid water content (LWC) and mass mean diameter (D_m). For D_m greater than 18 μm (which will be

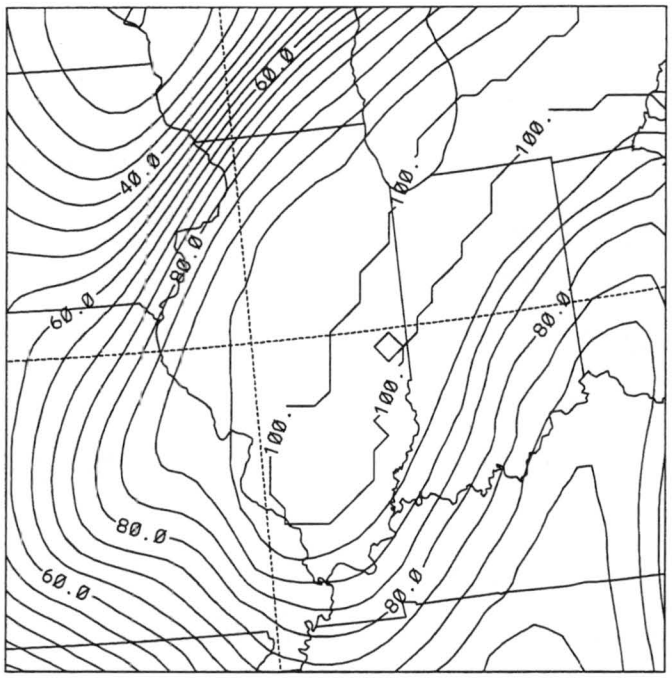

Figure 6.10: The percent relative humidity (RH) analyzed at p=700mb in Grid 2. The maximum value of percent RH predicted is 100, with a contour interval of 5.

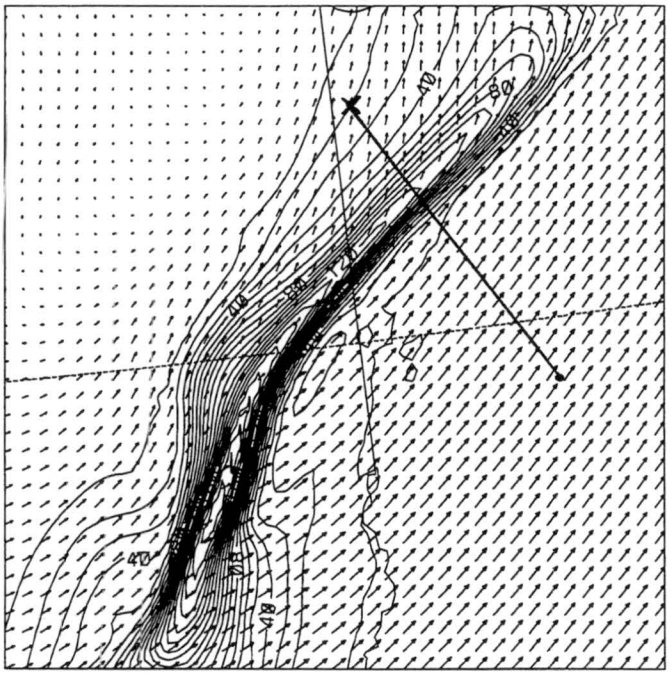

Figure 6.11: The cloud water mixing ratio in units of g/kg analyzed at p=700mb in Grid 3. The maximum value of cloud water mixing ratio predicted is 2 g/kg, with a contour interval of 0.1 g/kg. The labels are multiplied by 0.1E+6 so a label of 80 corresponds to a value of 0.8 g/kg. The arrows are horizontal wind vectors and a vector having a length equal to the distance between the tails of any two vectors has a magnitude of 24.9 m/s.

shown to be true in this case), icing encounters were classified as severe if LWC exceeded 1 g/m^3, moderate for LWC greater than 0.5 g/m^3 but less than 1.0 g/m^3, and light for LWC greater than 0.2 g/m^3 but less than 0.5 g/m^3. The mixing ratios plotted on Figure 6.11 are plotted in units of g/kg, however doing a simple units conversion by multiplying by the density of air at p=700mb ($\rho \cong 0.9$ kg/m^3), the LWC in this case is indeed greater than 0.5 g/m^3 over the area on Figure 6.11 bounded by $\sim$ 0.55 g/kg and LWC is greater than 1.0 g/m^3 over the area bounded by $\sim$ 1.1 g/kg. From these threshold values of LWC, one can deduce a relatively broad area of potentially moderate icing surrounding a narrower band of potentially severe icing, both of which the aircraft in question would have likely flown through or loitered in while in the holding pattern.

The next important step in the analysis of model output is to determine how likely the production of large supercooled liquid water droplets is, given the ambient atmospheric conditions, at least as they are predicted by the model. As was discussed initially back in Chapter 2, the vertical wind shear combined with the thermodynamic stability of a layer in the atmosphere can be combined to calculate the Bulk Richardson number (see Equation 2.1). Both the Bulk Richardson number and the vertical wind shear (Figures 6.12 and 6.13, respectively) have been computed from the pertinant gridded data available in the model. As previously discussed, large droplets preferentially form in regions where the Bulk Richardson number is less than 1, with a vertical wind shear value of 0.02 s^{-1}. While it is possible to compute values based on gridded data, the vertical resolution of the model at this pressure level is actually about $\Delta z = 600$ m. This is relatively course resolution when in fact the shear layers in question can have a depth as shallow as $\Delta z = 100$ m (Pobanz *et al.*, 1994).

For these reasons, both the plots of Richardson Number and vertical wind shear, while still providing useful information for this study need to be viewed with caution. If, for example, the same θ gradient and $\vec{V}$ gradient between grid levels is actually confined to a much thinner layer than the model can actually resolve, the Δz dependence of the wind shear would increase the value of shear for the same shear vector confined to this thinner layer. Similarly, the Bulk Richardson number would be decreased by the same argument. Keeping this vertical resolution issue in mind then, one should examine Figure 6.12 looking

instead for diagnosed 'minima' in Ri, realizing that the value in reality is likely to be less than as diagnosed perhaps by as much as 1/6th. Likewise, upon examining the vertical wind shear values in Figure 6.13 and locating the 'maxima' diagnosed by the model, the values here are likely to be stronger in reality than as diagnosed, this time perhaps by as much as 6 times greater. With this now in mind, it is easy to see that the 'adjusted' values of wind shear and Richardson number over most of the Grid #3 domain and especially over northern and central Indiana would easily satisfy the criteria established by Pobanz *et al.* (1994) in which large droplets would form.

The value of Richardson number over the crash site as diagnosed by the model is approximately 5, with a minimum value of less than two just to the north and east. The value of vertical wind shear over the crash site appears to be about 0.014 s^{-1}, with slightly stronger shear also to the north and east. Since the margin of error was shown to be on the order of a factor of 6, the values required by Pobanz *et al.* to form large droplets easily fit into this margin. Further evidence which should validate the model output would be to recall the wind profiler data from Winchester, Illinois (Fig. 5.8). The maximum value of wind shear observed here was 0.016 s^{-1} at approximately the 3 km (p=700mb) level which was argued to adjust to the northeast with the storm. Allowing for the intensification of the storm which was both observed and modeled successfully, an increase of shear to over 0.020 s^{-1} in Grid #3 (northeast corner of Figure 6.13) is conceivable.

Now that it is well established that there is sufficient cloud water present to create hazardous icing conditions at the time and location, it is also important to examine two other properties equally important to determine the icing potential, temperature and diagnosed droplet size. Figures 6.14 and 6.15 display both the mass mean diameter and air temperature, respectively. The mass mean diameter was computed as discussed in Chapter 4 using Equations 4.2 and 4.3. A cautionary note should be made here as well about the calculation for mass mean diameter; the size is based on maintaining a constant activated CCN profile in the horizontal, the vertical, and in time. It is probably not a good assumption that the profile is constant in the vertical as CCN concentration likely tends to decrease away from the surface toward cleaner air. Likewise, in time this would not be a good assumption either as turbulent motions, as was just discussed, forcing collision and coalescence would

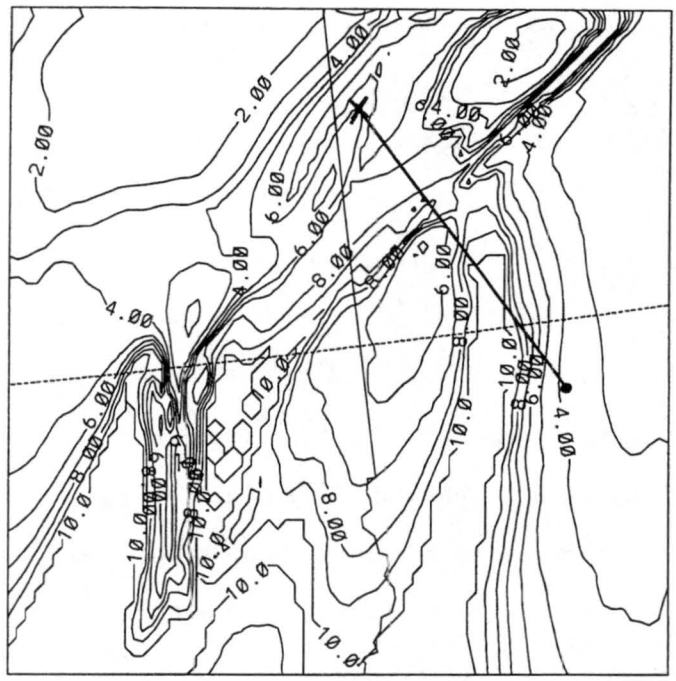

Figure 6.12: The Bulk Richardson Number, Ri, at p=700mb in Grid 3. The minimum value analyzed is 1.0.

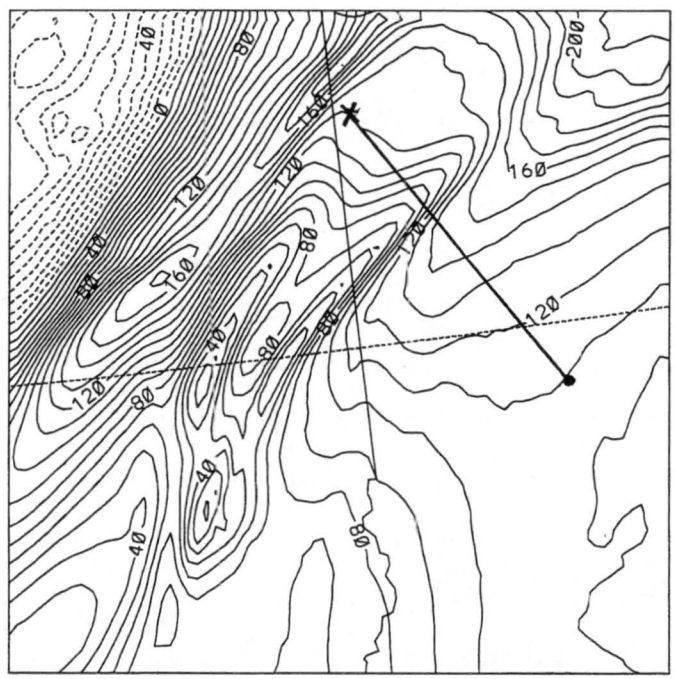

Figure 6.13: The vertical wind shear in units of (m/s)/m, or s^{-1}. The minimum value of vertical wind shear is -0.009 s^{-1} and the maximum being 0.021 s^{-1} with a contour interval of 0.001 s^{-1}. The labels are multiplied by 0.1E+5 so a label of 120 corresponds to 0.012 s^{-1}.

serve to decrease the number of cloud droplets or activated CCN, thus increasing the mean diameter given the same amount of cloud water. Therefore, the mean diameter plotted is likely to be a minimum possible value and in reality the diameter could be somewhat larger than as diagnosed by the model. On the other hand, regions such as the convective line along the frontal boundary are also characterized by higher supersaturations along with high concentrations of cloud droplets, an effect that would reduce the mean diameter in these regions.

The values of mass mean diameter are all in the size range which would allow for icing to occur, with values over a large area of D_m greater than 24 μm, which satisfy the Lewis criteria of needing to be larger than 18 μm for the cloud water mixing ratios predicted in Figure 6.11. The most hazardous icing, known to be caused by large droplets, are said to be in the 30 μm to 250 μm size range (Pobanz *et al.*, 1994). Even going with this more restrictive criteria, large areas of Grid #3 surrounding the convective line and downstream advective region are seen to have mass mean diameter larger than 30 μm.

Since it has been shown that more severe types of icing generally occur with these larger droplets, it is useful to know what portion of the total cloud water mixing ratio they comprise. Calculations were made using the gamma distribution, integrating from a minimum value of 30 μm up to infinity in which the number of droplets were counted as well as summing up the mass of these droplets. A complete derivation of the equations used to calculate these parameters (N_t and r_c of droplets greater than 30 μm) is outlined in Appendix A, as well as summary tables of these numbers for the basic run and all the sensitivity runs.

For this case, see Table A.1. It can be seen, for example that with N_t=300/cm^3, ν=1, and r_c=1.2 g/kg (an average value from the cloud water plots), that there are about 19/cm^3 droplets larger than 30 μm and the mixing ratio of their mass only is 0.84 g/kg in a perfect gamma distribution. The calculation for D_m under these conditions was also made and was shown to be 39.82 μm. This value of r_c comprises 69.91% of the total mixing ratio of 1.2 g/kg. Compare this to the maximum value of 2.5 g/kg of cloud water (bottom row of Table A.1 and maximum value of cloud water mixing ratio encountered on any of the cloud water

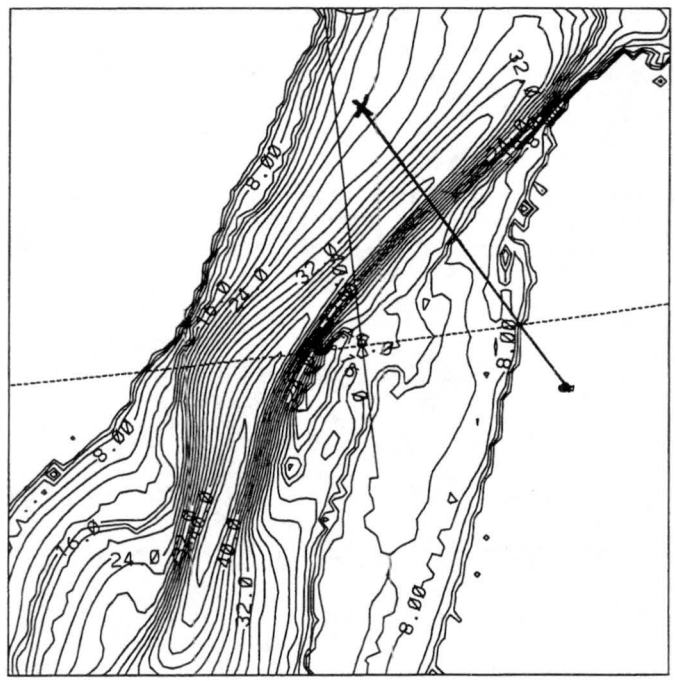

Figure 6.14: The mass mean diameter of cloud water droplets in units of μm at p=700mb and in Grid 3 (using cloud water mixing ratios in Figure 6.11 and N_c=300/cm^3). The maximum diameter predicted is 46 μm with a contour interval of 2 μm.

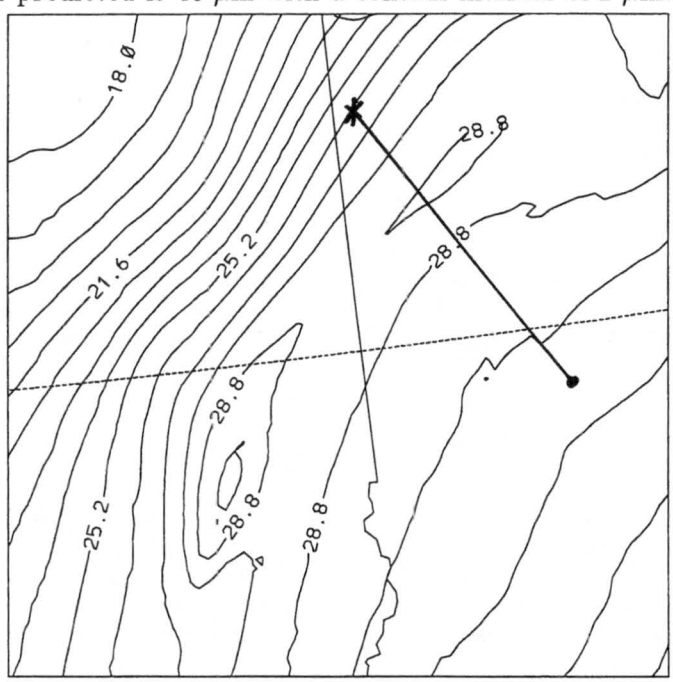

Figure 6.15: The air temperature in degrees Fahrenheit at p=700mb in Grid 3. The maximum temperature predicted is 32.4 F with a contour interval of 0.9 F.

plots) where there are 34 droplets greater than 30 μm, r_c of these droplets is 2.06 g/kg, D_m=50.86 μm, and the amount of r_c in droplets larger than 30 μm is 82.58%.

Also, at the very low end of the r_c spectrum, with r_c = 0.1 g/kg, there is less than 1 droplet greater than 30 μm (on average), there is only about 0.01 g/kg of water contained in it, D_m = 17.39 μm (much less than the 30 μm required to be considered a large droplet), and only 12.36% of the water is contained in the largest droplet, if in fact it exists at all in this distribution. Thus, it can be seen that the icing hazard increases dramatically with increasing r_c, as more and more of the total cloud water becomes contained in droplets greater than 30 μm.

The temperature at this altitude can also be examined (Fig. 6.15) which shows that most of the temperatures across Grid #3 were indeed below freezing. Perhaps somewhat limiting in this field is that the model-predicted temperatures, while below freezing, are only a few degrees Fahrenheit below freezing especially in the same regions of highest liquid water content (the warm bubbles contained by the 28.8 F (-1.8 C) contour correspond to the convective regions). As was noted earlier, the air temperature needs to be sufficiently below freezing, to allow for the possibility of freezing when the effect of dynamic warming due to the aircraft's airspeed is taken into account. With temperatures at this elevation in the upper 20's (degrees Fahrenheit) corresponding to the maximum cloud water and droplet size areas, this would suggest that icing potential is somewhat reduced in this region. However, since the air is still below freezing, there is the possibility for run-back icing, or clear ice along the fuselage away from the leading edge of the aircraft. To the north and west of the warm bubble in northwestern Indiana, the temperature is predicted to drop rapidly to 25 F (-3.9 C) or less very near the location of the crash site, a temperature that would favor icing more strongly than near the convective region. Once again, however, keeping in mind the vertical grid resolution and not knowing the exact altitude of the aircraft relative to the model grids (only approximate values of 700mb being known), the icing potential even in this warm bubble region would be increased significantly had the aircraft actually flown somewhat higher than this altitude, even by just a few hundred meters. The moist adiabatic lapse rate would allow for about a 0.66 C degree cooling for every 100 meters above the actual 700mb level. So, the aircraft would not have needed to be substantially

higher in order to justify saying that the icing potential encountered by the aircraft could have been substantial instead of marginal.

Additional information about the structure can be gained by examining a few vertical cross-sections through the storm. Figures 6.16 and 6.17 correspond to the vertical cross-sections of cloud water and vertical velocity through Grid #3, looking west. The cross section actually passes through the crash site from north to south (so these cross-sections run just to the east of the Illinois-Indiana border). The crash site is located to the north of both the vertical velocity maximum (corresponding to the general location of the warm front and its convection) and the cloud water maximum, which the aircraft would have had to fly through coming from Indianapolis. Since the aircraft was actually on a southeast to northwest oriented flight path before being put into the holding pattern, the aircraft would have actually flown through the convection and cloud water maxima to the east of X=927.5 km. These maxima can be seen in two nearly identical figures at X=967.5 km (Figures 6.18 and 6.19). Although the cloud water maximum is nearly the same in both figures, the updraft maximum is slightly weaker at 3.2 m/s in this more easterly cross section. The region in which the aircraft could have experienced icing would like be between these two sets of cross-sections.

6.3 Potential Accumulation

The concept of potential accumulation was touched on in Chapter 2 in which the potential accumulation of ice (thickness of ice per unit cross-sectional area) is related to the amount of cloud water swept up by a unit cross-sectional area of aircraft during flight, as well as the density of the type of ice to be expected (low density for rime ice, high density for clear ice). Potential accumulation then is calculated to be the path integral of cloud water swept up by the aircraft, and then taking the predicted meteorological conditions (i.e. temperature, mass mean diameter, and cloud water mixing ratio) to predict which type of ice is to be expected, and then divide the path integral of accumulated cloud water by that density. This calculation also assumes a collection efficiency of the aircraft to be one, not a very realistic assumption under certain conditions but better in others. The aerodynamics

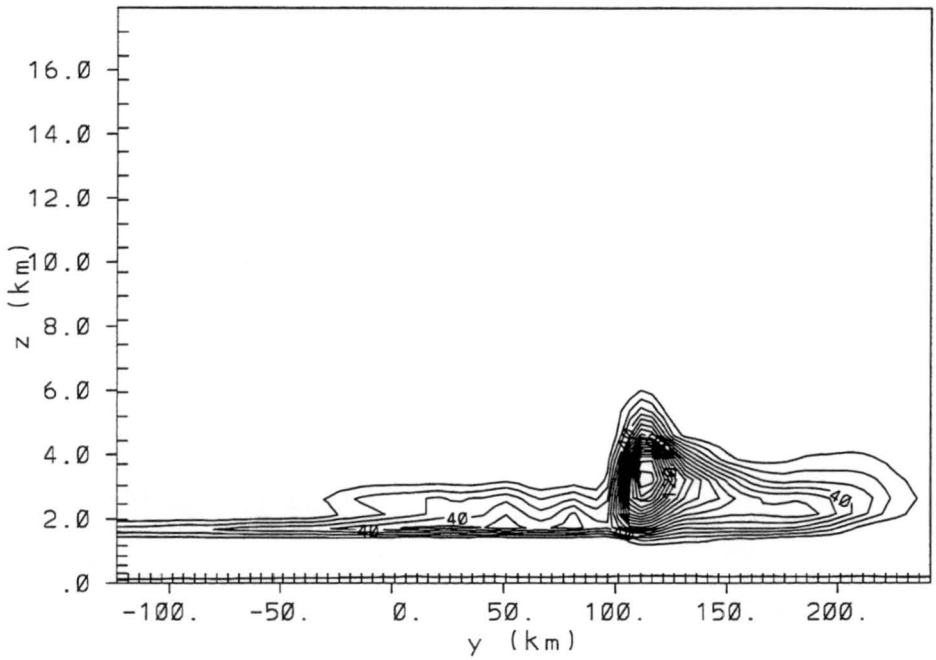

Figure 6.16: North-South cross-section (looking west) of cloud water mixing ratio at X=927.5 km in Grid 3. The maximum value diagnosed is 1.9 g/kg with a contour interval of 0.1 g/kg. The labels are multiplied by 0.1E+6 so a label of 40 corresponds to 0.4 g/kg. The crash site is along this cross-section at approximately Y=+175 km.

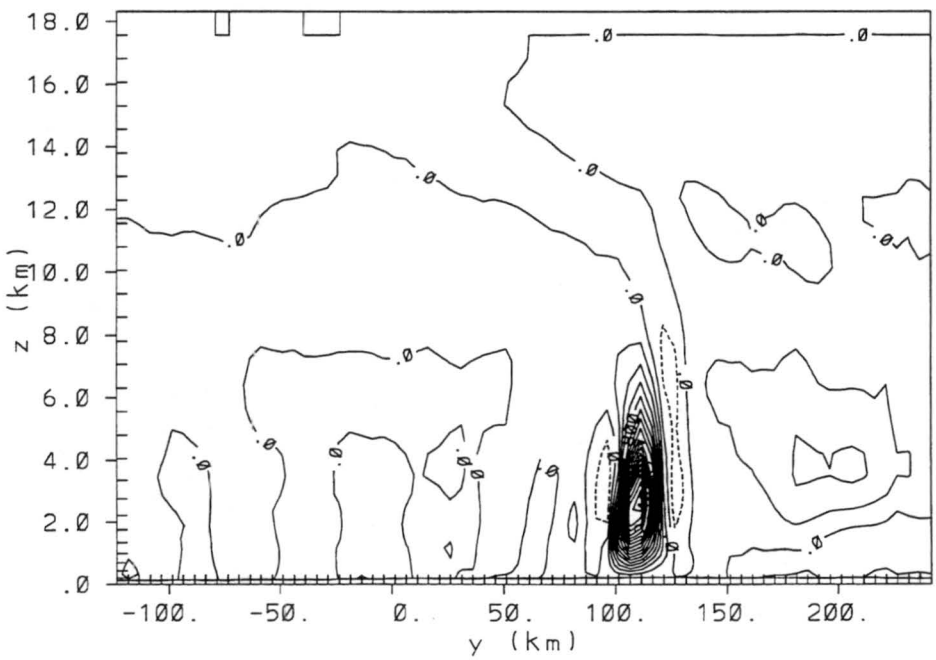

Figure 6.17: North-South cross-section (looking west) of vertical velocity, w, at X=927.5 km in Grid 3. The maximum value predicted is 3.4 m/s with a contour interval of 0.2 m/s.

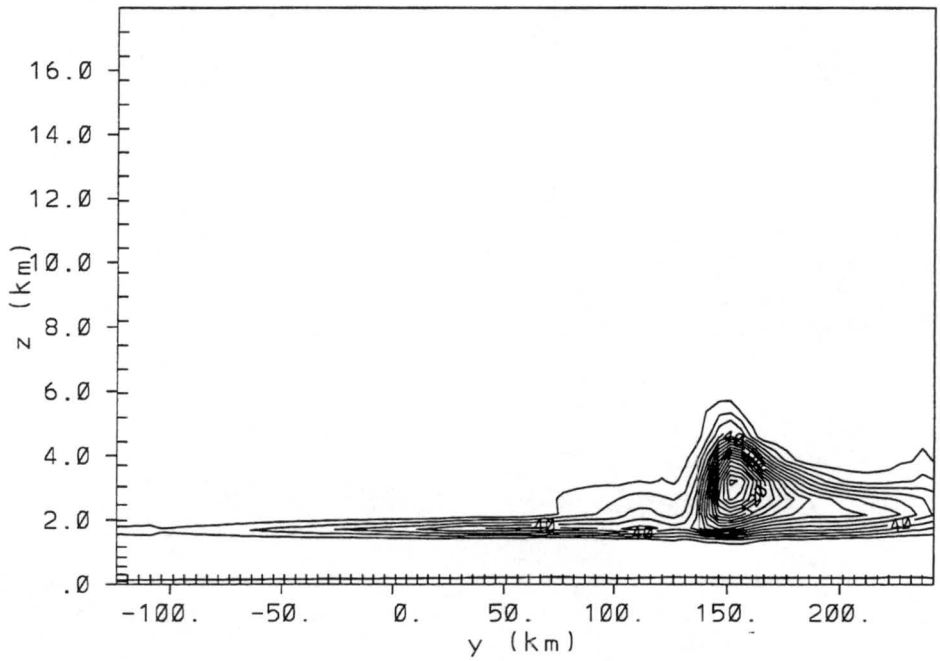

Figure 6.18: North-South cross-section (looking west) of cloud water mixing ratio at X=967.5 km in Grid 3. The maximum value diagnosed is 1.9 g/kg with a contour interval of 0.1 g/kg. The labels are multiplied by 0.1E+6 so a label of 40 corresponds to 0.4 g/kg.

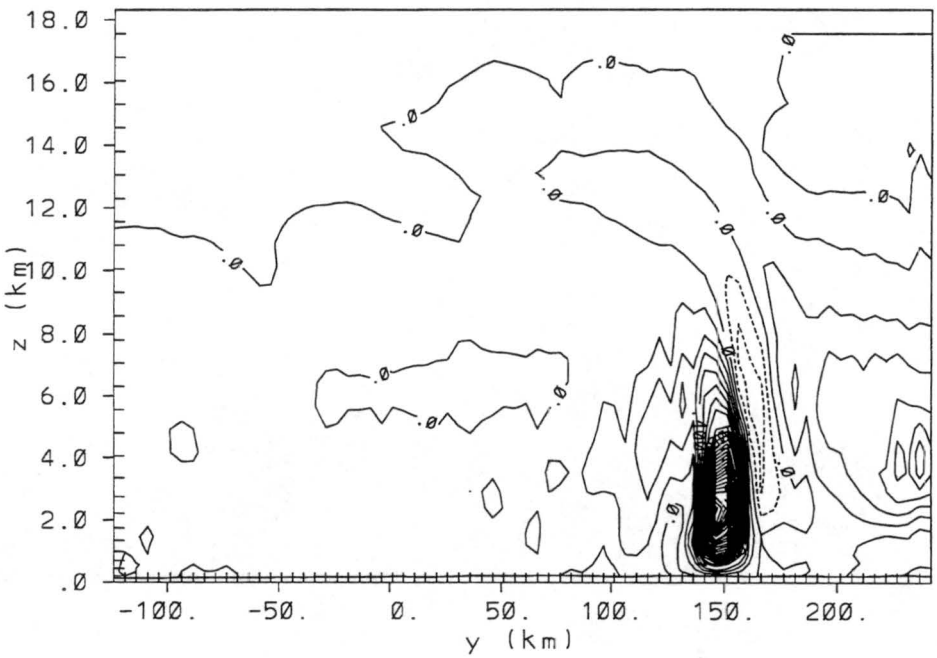

Figure 6.19: North-South cross-section (looking west) of vertical velocity, w, at X=967.5 km in Grid 3. The maximum value predicted is 3.2 m/s with a contour interval of 0.2 m/s.

of the aircraft, the aircraft angle of attack, and the meteorological conditions can affect the collection efficiency, as well as the type of ice that accumulates.

Rime ice, as discussed previously, is formed by instantaneous freezing and trapping of tiny air pockets. Clear ice, on the other hand, forms by smearing of water droplets not freezing instantaneously (see complete discussion in Chapter 2). Since in the making of clear ice, the liquid is allowed to flow somewhat before freezing, the airstream around the fuselage could help to blow off some of the water before freezing, resulting in a reduced collection efficiency. However, the larger droplets usually associated with clear ice also are more likely to cross streamlines to impact the fuselage, somewhat offsetting the effect of loss due to runback. Rime ice, on the other hand, could be said to have a higher collection efficiency due to the instantaneous freezing of droplets, negating any loss due to runback, but the fact that the droplets are usually smaller mean they are less likely to impact the fuselage, instead tending to flow around the fuselage surfaces, reducing the collection efficiency. This obviously results in a very complicated situation in which it is extremely difficult to accurately predict such accumulations, nevertheless, an attempt will be made to estimate such an accumulation.

The meteorological conditions predicted by the model and the relatively slow airspeed of about 200 kts would have likely favored the formation of clear ice, primarily due to the relatively warm, but still sub-freezing temperatures encountered at the flight level, combined with an environment conducive to forming large droplets. Given then, the density of clear ice to be approximately ρ=0.9 g/cm^3, the potential accumulation of ice was calculated to be about 4.34 cm. This obviously, is a maximum value, based on the liquid water content present. However, the actual icing, if encountered, was likely much less than this amount. However, it does not require a substantial accumulation of ice to seriously disrupt the airflow around the wing surfaces such that lift is lost and drag is increased. The accumulation of ice was probably minimal, if any was encountered at all, while flying through the convective region crossing the warm frontal boundary where there was a relatively warm pocket aloft. The area to the north and west of this convective region (over Roselawn, Indiana) is where the holding pattern was located, which, while containing less cloud water, was colder allowing for a much stronger possibility of icing. If, in fact, the aircraft crash

was caused by a hazardous accumulation of ice, the area near the holding pattern is where most of the accumulation of ice took place.

In addition to the above described method of accumulating all SLW encountered along the entire route of flight (which will be called method 'a'), attempts at calculating the potential accumulation were done for the following method: b) Accumulation of all cloud water (all droplet sizes) encountered to the north and west of the convective region only (the latter portion of the flight path) where the air temperatures at flight level were colder, c) Accumulation of just the SLW contained in droplets greater than 30 μm over the entire route of flight, and d) Accumulation of SLW in droplets greater than 30 μm only and in the latter portion of the flight path. The values in Column 1 and Column 4 of Table A.1 were multiplied by the density of air at p=700mb ($\rho_a \cong 0.9 kg/m^3$) and then converted to units of g_{H_2O}/cm^3_{air}. So, for example in the row on Table A.1 corresponding to r_c=1.0 g/kg, the value in column 1 would be converted to 9.0E-7 g/cm^3, while the value in column 4 would be converted to 5.94 E-7 g/cm^3. These values were computed for each value of r_c (not shown on tables) and were multiplied by the path length of flight that each amount of SLW was encountered so that the entire flight path (for methods a and c above) or just the latter portion of the flight path (for methods b and d above) were covered. This multiplication and then summing over the length of the flight path resulted in units of g_{H_2O}/cm^2 or g_{H_2O} per unit cross-sectional area. The final step in computing potential accumulation is to select the appropriate type of ice given the ambient meteorological conditions; in this case clear ice seemed to be most likely so dividing the above value of accumulated liquid water by the density of clear ice then yields the thickness of ice accumulated in centimeters. The values of potential accumulation of water which then resulted were as follows: Method a) 3.91g/cm^2 (liquid) or 4.34 cm of ice, b) 2.75 g/cm^2 (liquid) or 3.05 cm of ice, c) 2.03g/cm^2 (liquid) or 2.26 cm of ice, and d) 1.47g/cm^2 (liquid) or 1.63 cm of ice. Another useful comparison that will aid in comparing this basic run to the sensitivity runs will be to compute the ratio of accumulation from droplets greater than 30 μm to the accumulation from all droplet sizes, which will just be called $\frac{acc_{30}}{acc_{total}}$. This value can be calculated merely by dividing the accumulation in method c by the accumulation in method a (for the entire flight path) which yielded a percentage of $\frac{acc_{30}}{acc_{total}} = \frac{3.05\text{cm}}{4.34\text{cm}}$=53.0%. The

other value calculated from using the accumulation from the latter portion of the flight path turned out to be $\frac{acc_{3c}}{acc_{total}} = \frac{1.47\text{cm}}{2.75\text{cm}}$=51.2%. The interpretation of this ratio is that averaged over the entire flight path (or even just the latter portion of it), a little over half of the total water is contained in the 'large' droplets which are known to cause the most hazardous icing conditions.

The Chapter 7 results will contain some of the same figures, calculations of potential accumulation, and discussion as this basic run, except that it will apply to the sensitivity runs. There is also a summary table (Table 7.1) of the potential accumulation from each of the sensitivity runs performed compared to the basic run.

Chapter 7

SENSITIVITY STUDIES

So far, the model has done a reasonably good job in the prediction of the features of the mid-latitude cyclone on 31 October 1994, at least in the overall structure of the storm. As was noted in Chapter 6, there was difficulty with the overall precipitation type and amount (too little overall precipitation but too much hail), due to coding errors discussed in Chapter 6. This is primarily a low-level problem, and the cloud water aloft should not be affected much (Walko, personal communication). Despite these difficulties, meaningful information can still be gained from reviewing the sensitivity studies performed and which will be shown in this section. To summarize briefly, the following sensitivity studies were performed in which all can be compared and contrasted to the basic run described in Chapter 6: a) An option available in this version of RAMS is to specify the droplet size distribution parameter ν to a value of 3, instead of the default value of 1 (the default value of one results in a Marshall-Palmer type distribution), b) Since there was difficulty with excessive hail yet little rainfall, a simulation was performed in which the hail species was prohibited, and c) The activated CCN concentration was varied and run at values of 150, 300 (the default value, see Chapter 6), 500, 750, and 1000/cm^3. The first two sets of simulations were run with the default value of activated CCN (300/cm^3) while varying only their respective parameter, and the third set of simulations ran with hail allowed and $\nu = 1$, also the default values, so all simulations can be compared to the basic run as there was only one difference between each of the sensitivity runs and the basic run.

All of the figures in this chapter will be shown at the time of the crash, which occurred just before 2200 UTC 31 October 1994. Many of the figures, such as total precipitation were very similar to that of the basic run, and for that reason, only figures with substantial differences from their counterparts in Chapter 6 will be shown. First, the figures containing

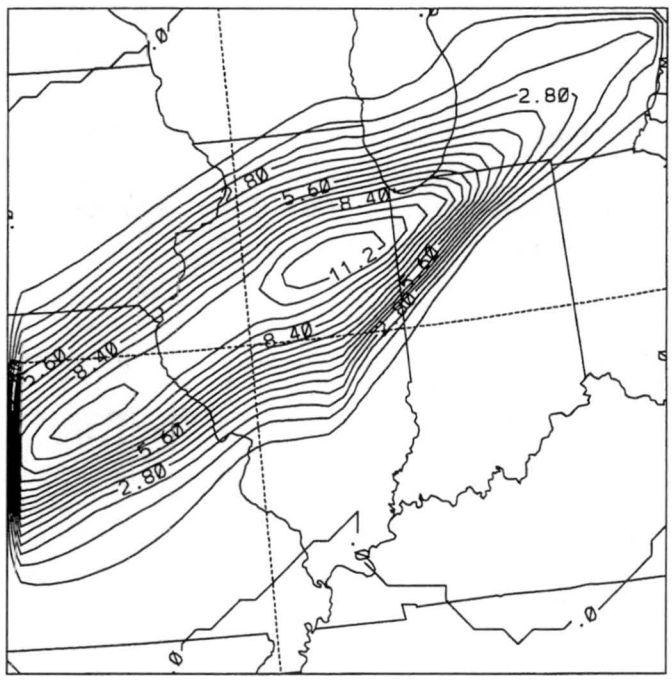

Figure 7.1: The total accumulated precipitation (all categories) at 2200 UTC 31 October in Grid 2. The maximum value of accumulated precipitation is 11.2 mm with a contour interval of 0.7 mm.

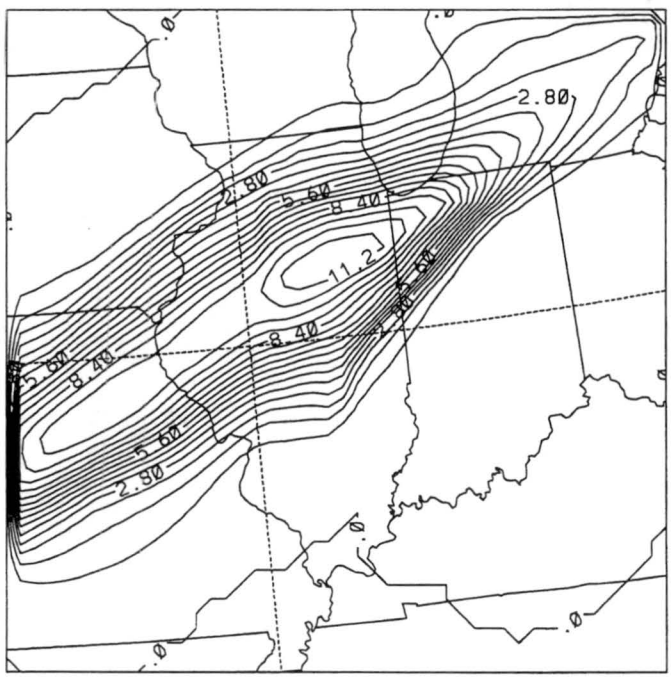

Figure 7.2: The accumulated precipitation from hail at 2200 UTC 31 October in Grid 2. The maximum value of accumulated hail is 11.2 mm with a contour interval of 0.7 mm.

the total precipitation and total accumulated hail from the basic run (Figs. 7.1 and 7.2, respectively) are shown for 2200 UTC. The 2200 UTC accumulated rainfall was not substantially different from the 2100 UTC (Fig. 6.6), and thus is not shown. The maximum value of accumulated precipitation at this time was 11.2 mm.

7.1 Sensitivity to Gamma Distribution Shape Parameter

This particular version of RAMS allows for the specification of the gamma distribution shape parameter ν to be either 1 (the default value), or 3 by a relatively minor model code change. Later versions of RAMS allow for an even greater latitude in selecting ν. The shape of the distribution is controlled by ν, and both ν and D_m control how broad the distribution is. This also forces the mode of the distribution to a value greater than zero, unlike in the Marshall-Palmer distribution where the largest number of droplets are contained in the smallest possible sizes (Walko *et al.*, 1993). An example of a droplet size distribution for the case of ν=1 and ν=3 is shown in Figure 7.3, for the same values of r_c and N_t. The mode of the distribution for ν=3 is seen to be at approximately D=13 μm, whereas for ν=1, the value of number concentration decreases exponentially away from D=0 μm.

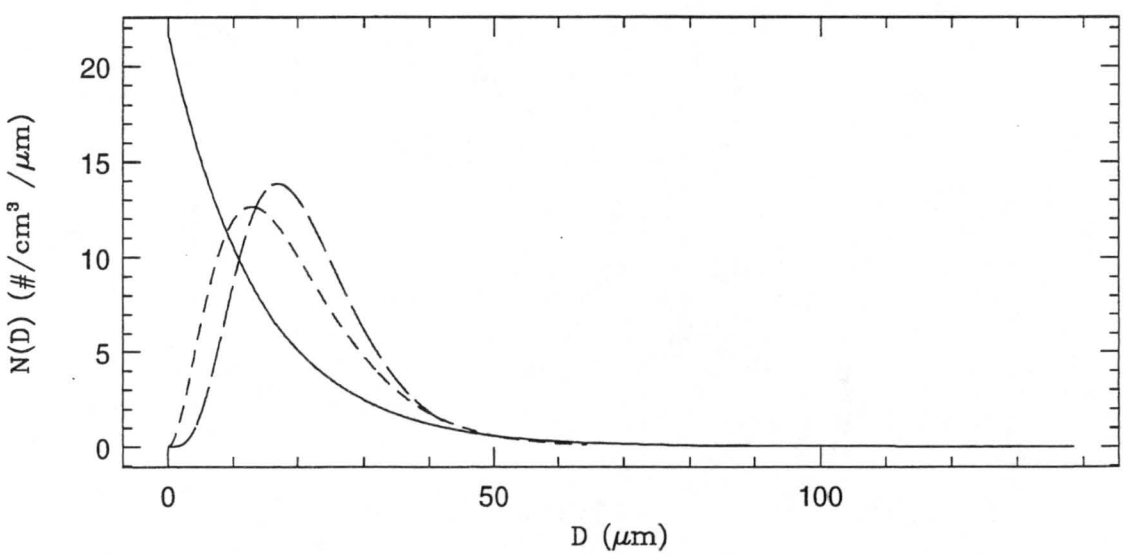

Figure 7.3: Droplet size distribution for ν=1 (solid line), ν=3 (short dashed line), and ν=5 (long dashed line) with N_t=300/cm^3 and cloud water mixing ratio = 2.5 g/kg for each. The number on the vertical axis corresponds to the number concentration of droplets in a 1 μm wide bin centered on a particular value of droplet diameter D.

Unfortunately, there doesn't seem to be very good guidance about which type of distribution to expect for a particular cloud type (regarding specific values of ν, that is). In general though, broader droplet distributions correspond to clouds which perhaps are more turbulent in nature or are entraining parcels of dry air such as cumuliform clouds. Also, in this case strongly sheared and turbulent stratiform clouds that are undergoing some sort of active droplet broadening process can these broader droplet distributions be seen. Narrower distributions probably are then better correlated to less turbulent or stratiform clouds, or even cumulus cloud parcels that are relatively unmixed (Cotton and Anthes, 1989).

The first apparent difference in this sensitivity run of ν=3, is that the precipitation totals, at least in the rainfall category, were higher than the basic run (Fig. 7.4), consistant with a broader distribution. Although there was only 2.7 mm of rainfall, this is over 6 times the value of 0.42 mm predicted by the basic run. Unfortunately, the amount is still way to small compared to the observations and the total accumulated precipitation (Fig. 7.5) is little changed from the basic run with a maximum value of precipitation predicted to be 10.2 mm. The only affect here then, appeared to be that slightly more of the total precipitation fell into the rain category. Again, this is the same problem involving RAMS microphysics as what addressed back in Chapter 6.

Many of the other features (overall dynamic structure) of the storm were nearly identical to the basic run, so only the cloud water and mass mean diameter figures will be shown for this case, in addition to the just mentioned precipitation figures. Figure 7.6 shows the cloud water mixing ratios for this case, and the only real difference between this and Figure 6.11 is that the maximum value of r_c diagnosed is 1.8 g/kg, slightly less than the 2.0 g/kg found in the basic run. This slight decrease could be the result of more precipitation occurring in the rainfall category, although as mentioned, the overall precipitation totals were about the same as the basic run.

The interesting information is instead gained from the knowledge of the mass mean diameter and potential accumulation calculated from this case. Figure 7.7 shows the diagnosed values of D_m and the maximum D_m diagnosed was 32 μm, substantially less than the 46 μm diagnosed in the basic run (Fig. 6.14). This is not surprising, given the differences in the droplet size distribution between ν=1 and ν=3 (Fig. 7.3). A narrower distribution

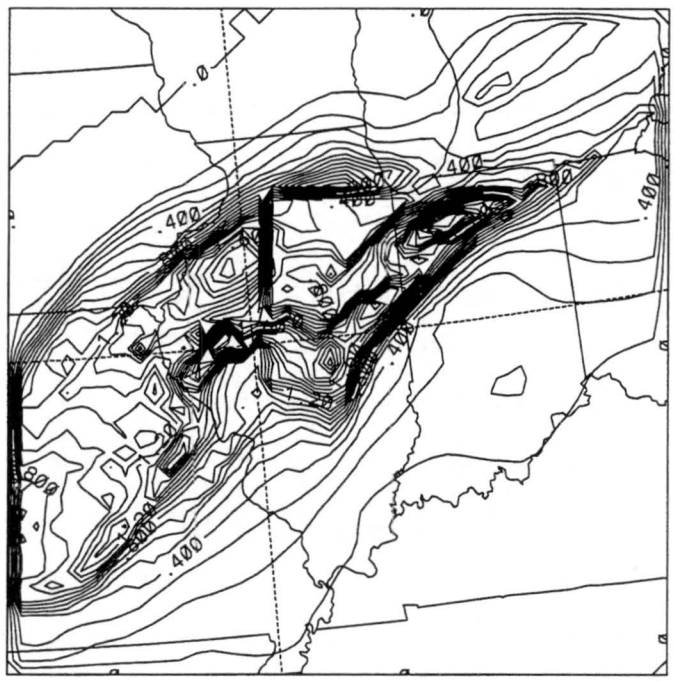

Figure 7.4: The Accumulated Rain at 2200 UTC 31 October 1994 in Grid 2 with ν=3. The maximum rainfall predicted is 2.7 mm with a contour interval of 0.1 mm.

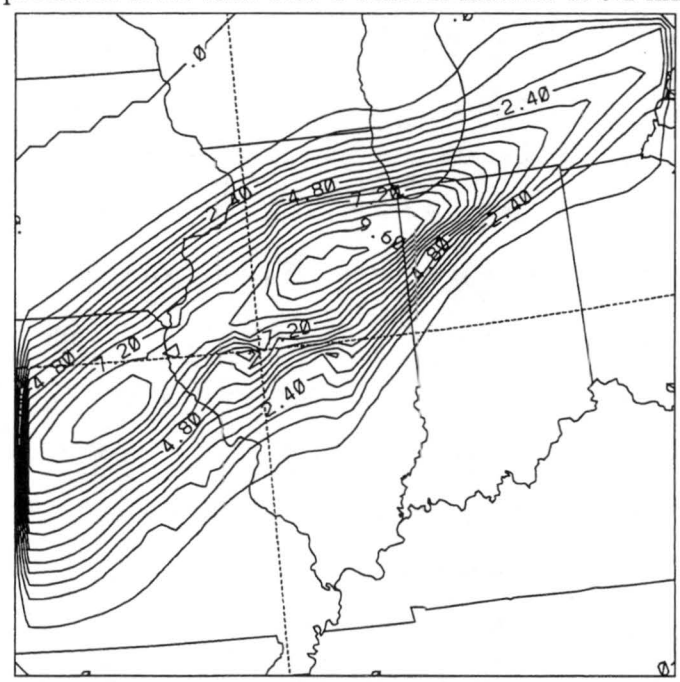

Figure 7.5: The total accumulated precipitation at 2200 UTC 31 October 1994 in Grid 2 with ν=3. The maximum value predicted is 10.2 mm with a contour interval of 0.6 mm.

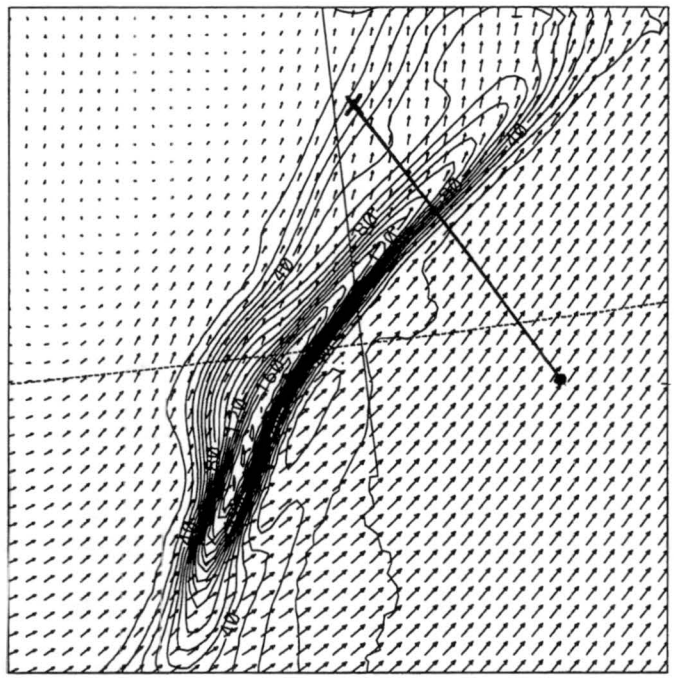

Figure 7.6: The cloud water mixing ratio in units of g/kg analyzed at p=700mb and ν=3 in Grid 3. The maximum value of cloud water mixing ratio diagnosed is 1.8 g/kg, with a contour interval of 0.1 g/kg. The labels are multiplied by 0.1E+6 so a label of 80 corresponds to a value of 0.8 g/kg. The arrows are horizontal wind vectors and a vector having a length equal to the distance between the tails of any two vectors has a magnitude of 25.1 m/s.

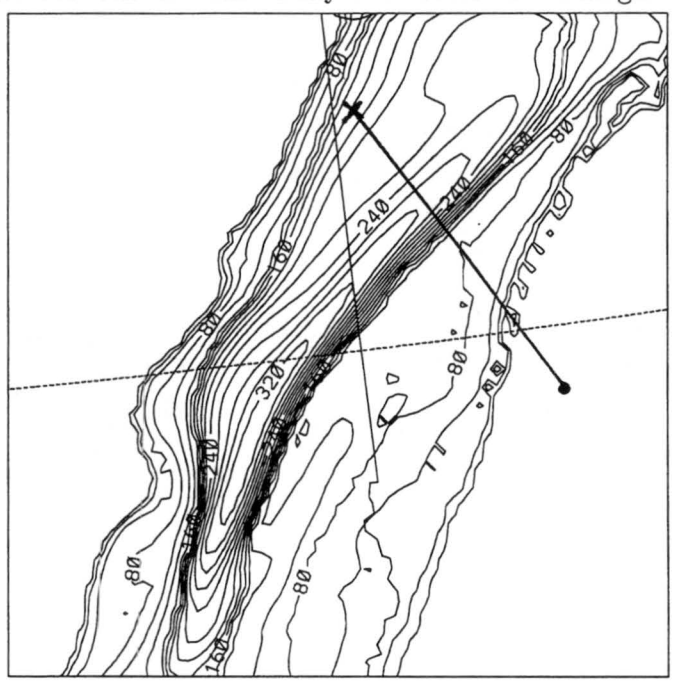

Figure 7.7: The mass mean diameter of cloud water droplets in units of μm at p=700mb and ν=3 in Grid 3. The maximum mass mean diameter diagnosed is 32 μm with a contour interval of 2 μm. The labels are multiplied by 0.1E+8 so a label of 240 corresponds to 24 μm.

such as this would be expected to have D_m closer to the mode of the distribution than the basic run.

The calculation for potential accumulation was performed exactly as described in Section 6.3 for the basic run. This time, however, Table A.6 in the appendix was used for its corresponding values of r_c contained in droplets greater than 30 μm. Using these numbers, the potential accumulation calculations turned out as followed (again, see Section 6.3 for description of methods); method a) 4.45g/cm^2 (liquid) or 4.94 cm of ice, b) 3.40 g/cm^2 (liquid) or 3.77 cm of ice, c) 1.00g/cm^2 (liquid) or 1.11 cm of ice, and d) 0.82g/cm^2 (liquid) or 0.92 cm of ice.

In a similar manner to the basic run, the ratios of $\frac{acc_{30}}{acc_{total}}$ were also found to be $\frac{1.11\text{cm}}{4.94\text{cm}}$=24.0% for the entire flight path and $\frac{0.92\text{cm}}{3.77\text{cm}}$=23.0% for the latter portion of the flight path. These much lower percentages are to be expected in the narrower distribution characterized by ν=3, i.e. less than one quarter of the total cloud water was contained in the 'large' droplets.

7.2 Sensitivity to No-Hail

The next test case, based on the problem of precipitation type produced by RAMS, was to prohibit the formation of hail as a hydrometeor species, which is easily done by modifying the RAMS namelist. The primary result of this experiment, unfortunately, was to further reduce the overall precipitation total. However, the rainfall amounts were increased and proved to be the best of any of the model runs performed with a maximum value of 6.0 mm as of 2200 UTC (Fig. 7.8). There was little additional precipitation from other species, and as a consequence the overall precipitation total was lowest among all the simulations performed.

A result of the reduced precipitation, then, was to keep the overall water content of the atmosphere higher, and as it turned out, the cloud water content was highest in this case compared to the rest. This can be easily seen in Figure 7.9 of 700mb relative humidity, where the area covered by 100% RH is considerably larger than its counterpart figure from the basic run, Figure 6.10, at least in the northward and westward extent of this saturated region. Further evidence of the higher cloud water becomes more obvious in the cloud water

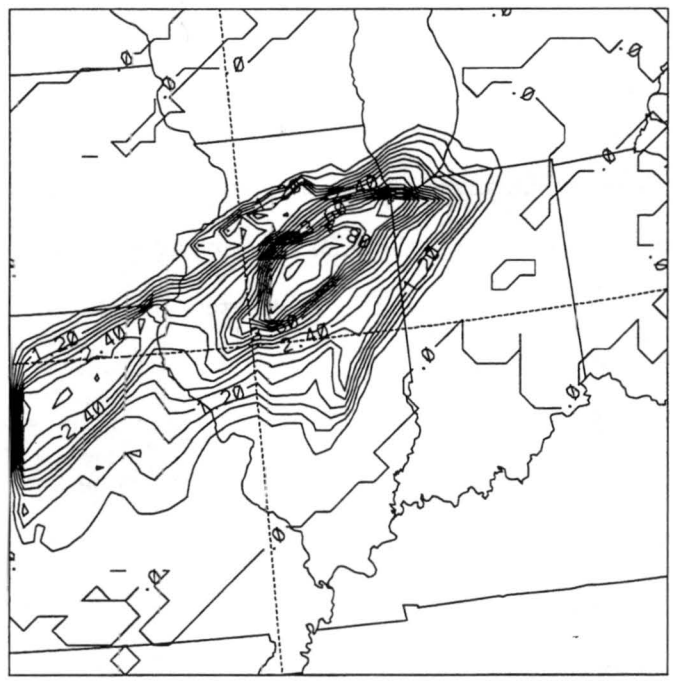

Figure 7.8: The Total Accumulated Precipitation at 2200 UTC 31 October 1994 in Grid 2 with no hail. The maximum value predicted is 6.0 mm with a contour interval of 0.3 mm. Since hail was prohibited in this case, most of this precipitation is in the form of rain.

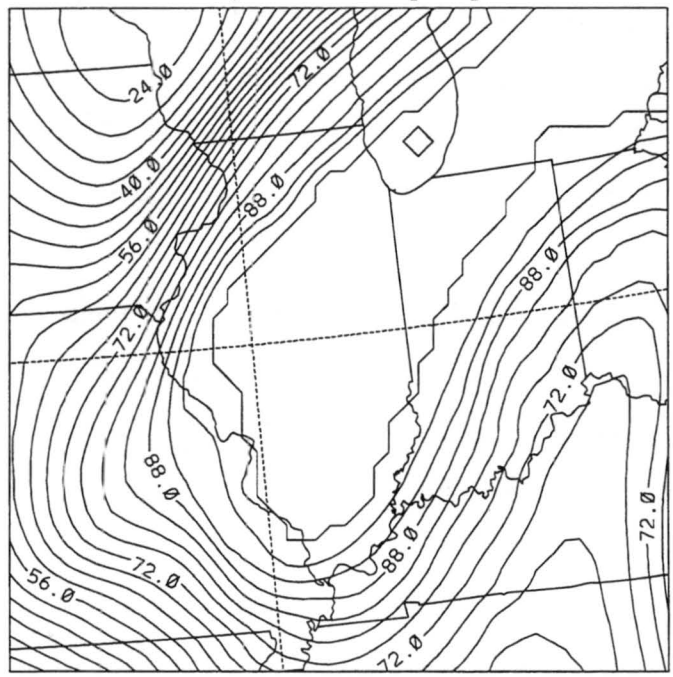

Figure 7.9: The percent relative humidity (RH) analyzed at p=700mb in Grid 2 with no hail. The maximum value of RH diagnosed is 100, with a contour interval of 4.

plot for this simulation (Fig. 7.10). The maximum value diagnosed here is 2.5 g/kg, not that much larger than the other simulations, however the areal extent of the region bounded by the 2.0 g/kg or even the 1.0 g/kg contours, for example, is considerably larger than in any of the other simulations. The route of flight crossed through regions where the SLW was considerably higher than any of the other simulations; it would have flown through two maxima of r_c greater than 2.4 g/kg, one of them being very near the holding pattern of the doomed aircraft. The plot of mass mean diameters (Fig. 7.11) also shows exceptionally large values as a result of the high values of r_c diagnosed. Much of the area covering the route of flight in this figure can be seen to have mass mean diameter over 48 μm, again, the largest (at least in areal coverage) of any of the simulations performed.

The results of the potential accumulation from this no-hail case were as follows (using the same table (A.1) and method described in Section 6.3 as the basic run given that the distribution parameters were the same); method a) 20.33 g/cm^2 (liquid) or 22.59 cm of ice, b) 13.32 g/cm^2 (liquid) or 14.80 cm of ice, c) 14.39 g/cm^2 (liquid) or 16.00 cm of ice, and d) 10.67 g/cm^2 (liquid) or 11.86 cm of ice. The ratio of $\frac{acc_{30}}{acc_{total}}$ in these cases turned out to be $\frac{16.00\text{cm}}{22.59\text{cm}}$=70.1% for the entire route of flight, or $\frac{11.86\text{cm}}{14.80\text{cm}}$=80.1% for just the latter portion. These exceptionally high percentages result from such high SLW compared to the other simulations, and given that much of the area contains droplets much larger than 30μm, it should not be surprising that most of the mass of cloud water (70-80%) is contained in the large droplets.

Due to these extremely high values of potential accumulation and SLW, as well as the aircraft investigation not revealing that the pilots were reporting that severe of icing (Politovich, personal communication), it is highly unlikely that this simulation represented the conditions encountered by the doomed aircraft over Indiana. The high LWC compared to the other simulations is therefore a result of prohibiting one of the precipitation species. This simulation was not completely without value, as it demonstrates how the icing potential (by the 'large' droplets) of a storm can be significantly enhanced by just a modest increase of cloud water. In this case, doubling the cloud water content from say 1.0 g/kg to 2.0 g/kg more than doubled the amount of possible ice accumulation by large droplets, and it was probably closer to 2 1/2 times greater based on the values in Table A.1.

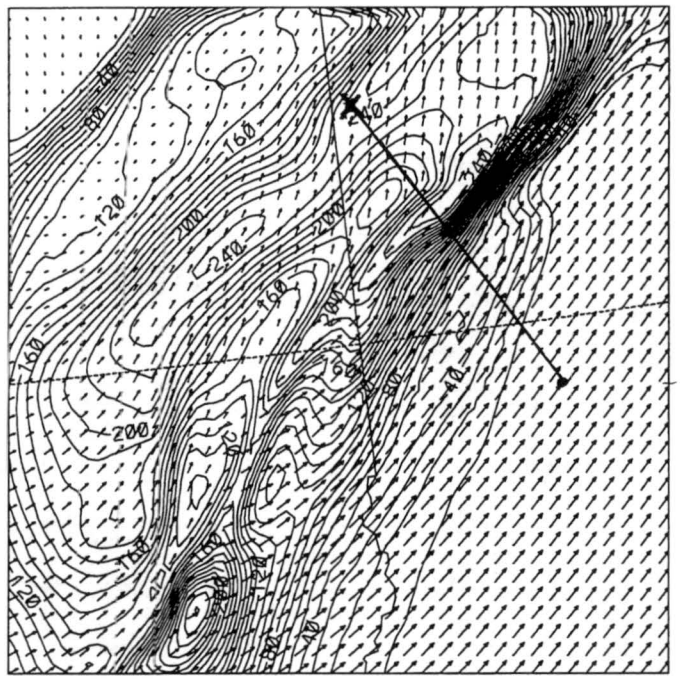

Figure 7.10: The cloud water mixing ratio in units of g/kg analyzed at p=700mb in Grid 3 with no hail permitted. The maximum value of cloud water mixing ratio diagnosed is 2.5 g/kg, with a contour interval of 0.1 g/kg. The labels are multiplied by 0.1E+6 so a label of 80 corresponds to a value of 0.8 g/kg. The arrows are horizontal wind vectors and a vector having a length equal to the distance between the tails of any two vectors has a magnitude of 24.7 m/s.

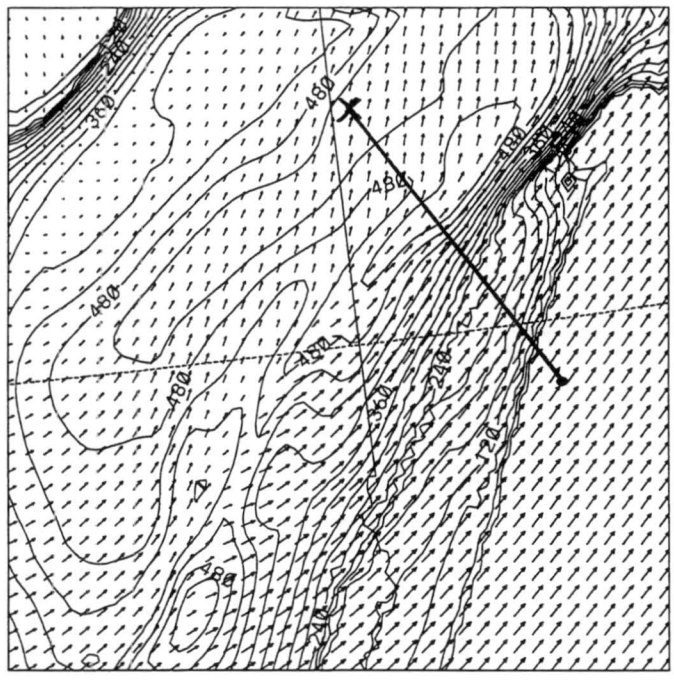

Figure 7.11: The mass mean diameter of cloud water droplets in units of μm at p=700mb in Grid 3 with no hail permitted. The maximum mass mean diameter diagnosed is 51 μm with a contour interval of 3 μm. The labels are multiplied by 0.1E+8 so a label of 240 corresponds to 24 μm.

7.3 Sensitivity to Activated CCN Concentration

The last several sensitivity runs and the bulk of the simulations performed, involved varying the ever-important activated CCN concentration, N_t. For these simulations, four sets of values were used to perform these studies; N_t=150, 500, 750, and 1000/cm^3. The low numbers represent relatively clean air, i.e. that which is probably more of a maritime origin and not that likely over continental regions except in rare cases. The increasing values of N_t represent increasingly 'dirty' air, either from natural sources of dust, pollen, and other particles or perhaps anthropongenic sources of pollutants such as automobile emissions and industrial processes. In order to see what the different types of distributions look like, one need only examine Fig. 7.12 in order to compare how the distributions of each of the sensitivity runs and the basic run differ from each other. As can be easily seen for distribution of the same total mixing ratio r_c, there is a wide range in number concentration in the smallest size bins (near D=0 μm).

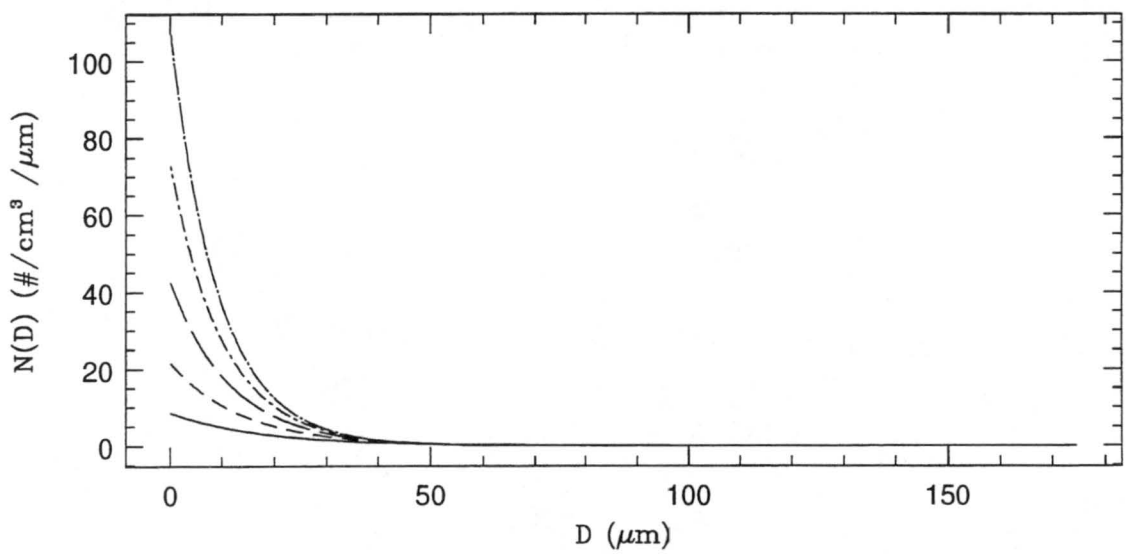

Figure 7.12: Droplet size distributions for N_t= 150, 300, 500, 750, and 1000/cm^3 (with ν=1 and r_c = 2.5 g/kg for each). The number on the vertical axis corresponds to the number concentration of droplets in a 1 μm wide bin centered on a particular value of droplet diameter D. The highest peak at D = 0 μm corresponds to the highest value of N_t (1000/cm^3) whereas the lowest peak at D = 0 μm corresponds to the smallest value of N_t (150/cm^3), with the rest in their respective order of N_t.

A well known trend is that, in general, for a given amount of cloud water, a larger number of droplets competing for the same amount of cloud water in one case versus another will result in smaller overall sizes for the distribution containing more droplets, or activated CCN. This also works the other way; for the clean maritime air masses where there are relatively few droplets competing for a like amount of cloud water, the droplets tend to be much larger.

Before the remainder of the results are shown, it should be pointed out that there were only slight differences in the precipitation totals among these runs, and those were only in the rainfall category and were not very evident in the overall precipitation totals, hence they will not be shown here. In general, there was a slight increase in the rainfall category for the case of $N_t = 150/\text{cm}^3$, but by only fractions of millimeters whereas the higher values of N_t resulted in a slight decrease of rainfall compared to the basic run, but again only fractions of millimeters. The near-surface rainfall mixing ratio maxima (also not shown) for this region decreased from a value of 0.46E-5 kg/kg for $N_t = 150/\text{cm}^3$ down to 0.40E-5 kg/kg for $N_t = 1000/\text{cm}^3$ This trend appears to be correct, although the magnitude of the effect on total precipitation should have been somewhat greater. Again, this is likely the result of the same precipitation problems in RAMS mentioned before.

The most noticeable and important differences then in the remainder of the sensitivity studies are in the cloud water mixing ratio and mass mean diameter figures. They are shown as Figures 7.13 and 7.14, respectively for $N_t = 150/\text{cm}^3$, Figs. 7.15 and 7.16, respectively, for $N_t = 500/\text{cm}^3$, Figs. 7.17 and 7.18, respectively, for $N_t = 750/\text{cm}^3$, and Figs. 7.19 and 7.20, respectively, for $N_t = 1000/\text{cm}^3$.

The cloud water mixing ratio plot for $N_t = 150/\text{cm}^3$ shows the least amount of cloud water present compared to the other remaining sensitivity runs (varying N_t). This could be the result of the slight enhancement of the precipitation (rainfall) processes which normally occur with fewer, but larger droplets. The collision-coalescence process creating precipitation sized particles is enhanced by the presence of larger droplets as is the case here. The mass mean diameter for this same case (Fig. 7.14) shows the dramatic impact on the size of the droplets when relatively few of them are present. The maximum D_m diagnosed in this case was 60 μm, the largest of any of the sensitivity runs. If this were truly the case

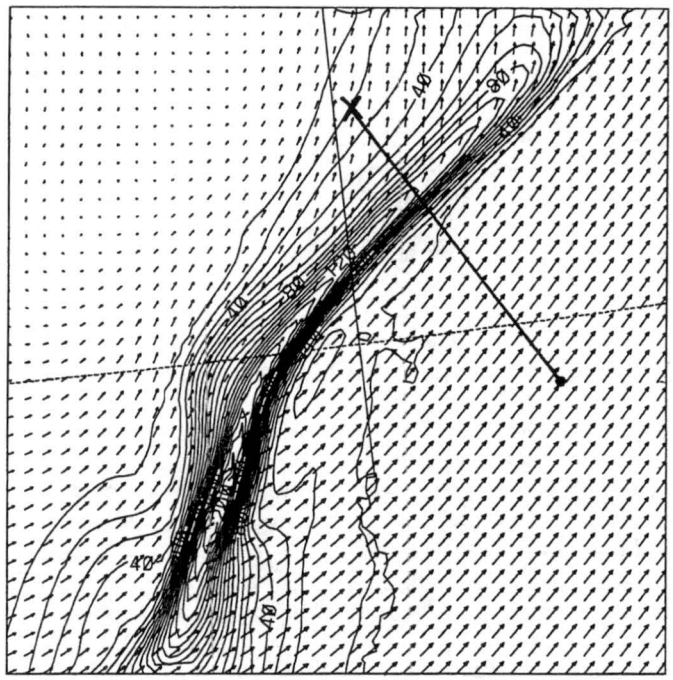

Figure 7.13: The cloud water mixing ratio in units of g/kg analyzed at p=700mb with $150/cm^3$ in Grid 3. The maximum value of cloud water mixing ratio diagnosed is 2.0 g/kg, with a contour interval of 0.1 g/kg. The labels are multiplied by 0.1E+6 so a label of 80 corresponds to a value of 0.8 g/kg. The arrows are horizontal wind vectors and a vector having equal length to the distance between the tails of any two vectors has a magnitude of 24.9 m/s.

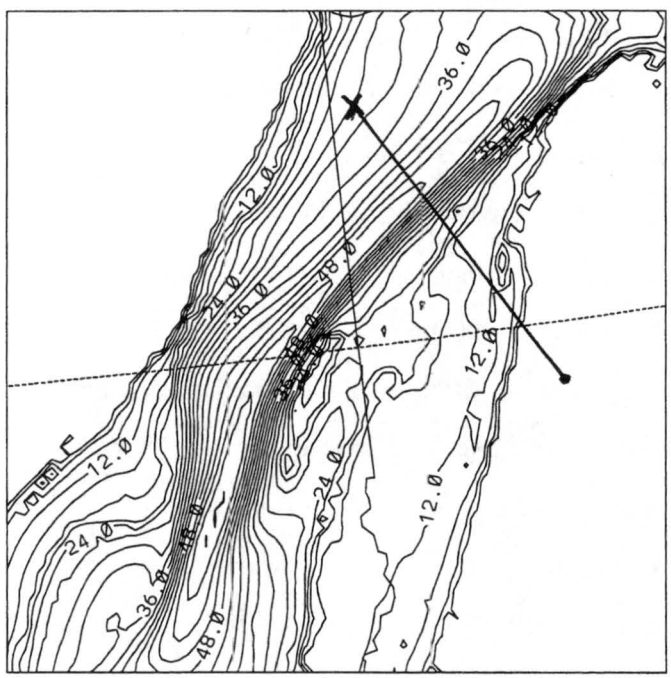

Figure 7.14: The mass mean diameter of cloud water droplets in units of μm at p=700mb with $150/cm^3$ in Grid 3. The maximum mass mean diameter diagnosed is 60 μm with a contour interval of 3 μm.

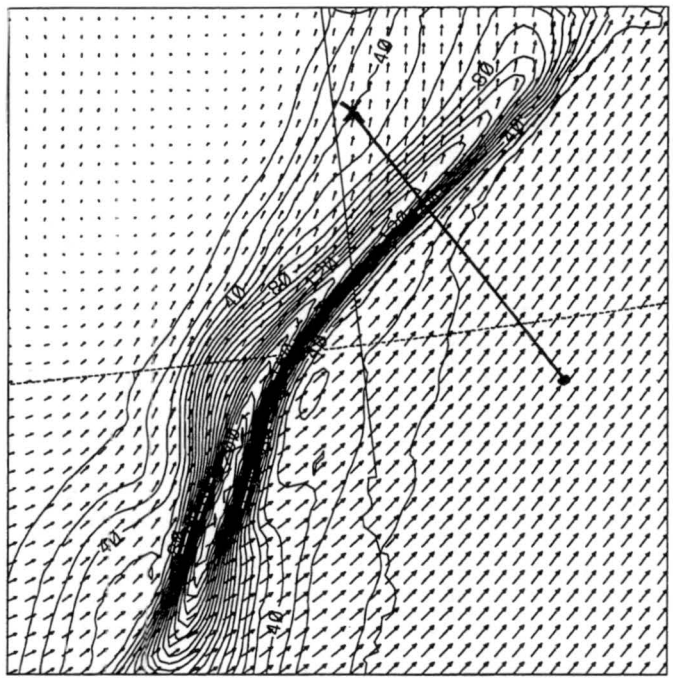

Figure 7.15: The cloud water mixing ratio in units of g/kg analyzed at p=700mb with $500/cm^3$ in Grid 3. The maximum value of cloud water mixing ratio diagnosed is 2.3 g/kg, with a contour interval of 0.1 g/kg. The labels are multiplied by 0.1E+6 so a label of 80 corresponds to a value of 0.8 g/kg. The The arrows are horizontal wind vectors and a vector having equal length to the distance between the tails of any two vectors has a magnitude of 24.9 m/s.

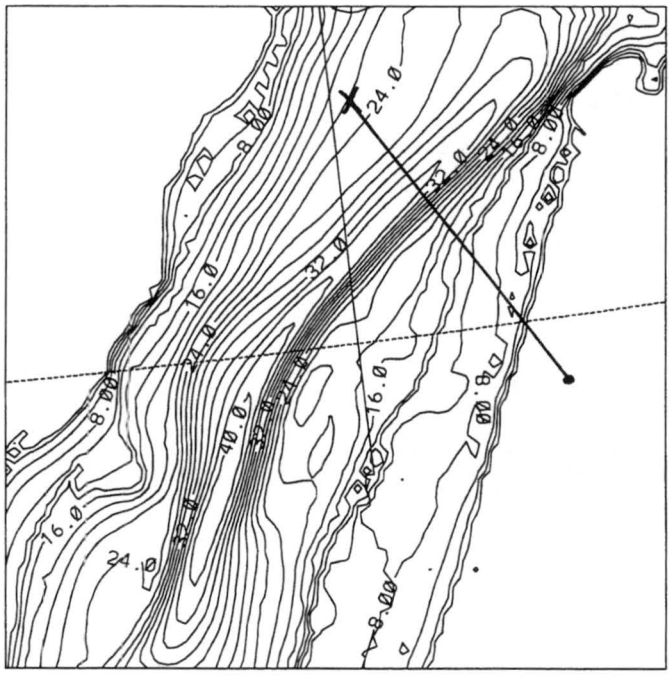

Figure 7.16: The mass mean diameter of cloud water droplets in units of μm at p=700mb with $500/cm^3$ in Grid 3. The maximum mass mean diameter diagnosed is 40 μm with a contour interval of 2 μm.

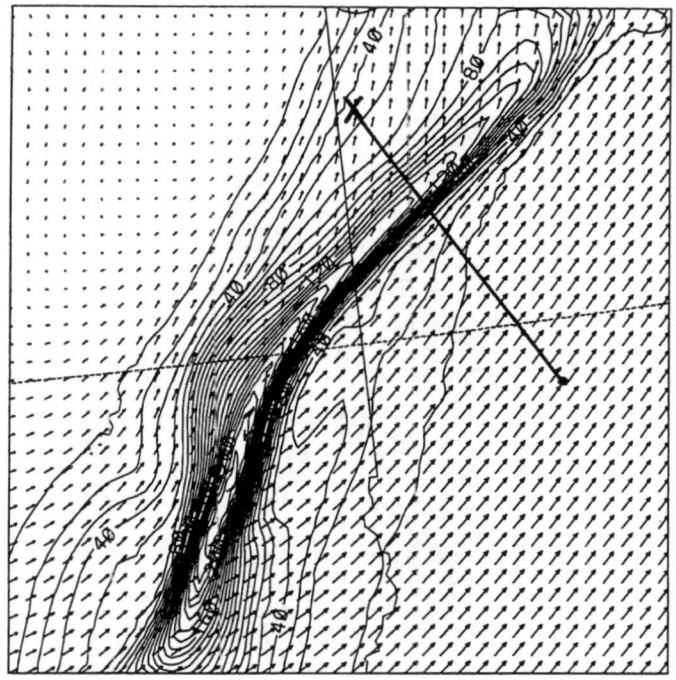

Figure 7.17: The cloud water mixing ratio in units of g/kg analyzed at p=700mb with 750/cm^3 in Grid 3. The maximum value of cloud water mixing ratio diagnosed is 2.4 g/kg, with a contour interval of 0.1 g/kg. The labels are multiplied by 0.1E+6 so a label of 80 corresponds to a value of 0.8 g/kg. The The arrows are horizontal wind vectors and a vector having equal length to the distance between the tails of any two vectors has a magnitude of 24.9 m/s.

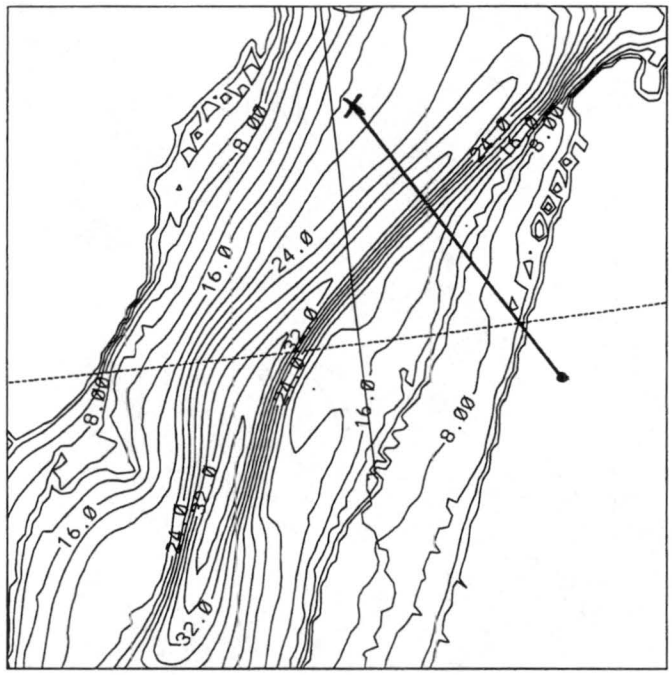

Figure 7.18: The mass mean diameter of cloud water droplets in units of μm at p=700mb with 750/cm^3 in Grid 3. The maximum mass mean diameter diagnosed is 36 μm with a contour interval of 2 μm.

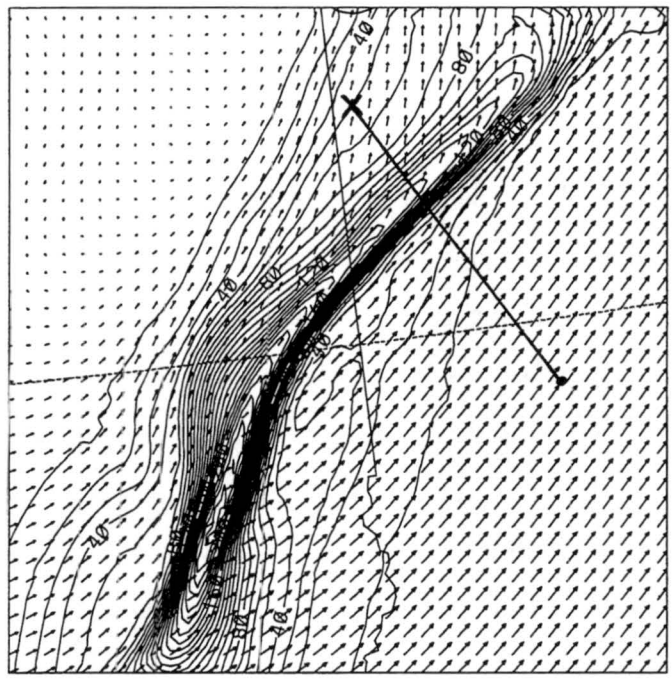

Figure 7.19: The cloud water mixing ratio in units of g/kg analyzed at p=700mb with $1000/cm^3$ in Grid 3. The maximum value of cloud water mixing ratio diagnosed is 2.4 g/kg, with a contour interval of 0.1 g/kg. The labels are multiplied by 0.1E+6 so a label of 80 corresponds to a value of 0.8 g/kg. The The arrows are horizontal wind vectors and a vector having equal length to the distance between the tails of any two vectors has a magnitude of 24.9 m/s.

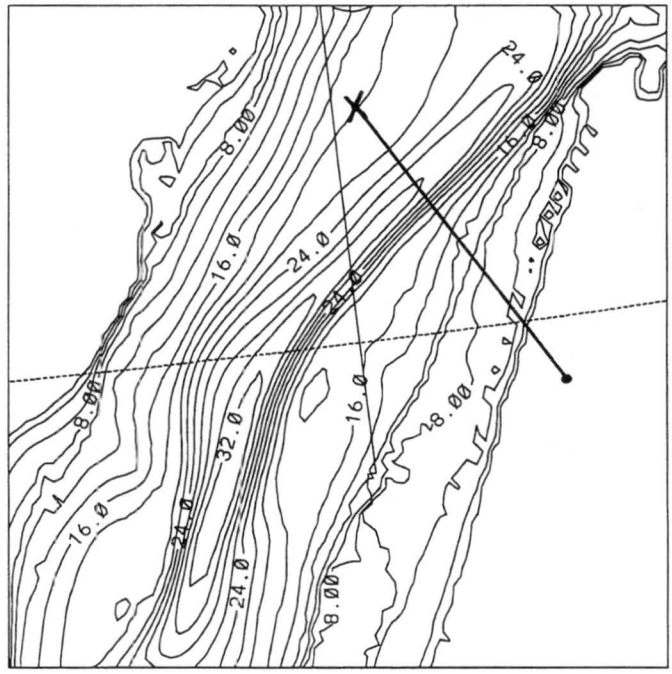

Figure 7.20: The mass mean diameter of cloud water droplets in units of μm at p=700mb with $1000/cm^3$ in Grid 3. The maximum mass mean diameter diagnosed is 32 μm with a contour interval of 3 μm.

on this day, such a large D_m for the mixing ratio r_c would no doubt have resulted in severe icing, perhaps not as severe as the no-hail case, but the strongest of any of these sensitivity runs in which N_t is varied.

Using Table A.2 in this case to perform potential accumulation calculations, the following accumulations were obtained (again, see complete description of the methods in Section 6.3); Method a) 3.80 g/cm^2 (liquid) or 4.22 cm of ice, b) 2.37 g/cm^2 (liquid) or 2.63 cm of ice, c) 2.57 g/cm^2 (liquid) or 2.86 cm of ice, and d) 1.58 g/cm^2 (liquid) or 1.76 cm of ice. The ratio of $\frac{acc_{30}}{acc_{total}}$ for these cases was $\frac{2.86\text{cm}}{4.22\text{cm}}$=68.0% for the entire flight path and $\frac{1.75\text{cm}}{2.63\text{cm}}$=67.0% for the latter portion of the flight path. These results show that given the relatively small number of droplets present, about two-thirds of them are forced to be in sizes larger than 30 μm, when averaged over the flight path through this simulated cloud water field. This will not be the case as N_t increases, these percentages will be shown to decrease as more and more droplets compete for a like amount of total cloud water.

The remaining sensitivity studies are therefore an attempt to compute icing potential based on N_t concentration more likely to be found in interior continental regions such as the midwestern United States, and especially downwind of major urban and industrial areas such as Chicago, IL, and Gary, IN. The overall trend that should be taken away from the remaining figures (Figs. 7.15 through 7.20) is that as N_t increases, so does the cloud water amount (but up to a limit) as precipitation processes become slightly less efficient with the more, but smaller droplets. The maxima of cloud water diagnosed from the N_t=500, 750, and 1000/cm^3 is 2.3, 2.4, and 2.4 g/kg, respectively. This can be compared to the maxima of 2.0 g/kg for N_t=150/cm^3. The evidence of smaller droplets can be seen in the mass mean diameter plots for these same runs; the maximum value of D_m=40 μm occurs with N_t=500/cm^3 and decreases to maximum value of D_m=32 μm for N_t=1000/cm^3.

The results of potential accumulation calculations for the rest of these simulations are shown here in Table 7.1, having used Tables A.3, A.4, and A.5 in the appendix for the cases of N_t=500, 750, and 1000/cm^3, respectively, as was done in all the other cases so far. The important thing to take away from these calculations are two-fold. First, as N_t increases, so does the overall maximum in cloud water up to a point, which allowed for a general increase of the total possible accumulation if all cloud water were swept up. More significantly,

however, the resulting decrease in D_m also went along with a substantial decrease in the amount of cloud water contained in 'large' droplets, thus reducing the overall icing hazard as more of the water was forced into smaller droplets which have smaller collection efficiencies. In Table 7.1, the columns which represent accumulation of cloud water in droplets greater than 30 μm (Method C and D) show a substantial decrease in the amount of cloud water accumulated as N_t increases, while at the same time the potential accumulation when collecting all cloud water (Method A and B) showed increases.

Table 7.1: **Summary of Potential Accumulations from all Simulations**

Run Type	Method A	Method B	Method C	Method D	$\frac{acc_{30}}{acc_{total}}$(%)
Basic	3.91 g/cm^2	2.75 g/cm^2	2.03 g/cm^2	1.47 g/cm^2	51.2
(N_t=300/cm^3)	4.34 cm	3.05 cm	2.26 cm	1.63 cm	53.0
ν=3	4.45 g/cm^2	3.40 g/cm^2	1.00 g/cm^2	0.82 g/cm^2	24.0
	4.94 cm	3.77 cm	1.11 cm	0.92 cm	23.0
No Hail	20.33 g/cm^2	13.32 g/cm^2	14.39 g/cm^2	10.67 g/cm^2	70.1
	22.59 cm	14.80 cm	16.00 cm	11.86 cm	80.1
N_t=150/cm^3	3.80 g/cm^2	2.37 g/cm^2	2.57 g/cm^2	1.58 g/cm^2	68.0
	4.22 cm	2.63 cm	2.86 cm	1.76 cm	67.0
N_t=500/cm^3	5.56 g/cm^2	3.91 g/cm^2	2.53 g/cm^2	1.85 g/cm^2	45.5
	6.17 cm	4.34 cm	2.81 cm	2.05 cm	47.2
N_t=750/cm^3	6.17 g/cm^2	4.22 g/cm^2	2.22 g/cm^2	1.63 g/cm^2	35.7
	6.88 cm	4.68 cm	2.46 cm	1.81 cm	38.7
N_t=1000/cm^3	7.01 g/cm^2	4.64 g/cm^2	2.12 g/cm^2	1.45 g/cm^2	30.2
	7.78 cm	5.15 cm	2.35 cm	1.61 cm	31.3

Explanation of Table: **Column 1** summarizes the various simulations that were performed, whereas **Columns 2 through 5** summarize the potential accumulations from the different methods of calculations of potential accumulations performed (See Section 6.3 for complete description of these different calculation methods). The upper of the two numbers in each row is the mass of water per unit cross-sectional area accumulated for that simulation and method of calculation, whereas the lower of the two numbers represents its corresponding thickness of ice in centimeters (assuming clear ice, ρ_{ice}=0.9 g/cm^3). **Column 6** is the percentage of the accumulated water in droplets larger than 30 μm (found in methods C and D) compared to the total water encountered in all droplet sizes. The upper of these two numbers is the percentage from the entire flight path, the lower of these two is from the latter portion of the flight path.

Chapter 8

SUMMARY AND CONCLUSIONS

The original purpose of this thesis was to examine if a mesoscale model, such as RAMS, could be used to aid in identifying potentially hazardous icing regions as well as interrogating the storm to determine the necessary structure which could lead to such a hazardous event. While the crash involving the American Eagle commuter flight near Roselawn, IN, was likely caused by a combination of factors, the National Transportation Safety Board investigation report of this incident had not yet been published at the time of this writing. The investigation was being carried out based on the possibility of icing as a contributing factor, however, and the report is scheduled for release in mid-1996. The weather conditions at the time and place of the crash were such that any experienced aviation meteorologist would have been able to identify that area of Indiana as a high threat region, in a sector of the extra-tropical cyclone where icing is common (ahead and aloft of the warm front).

8.1 Summary of Results

The most fundamental requirement for aircraft icing to occur, as stated earlier, is to have sufficient quantities of condensed cloud water present while sufficiently below freezing, thus having supercooled liquid water present. The model results, while not a perfect representation of reality, did, in all simulations, show that the icing potential existed in this storm at the time of the crash and along the flight path of the doomed aircraft.

Icing potential was shown to be strongly dependent upon the droplet size distribution present inside the cloud. Distributions where there were relatively few, but consequently larger droplets were shown to be a much more serious threat as up to 80% of the cloud water mass can be contained in the 'large' droplets. On the other hand, distributions with significantly higher numbers of activated CCN present produced only slightly greater

amounts of cloud water but a much smaller D_m. In these high concentration areas, the distribution was such that around 30% of the cloud water was contained in the 'large' droplets for a cloud water mixing ratio r_c on the order of 1.0 to 2.0 g/kg. Thus, having knowledge of CCN concentrations or droplet size distributions could lead to better forecasts as one could infer how much water is contained in various bins of droplet sizes.

The values of potential accumulation of ice ranged from less than 1 cm to over 20 cm in the most extreme case, but all showed that at least some amount of ice accumulation was possible given the conditions in the model. Other parameters such as the Richardson number and vertical wind shear computed from model data in all cases favored the formation of large droplets by inferring that a strong shear layer was present at approximately the same location and elevation as the flight path.

Based on all available information analyzed from the model, it is then reasonable to conclude that mesoscale models, such as RAMS, can be used successfully to aid in identifying hazardous icing regions. All the information needed to compute the important variables for icing such as cloud water, temperature, droplet size distribution, vertical wind shear, and others are either prognosed by the mode or diagnosed as needed from the other variables. Concerns such as timeliness and grid resolution which are also important, will be addressed in the following section.

8.2 Suggestions for Future Research

As is the case with any atmospheric model, it is desirable to increase the resolution while maintaining or improving on model run times. Continuing advances in computing power and memory, as well as more efficient computer code and parameterizations will continue to improve model performance, as will increased knowledge of atmospheric processes upon which the code is based. As far as applications to the field of icing is concerned, it would be desirable to have the above mentioned higher resolution and faster running model to cover large areas of the country or even the world, and do so in real time or better such that the aviation community can be provided with more specific information when deciding on routes of flight, altitudes, or even timing. Other possibilities for the use of real-time mesoscale models would be for the forecasters identify threat areas from the large scale

features (locations of synoptic scale mid-latitude cyclones for example) and telescope the finer resolution grids to the immediate area of interest to determine how extreme the threat is, which could also support subjective forecasts currently being issued.

Since knowledge of droplet size distribution was shown to be absolutely critical to determine the icing potential of a storm, second only to having substantial amounts of supercooled liquid water present, attempts should be made to better sample CCN concentrations around the country, perhaps in the same manner as radiosondes are now used to gather information on the basic atmospheric variables of pressure, temperature, winds, and moisture content. It is also very important to understand the vertical profiles of CCN and incorporate this information into the simulations as using a constant CCN profile with height, as is done with this version of RAMS, is a poor assumption outside of the boundary layer. The CCN concentrations should be objectively analyzed like other atmospheric variables when a model is initialized and, the model should be able to keep track of these variable CCN concentrations as they advect through the model domain. It is conceivable to think of a situation where differing airmasses containing substantially different CCN profiles are feeding the same storm (perhaps some 'clean' maritime air as well as polluted continental or urban air) such that the icing potential within this storm is affected by the upstream source of air. This could result in more severe icing in some locations than in others based on this fact.

Along the same lines as the knowledge of CCN would then be to have the model keep track of the varying droplet size distributions which are of course naturally variable within any storm system. Saying that the distribution shape parameter for a particular storm is the same value everywhere (as is dictated by the model code at present) is nearly as poor of an assumption as setting CCN constant everywhere. The new RAMS microphysics includes the activation of CCN, as well as the prediction of number concentrations of droplets, but ν will still be user-specified.

This is indeed quite a wish list that will not all become reality for at least several years to come. In the mean time, analytical studies such as are being done by researchers at NCAR are continuously shedding light on the very complex subject of aircraft icing. The algorithms being continually developed for use with current model output are showing great

promise to improve upon the present capabilities of models and aviation forecasters. Until the machines and models can be developed to the extent outlined above, improving upon the algorithms in use today will be where the most of the improvements can be made.

References

Air Weather Service, 1980: Forecasters' Guide on Aircraft Icing, Air Weather Service Report No. AWS/TR-80/001, 55 pp. [Available from Air Weather Service, Scott AFB, IL, 62225.]

American Meteorological Society, 1959: *Glossary of Meteorology,* R. Huschke, Ed., Amer. Meteor. Soc., Boston, 638 pp.

Arakawa, A., and V. Lamb, 1981: A Potential Enstrophy and Energy Conserving Scheme for the Shallow Water Equations., *Mon. Wea. Rev.*, **109**, 18-36.

Avissar, R., and R.A. Pielke, 1989: A Parameterization of Heterogeneous Land Surfaces for Atmospheric Numerical Models and its Impact on Regional Meteorology. *Mon. Wea. Rev.*, **117**, 2113-2136.

Benjamin, S.G., K.J. Brundage, P.A. Miller, T.L. Smith, G.A. Grell, D. Kim, J.M. Brown, T.W. Schlatter, and L.L. Marone, 1994: The Rapid Update Cycle at NMC. *10th Conf. on Numerical Weather Prediction*, Portland, OR, Amer. Meteor. Soc., 566-568.

Best, A.C., 1952: Occurrence of High Rates of Ice Accretion on Aircraft. Professional Notes of the Meteorological Office, London, **7**, No. 106.

Carlson, T.N., 1980: Airflow Through Midlatitude Cyclones and the Comma Cloud Pattern. *Mon. Wea. Rev.,* **108**, 1498-1509.

Coffey, R.A., 1996: Neural Net Icing Forecasts. *IFR,* **12** (2), 6-9.

Cole, J., and W.R. Sand, 1991: Statistical Study of Aircraft Icing Accidents. *Proc. 29th Aerospace Sci. Mtg.,* Reno, NV, Amer. Inst. Aero. & Astro., Washington D.C., AIAA 91-0558.

Cooper, W.A., 1989: Effects of Variable Droplet Growth Histories on Droplet Size Distributions. *J. Atmos. Sci.*, **46**, 1301-1311.

Cotton, W.R. and R.A. Anthes, 1989: Storm and Cloud Dynamics. *Academic Press, Inc.*, 883 pp.

De Almeida, F.C., 1979: The Effects of Small-Scale Turbulent Motions on the Growth of a Cloud Droplet Spectrum. *J. Atmos. Sci.*, **36**, 1557-1563.

Federal Aviation Administration, 1975: Aviation Weather for Pilots and Flight Operations Personnel. ACOO-6A, DOT, FAA, Flight Standards Service and DOC, NOAA, NWS, Washington, D.C.

Flatau, P.J., G.J. Tripoli, J. Verlinde, and W.R. Cotton, 1989: The CSU-RAMS Cloud Microphysics Module: General Theory and Code Documentation. Technical Report 451. [Available from Dept. of Atmospheric Science, Colorado State University, Fort Collins, CO, 80523.]

Klemp, J.B. and R.B. Wilhelmson, 1978: The Simulation of Three-Dimensional Convective Storm Dynamics. *J. Atmos. Sci.*, **35**, 1097-1110.

Lewis, W., 1947: A Flight Investigation of the Meteorological Conditions Conducive to the Formation of Ice on Airplanes. NACA TN 1393, 50pp.

Lilly, D.K., 1962: On the Numerical Simulation of Buoyant Convection. *Tellus*, **14**, 148-172.

Lomaya, V.A., I.P. Mazin, and A.I. Neizvestnyy, 1990: Effect of Turbulence on the Coagulation Efficiency of Cloud Droplets. *Izv. Atmos. Oceanic Phys.*, **26**, 595-600.

Macklin, W.C., 1962: The Density and Structure of Ice Formed by Accretion. *Quart. J. Roy. Meteor. Soc.*, **88**, 30-50.

Mahrer, Y. and R.A. Pielke, 1977: A Numerical Study of Airflow Over Irregular Terrain. *Beitr. Phys. Atmos.*, **50**, 98-113.

Mason, B.J., 1971: The Physics of Clouds. *Clarendon Press*, 671 pp.

Meyers, M.P., 1995: The Impact of a Two-Moment Cloud Model on the Microphysical Structure of Two Precipitation Events. Ph.D. Dissertation, Colorado State University, 165 pp. [Available from Dept. of Atmospheric Science, Colorado State University, Fort Collins, CO, 80523.]

Newton, D.W., 1978: An Integrated Approach to the Problem of Aircraft Icing. *J. Aircraft,* **15,** 374-380.

NOAA/USDA Joint Agriculture Facility, Washington D.C., 1994: Weekly Weather and Crop Bulletin, **81** (44), 1-3.

Pielke, R.A., W.R. Cotton, R.L. Walko, C.J. Tremback, W.A. Lyons, L.D. Grasso, M.E. Nicholls, M.D. Moran, D.A. Wesley, T.J. Lee, and J.H. Copeland, 1992: A Comprehensive Meteorological Modeling System - RAMS. *Meteor. Atmos. Phys.*, **49**, 69-91.

Pobanz, B.M., J.D. Marwitz, and M.K. Politovich, 1994: Conditions Associated with Large-Drop Regions. *J. Appl. Meteor.,* **33,** 1366-1372.

Politovich, M.K., 1989: Aircraft Icing Caused by Large Supercooled Droplets. *J. Appl. Meteor.,* **28,** 856-868.

Politovich, M.K., and R. Olson, 1991: An Evaluation of Aircraft Icing Forecasts for the Continental United States. Proceedings, *4th Intl. Conf. on Aviation Weather Systems*, Paris, France.

Politovich, M.K., B.C. Bernstein, F.M. Ralph, P.J. Neiman, J.D. Marwitz, and R. Ashenden, 1995: Meteorological Conditions Associated with the ATR-72 Aircraft Accident Near Roselawn, Indiana on 31 October 1994. Preprints, *Intl. Icing Symposium '95*, Montreal, Canada, 235-243.

Reed, R.J., Y.-H. Kuo, and S. Low-Nam, 1994: An Adiabatic Simulation of the ERICA IOP 4 Storm: An Example of Quasi-Ideal Frontal Cyclone Development. *Mon. Wea. Rev.,* **122**, 2688-2708.

Reuter, G.W., C.J. Wright and D. Eyre, 1989: Effects of Turbulence on the Growth of a Could Drop Spectrum. *J. Atmos. Sci.*, **46**, 1407-1410.

Smagorinsky, J., 1963: General Circulation Experiments with the Primitive Equations. Part 1: The Basic Experiment. *Mon. Wea. Rev.*, **91**, 99-164.

Tremback, C.J. and R. Kessler, 1985: A Surface Temperature and Moisture Parameterization for Use in Mesoscale Numerical Models. Preprints, *7th Conf. on Numerical Weather Prediction*, Montreal, Canada, American Meteorological Society.

Tripoli, G.J. and W.R. Cotton, 1982: The Colorado State University Three-Dimensional Cloud/Mesoscale Model - 1982. Part I: General Theoretical Framework and Sensitivity Experiments. *J. Rech. Atmos.*, **16**, 185-220.

Sand, W.R., W.A. Cooper, M.K. Politovich, and D.L. Veal, 1984: Icing Conditions Encountered by a Research Aircraft. *J. Climate Appl. Meteor.,* **23,** 1427-1440.

Schultz, P. and M.K. Politovich, 1992: Toward the Improvement of Aircraft-Icing Forecasts for the Continental United States. *Wea. Forecasting,* **7,** 491-500.

Walko, R.L., C.J. Tremback, and R. Hertenstein, 1993: RAMS - The Regional Atmospheric Modeling System Version 3a User's Guide. [Available from Dept. of Atmospheric Science, Colorado State University, Fort Collins, Colorado, 80523.]

Walko, R.L., W.R. Cotton, M.P. Meyers, and J.Y. Harrington, 1995: New RAMS Cloud Microphysics Parameterization. Part I: The Single Moment Scheme. *Atmos. Res.*, **38**, 29-62.

Appendix A

The following is a discussion into how the following values were computed in an attempt to calculate the potential accumulation of ice on aircraft; the number of droplets in the droplet size distribution larger than 30 μm (N_{30}), the mixing ratio or mass of cloud water contained in these same droplets larger than 30 μm (r_{30}), and the mass mean diameter (D_m). First, for N_{30},

$$N_{30} = \int_{D_x}^{\infty} n(D)dD = \int_{D_x}^{\infty} f_{gam}(D)dD \tag{A.1}$$

where D_x is the lower limit of the integral, in this case $D_x = 30$ μm, $n(D)$ is the number of droplets contained per unit increment of diameter D occuring at size D, dD is the increment of diameter D, and $f_{gam}(D)$ is the generalized gamma distribution described by Flatau *et al* (1989). It is given by

$$f_{gam}(D) = \frac{1}{\Gamma(\nu)} \left(\frac{D}{D_n}\right)^{\nu-1} \frac{1}{D_n} \exp\left(-\frac{D}{D_n}\right) \tag{A.2}$$

where $D_n = (\frac{r_c}{N_t} \frac{6\rho_a}{\pi\rho_l} \frac{1}{(\nu)(\nu+1)(\nu+2)})^{(1/3)}$, or the characteristic size of the droplets, r_c is the cloud water mixing ratio, N_t is the number concentration of droplets per unit volume, ρ_a is the density of air, ρ_l is the density of liquid water, and ν is the shape parameter. Evaluating equation A.1 further then yields the following,

$$N_{30} = \int_{D_x}^{\infty} \frac{N_t}{\Gamma(\nu)} \left(\frac{D}{D_n}\right)^{\nu-1} \frac{1}{D_n} \exp\left(-\frac{D}{D_n}\right) dD \tag{A.3}$$

Substituting in $\chi = \frac{D}{D_n}$, this can be written as

$$N_{30} = \frac{N_t}{\Gamma(\nu)} \int_{\frac{D_x}{D_n}}^{\infty} \chi^{\nu-1} e^{-\chi} d\chi. \tag{A.4}$$

Here, the integral on the right hand side of A.4 is just

$$\int_{\frac{D_x}{D_n}}^{\infty} \chi^{\nu-1} e^{-\chi} d\chi = \Gamma\left(\nu, \frac{D_x}{D_n}\right) \tag{A.5}$$

where $\Gamma\left(\nu, \frac{D_x}{D_n}\right)$ is the incomplete, or truncated gamma function, also described by Flatau *et al* (1989). This just leaves then

$$N_{30} = N_t \frac{\Gamma\left(\nu, \frac{D_x}{D_n}\right)}{\Gamma(\nu)}. \tag{A.6}$$

The calculation of r_{30} begins similarly to above, except that mass needs to be included:

$$r_{30} = \int_{D_x}^{\infty} m(D)n(D)dD \tag{A.7}$$

$$r_{30} = \int_{D_x}^{\infty} \frac{\pi}{6}\rho_l D^3 \frac{N_t}{\Gamma(\nu)} \left(\frac{D}{D_n}\right)^{\nu-1} \frac{1}{D_n} \exp\left(-\frac{D}{D_n}\right) dD \tag{A.8}$$

Here, substitute in $D^3 = D_n^3 \left(\frac{D}{D_n}\right)^3$ to get

$$r_{30} = \frac{\pi}{6}\rho_l D_n^3 \frac{N_t}{\Gamma(\nu)} \Gamma\left(\nu + 3, \frac{D_x}{D_n}\right). \tag{A.9}$$

Finally, to find the mass mean diameter, D_m, the following two integrals must be equated and solve for D_m.

$$\int_{D_m}^{\infty} m(D)n(D)dD = \frac{1}{2}\int_0^{\infty} m(D)n(D)dD \tag{A.10}$$

Substituting as before these become:

$$\frac{\pi}{6}\rho_l D_n^3 \frac{N_t}{\Gamma(\nu)} \Gamma\left(\nu + 3, \frac{D_m}{D_n}\right) = \frac{1}{2}\left[\frac{\pi}{6}\rho_l D_n^3 \frac{N_t}{\Gamma(\nu)}\Gamma(\nu + 3)\right] \tag{A.11}$$

which leaves just

$$\Gamma\left(\nu + 3, \frac{D_m}{D_n}\right) = \frac{1}{2}\Gamma(\nu + 3). \tag{A.12}$$

There is no analytical way to separate D_m out of this last equation, so therefore an iterative method was used in which D_m is adjusted in small increments until both sides are within an acceptable margin of error. As it turns out, the ratio D_m/D_n is nearly linear with ν only, and knowledge of this can be used to simplify the calculation of D_m since finding D_n was fairly straight forward. When the iteration was performed for a large number of r_c and ν, the ratio ended up being to a very close approximation,

$$\frac{D_m}{D_n} \cong 2.67 + \nu \tag{A.13}$$

or rather,

$$D_m \cong (2.67 + \nu)D_n. \tag{A.14}$$

Table A.1: **SLW Accumulation Table for N_t=300/cm^3 and ν=1**

r_c(g/kg)	# drops > 30 μm	D_m (μm)	r_c(g/kg) > 30 μm	% r_c > 30 μm
0.10	0.53	17.39	0.012	12.36
0.20	1.96	21.91	0.052	26.09
0.30	3.71	25.08	0.108	36.05
0.40	5.54	27.61	0.174	43.50
0.50	7.37	29.74	0.246	49.29
0.60	9.17	31.60	0.324	53.94
0.70	10.93	33.27	0.404	57.75
0.80	12.62	34.78	0.488	60.95
0.90	14.26	36.18	0.573	63.68
1.00	15.84	37.47	0.660	66.04
1.10	17.36	38.69	0.749	68.09
1.20	18.84	39.82	0.839	69.91
1.30	20.26	40.90	0.930	71.52
1.40	21.64	41.92	1.021	72.96
1.50	22.97	42.89	1.114	74.26
1.60	24.26	43.83	1.207	75.44
1.70	25.52	44.72	1.301	76.51
1.80	26.73	45.59	1.395	77.50
1.90	27.91	46.41	1.490	78.40
2.00	29.06	47.21	1.585	79.23
2.10	30.17	47.99	1.680	80.00
2.20	31.26	48.74	1.776	80.71
2.30	32.31	49.46	1.872	81.38
2.40	33.34	50.17	1.968	82.00
2.50	34.35	50.86	2.064	82.58

Explanation of table: **Column 1**; The cloud water mixing ratio which can be gathered directly from figures of Cloud Water. **Column 2**; The number of droplets (in units of #/cm^3) in the gamma distribution that are larger than 30 μm (the threshold for 'large' droplets) for the respective value of r_c, N_t, and ν (calculated from Eq. A.6). **Column 3**; The mass mean diameter, at which one half the mass of water is contained either above or below this size (calculated from Eq. A.14). **Column 4**; The cloud water mixing ratio contained in the droplets larger than 30 μm (see column 2, calculated from Eq. A.9). The value here can be converted to units of g/cm^3 by multiplying by the density of air at p=700mb (or other desired pressure level) and doing an additional units conversion. **Column 5**; The percent of cloud water contained in the droplets larger than 30 μm compared to the total liquid water content.

Table A.2: **SLW Accumulation Table for N_t=150/cm^3 and ν=1**

r_c(g/kg)	# drops > 30 μm	D_m (μm)	r_c(g/kg) > 30 μm	% r_c > 30 μm
0.10	0.98	21.91	0.026	26.09
0.20	2.77	27.61	0.087	43.50
0.30	4.59	31.60	0.162	53.94
0.40	6.31	34.78	0.244	60.95
0.50	7.92	37.47	0.330	66.04
0.60	9.42	39.82	0.419	69.91
0.70	10.82	41.92	0.511	72.96
0.80	12.13	43.83	0.604	75.44
0.90	13.37	45.59	0.697	77.50
1.00	14.53	47.21	0.792	79.23
1.10	15.63	48.74	0.888	80.71
1.20	16.67	50.17	0.984	82.00
1.30	17.67	51.53	1.081	83.12
1.40	18.61	52.81	1.178	84.11
1.50	19.52	54.05	1.275	84.99
1.60	20.38	55.22	1.373	85.78
1.70	21.21	56.35	1.470	86.50
1.80	22.01	57.44	1.569	87.14
1.90	22.78	58.48	1.667	87.73
2.00	23.52	59.48	1.765	88.26
2.10	24.23	60.46	1.864	88.76
2.20	24.92	61.40	1.963	89.21
2.30	25.59	62.32	2.061	89.63
2.40	26.23	63.21	2.160	90.02
2.50	26.86	64.08	2.259	90.38

Explanation of table: Same as for Table A.1.

Table A.3: **SLW Accumulation Table for N_t=500/cm^3 and ν=1**

r_c(g/kg)	# drops > 30 μm	D_m (μm)	r_c(g/kg) > 30 μm	% r_c > 30 μm
0.10	0.27	14.67	0.006	5.86
0.20	1.29	18.48	0.031	15.45
0.30	2.73	21.16	0.071	23.69
0.40	4.40	23.28	0.122	30.45
0.50	6.18	25.08	0.180	36.05
0.60	8.00	26.65	0.245	40.76
0.70	9.85	28.06	0.313	44.77
0.80	11.68	29.34	0.386	48.24
0.90	13.50	30.51	0.461	51.27
1.00	15.29	31.60	0.539	53.94
1.10	17.05	32.62	0.619	56.31
1.20	18.78	33.59	0.701	58.44
1.30	20.48	34.50	0.785	60.36
1.40	22.14	35.35	0.869	62.10
1.50	23.76	36.18	0.955	63.68
1.60	25.35	36.97	1.042	65.13
1.70	26.91	37.72	1.130	66.47
1.80	28.44	38.45	1.219	67.70
1.90	29.93	39.15	1.308	68.85
2.00	31.40	39.82	1.398	69.91
2.10	32.83	40.48	1.489	70.90
2.20	34.24	41.10	1.580	71.82
2.30	35.61	41.72	1.672	72.69
2.40	36.96	42.31	1.764	73.50
2.50	38.29	42.89	1.857	74.26

Explanation of table: Same as for Table A.1.

Table A.4: **SLW Accumulation Table for N_t=750/cm^3 and ν=1**

r_c(g/kg)	# drops > 30 μm	D_m (μm)	r_c(g/kg) > 30 μm	% r_c > 30 μm
0.10	0.14	12.81	0.003	2.81
0.20	0.81	16.14	0.018	9.13
0.30	1.93	18.48	0.046	15.45
0.40	3.33	20.34	0.084	21.12
0.50	4.91	21.91	0.130	26.09
0.60	6.60	23.28	0.183	30.45
0.70	8.37	24.51	0.240	34.30
0.80	10.17	25.63	0.302	37.71
0.90	12.01	26.65	0.367	40.76
1.00	13.85	27.61	0.435	43.50
1.10	15.69	28.50	0.506	45.98
1.20	17.52	29.34	0.579	48.24
1.30	19.34	30.13	0.654	50.30
1.40	21.15	30.89	0.731	52.19
1.50	22.94	31.60	0.809	53.94
1.60	24.70	32.29	0.889	55.55
1.70	26.45	32.95	0.970	57.05
1.80	28.17	33.59	1.052	58.44
1.90	29.87	34.19	1.135	59.74
2.00	31.55	34.78	1.219	60.95
2.10	33.21	35.35	1.304	62.10
2.20	34.84	35.91	1.390	63.17
2.30	36.45	36.44	1.476	64.18
2.40	38.03	36.97	1.563	65.13
2.50	39.60	37.47	1.651	66.04

Explanation of table: Same as for Table A.1.

Table A.5: **SLW Accumulation Table for N_t=1000/cm^3 and ν=1**

r_c(g/kg)	# drops > 30 μm	D_m (μm)	r_c(g/kg) > 30 μm	% r_c > 30 μm
0.10	0.08	11.64	0.002	1.52
0.20	0.55	14.67	0.012	5.86
0.30	1.41	16.79	0.032	10.76
0.40	2.57	18.48	0.062	15.45
0.50	3.94	19.91	0.099	19.77
0.60	5.46	21.16	0.142	23.69
0.70	7.09	22.27	0.191	27.23
0.80	8.80	23.28	0.244	30.45
0.90	10.56	24.22	0.300	33.38
1.00	12.35	25.08	0.361	36.05
1.10	14.17	25.89	0.424	38.50
1.20	16.01	26.65	0.489	40.76
1.30	17.85	27.38	0.557	42.84
1.40	19.69	28.06	0.627	44.77
1.50	21.53	28.71	0.699	46.57
1.60	23.36	29.34	0.772	48.24
1.70	25.19	29.94	0.847	49.80
1.80	27.00	30.51	0.923	51.27
1.90	28.80	31.07	1.000	52.64
2.00	30.58	31.60	1.079	53.94
2.10	32.35	32.12	1.158	55.16
2.20	34.11	32.62	1.239	56.31
2.30	35.84	33.11	1.320	57.40
2.40	37.56	33.59	1.403	58.44
2.50	39.27	34.05	1.486	59.42

Explanation of table: Same as for Table A.1.

Table A.6: **SLW Accumulation Table for N_t=300/cm^3 and ν=3**

r_c(g/kg)	# drops > 30 μm	D_m (μm)	r_c(g/kg) > 30 μm	% r_c > 30 μm
0.10	0.04	12.46	0.001	0.70
0.20	0.42	15.70	0.008	4.14
0.30	1.28	17.98	0.027	9.02
0.40	2.57	19.78	0.057	14.22
0.50	4.18	21.31	0.096	19.27
0.60	6.02	22.65	0.144	24.00
0.70	8.02	23.84	0.198	28.36
0.80	10.13	24.93	0.259	32.34
0.90	12.32	25.92	0.324	35.99
1.00	14.56	26.85	0.393	39.32
1.10	16.82	27.72	0.466	42.37
1.20	19.09	28.53	0.542	45.16
1.30	21.36	29.31	0.620	47.73
1.40	23.62	30.04	0.701	50.09
1.50	25.86	30.74	0.784	52.28
1.60	28.07	31.40	0.869	54.30
1.70	30.26	32.05	0.955	56.18
1.80	32.43	32.66	1.043	57.93
1.90	34.56	33.26	1.132	59.56
2.00	36.65	33.84	1.222	61.08
2.10	38.72	34.39	1.312	62.50
2.20	40.75	34.92	1.404	63.83
2.30	42.74	35.45	1.497	65.09
2.40	44.70	35.95	1.590	66.27
2.50	46.63	36.44	1.685	67.38

Explanation of table: Same as for Table A.1.